

## ABSTRACT

Multi Objective Optimization for Seismology (MOOS), with Applications to the Middle East, the Texas Gulf Coast, and the Rio Grande Rift

Mohit Agrawal, Ph.D.

Chairperson: Robert J. Pulliam, Ph.D.

We develop and apply new modeling methods that make use of disparate but complementary seismic “functionals,” such as receiver functions and dispersion curves, and model them using a global optimization method called “Very Fast Simulated Annealing” (VFSA). We apply aspects of the strategy, which we call “Multi Objective Optimization for Seismology” (MOOS), to three broadband seismic datasets: a sparse network in the Middle East, a closely-spaced linear transect across Texas Gulf Coastal Plain, and a 2D array in SE New Mexico and West Texas (the eastern flank of the Rio Grande Rift).

First, seismic velocity models are found, along with quantitative uncertainty estimates, for eleven sites in the Middle East by jointly modeling Ps and Sp receiver functions and surface (Rayleigh) wave group velocity dispersion curves. These tools demonstrate cases in which joint modeling of disparate and complementary functionals provide better constraints on model parameters than a single functional alone.

Next, we generate a 2D stacked receiver function image with a common conversion point stacking technique using seismic data from a linear array of 22 broadband stations deployed across Texas's Gulf Coastal Plain. The image is migrated using velocity models found by modeling dispersion curves computed via ambient noise cross-correlation. Our results show that the Moho disappears outboard of the Balcones Fault Zone and that a significant, negative-polarity discontinuity exists beneath the Coastal Plain.

Lastly, we stack and depth-migrate Ps and Sp receiver functions computed from data recorded by broadband stations deployed by the SIEDCAR (Seismic Investigation of Edge Driven Convection Association with Rio Grande Rift) project. To find P- and S-wave velocity models for receiver function migration, we develop and apply a technique that is analogous to "velocity analysis" in seismic reflection processing. The resulting 3D image reveals gaps in the seismically-determined lithosphere-asthenosphere boundary (LAB) and Moho beneath dramatically uplifted topography and above a distinct fast anomaly (found independently via seismic travel time tomography). We speculate that this gap is the result of large-scale lithospheric removal associated with east-west extension and the northward propagation of the Rio Grande Rift.

Multi Objective Optimization for Seismology (MOOS), with Applications to the Middle East,  
the Texas Gulf Coast, and the Rio Grande Rift

by

Mohit Agrawal, M.S.

A Dissertation

Approved by the Department of Geosciences

---

Stacy C. Atchley, Ph.D., Chairperson

Submitted to the Graduate Faculty of  
Baylor University in Partial Fulfillment of the  
Requirements for the Degree  
of  
Doctor of Philosophy

Approved by the Dissertation Committee

---

Robert J. Pulliam, Ph.D., Chairperson

---

John A. Dunbar, Ph.D.

---

Vincent S. Cronin, Ph.D.

---

Stephen I. Dworkin, Ph.D.

---

Gregory A. Benesh, Ph.D.

Accepted by the Graduate School

May 2016

---

J. Larry Lyon, Ph.D., Dean

Copyright © 2016 by Mohit Agrawal

All rights reserved

## TABLE OF CONTENTS

List of Figures	vii
List of Tables	x
Acknowledgments	xi
Dedication	xiii
Chapter One. Introduction	1
Chapter Two. Crustal and Uppermost Mantle Structure in the Middle East: Assessing Constraints Provided by Jointly Modelling Ps and Sp Receiver Functions and Rayleigh Wave Group Velocity Dispersion Curves	3
Summary	3
Introduction	5
Review of Middle East Tectonics	7
Data Functionals	10
Multi-Objective Optimization in Seismology (MOOS)	13
Objective Function	14
Global Optimization Method: Very Fast Simulated Annealing (VFSA)	15
Uncertainty Estimation	17
Data and Methodology	19
Joint Modeling of Multiple Datasets	22
Joint modeling of the Crust and Uppermost Mantle beneath the Middle East	35
Discussion and Conclusion	55
Acknowledgments	56
References	58
Supporting Information	67
Chapter Three. Lithospheric Structure of the Texas-Gulf of Mexico Passive Margin from Surface Wave Dispersion and Migrated Ps Receiver Functions	73
Abstract	73
Introduction	75
Geological Background	79
Sequential Modeling of Rayleigh Wave Group Velocity Dispersion and Ps Receiver Functions	81
Method	82
Data	94
Results and Discussion	95

Acknowledgements	108
References	110
Chapter Four. Lithospheric Removal beneath the Eastern Flank of the Rio Grande Rift from Receiver Function Velocity Analysis	119
Abstract	119
Introduction	121
Data	128
Methodology	128
Results	140
Discussion	145
Conclusion	149
Acknowledgments	150
References	151
Chapter Five. Conclusions	156
References	156

## LIST OF FIGURES

Figure		Page
Figure 2.1	Distributions of seismic stations in Middle East map	9
Figure 2.2	Example of surface wave dispersion and model predictions	12
Figure 2.3	Plot of convergence of joint error for station S02	22
Figure 2.4	Synthetics via MOOS using Ps receiver function only	25
Figure 2.5	Synthetics using Ps receiver function and dispersion curves	26
Figure 2.6	Synthetics using Ps and Sp receiver function and dispersion curves	28
Figure 2.7	PPDs and correlation matrices for station S02 in Oman	30
Figure 2.8	Joint modeling results for station KIV in Russia	34
Figure 2.9	Joint modeling results for station ATD in Djibouti	38
Figure 2.10	Joint modeling results for station KYPR in Turkey	40
Figure 2.11	Joint modeling results for station DYBR in Turkey	42
Figure 2.12	Joint modeling results for station AGIN in Turkey	44
Figure 2.13	Joint modeling results for station BTLS in Turkey	45
Figure 2.14	Joint modeling results for station CSS in Cyprus	48
Figure 2.15	Joint modeling results for station S04 in Oman	50
Figure 2.16	Joint modeling results for station D2 in Iran	52
Figure 2.17	Joint modeling results for station RAYN in Saudi Arabia	54
Figure S2.1	Figure of thickness PPD for station S02 in Oman	67
Figure S2.2	Figure of thickness PPD for station KIV in Russia	67
Figure S2.3	Figure of thickness PPD for station ATD in Djibouti	68

Figure S2.4	Figure of thickness PPD for station KYPR in Turkey	68
Figure S2.5	Figure of thickness PPD for station DYBR in Turkey	69
Figure S2.6	Figure of thickness PPD for station AGIN in Turkey	69
Figure S2.7	Figure of thickness PPD for station BTLS in Turkey	70
Figure S2.8	Figure of thickness PPD for station CSS in Cyprus	70
Figure S2.9	Figure of thickness PPD for station S04 in Oman	71
Figure S2.10	Figure of thickness PPD for station D2 in Iran	71
Figure S2.11	Figure of thickness PPD for station RAYN in Saudi Arabia	72
Figure 3.1	Map of tectonic features in Texas Gulf Coastal Plain	77
Figure 3.2	Block diagram of methodology to construct seismic image	83
Figure 3.3	Schematic diagram for processing ambient noise	84
Figure 3.4	Example of ambient noise cross-correlation technique	86
Figure 3.5	Fitting of dispersions curves and models using VFSA	88
Figure 3.6	2-D Vs models interpolated from 1-D Vs models	89
Figure 3.7	Plots of events bins and slowness bins for station GC01	91
Figure 3.8	Ps receiver functions via multichannel deconvolution method	93
Figure 3.9	Earthquake locations used in Ps receiver functions	96
Figure 3.10	Ps CCP stacked image, interpretation and cartoon section	102
Figure 3.11	Hit counts and stack error in Ps CCP stacking	107
Figure 4.1	Topographic map of western United States	123
Figure 4.2	Geologic map of southwestern New Mexico and west Texas	126
Figure 4.3	Block diagram of methodology to construct 3D seismic image	129
Figure 4.4	Ps and Sp receiver functions for station 123A	130

Figure 4.5	Starting models used for optimization via VFSA	136
Figure 4.6	Joint optimization results for station 328A and 123A	137
Figure 4.7	3D Vp and Vs models interpolated from 1D Vp and Vs models	138
Figure 4.8	Ps and Sp CCP images along south-north profiles	141
Figure 4.9	Ps and Sp CCP images along west-east profiles	142
Figure 4.10	Hit counts associated with Ps and Sp receiver functions for D-D'	144
Figure 4.11	Moho and LAB topography beneath SIEDCAR region	146

## LIST OF TABLES

Table		Page
Table 2.1	List of seismic station names and locations for Moho depths.	20

## ACKNOWLEDGMENTS

First and foremost, I would like to dedicate this thesis to my parents, Sri Brijmohan Agrawal and Srimati Kamla Devi, for their endless support and love throughout my life. Thank you both for providing me strength to make it possible. My sincere thanks to my brother, Devesh Kumar Agrawal, who always stood by me all the way since the beginning of my studies. His invaluable advices and numerous supportive speeches were always there to help me whenever I was wandering in the dark. To all my family members, Kaushal bhaiyya, Shobhit, Prachi Bhabhi and Khushboo Bhabhi: Thank you all for your moral support over the course of my entire academic career and having faith in me.

Personally, I would like to express my deepest gratitude to my PhD advisor Dr. Jay Pulliam for helping me through my graduate school experiences. I truly appreciated all the endless hours that you spend to train me in learning various aspects of seismology. I really admire you not only as a wonderful advisor but also as an awesome human being. There were many occasions when I behaved whimsically and you just tolerated and forgiven me like a mature friend. You always treated me with respect and have provided me complete freedom to choose my own research directions. Although you were always there to help me whenever I needed it. I found a very trustworthy friend in you whom I can play table tennis with and share my personal feelings. I also want to thank you for accommodating me being vegetarian in various dinners that you organized at your apartment. You were always a great source of inspiration for me and while seeing you

working hard for your students, I always felt energized and tried to put my best effort in my research projects. I really don't feel I could have get better supervisor than you and I will always miss you.

I would like to thank all my committee members Dr. Vincent Cronin, Dr. John Dunbar, Dr. Steven Dworkin and Dr. Gregory Benesh for various discussions and suggestions. Thank is also due to other faculty members who taught me in various courses.

I would also like to thank Dr. Mrinal K. Sen from Jackson School of Geosciences at UT Austin for his care and timely help to improve my geotechnical skills. Along with that I want to especially thank his graduate students Reetam Biswas and Debanjan Dutta with whom I could spend many great moments together.

I would also like to thank my current and past colleagues Tian Xu, Nathan Benton, Jeffery Jex, Adam Collard, Tyler, Hannah Mejia, James Parker, Kenton Shaw, Martin, Dominic, Ryan and Mike for their help in my comfortable stay at Baylor.

Thanks to my friends Gift Ntuli (also colleague), Bulbul Ahmmed, Jagannath Bhuyan, Tushar Kanti Mahato, Rishabh Dutta, Priya Gianchandani and Chinenye IHEME who were always there to support over the course of my entire academic career and for always reminding me that my dreams can come true, no matter how impossible they may seem.

Thanks a lot to Baylor and Department of Geology for providing me necessary and excellent facilities which helped me a lot in successful completion of my PhD.

DEDICATION

To  
My Parents

## CHAPTER ONE

### Introduction

This dissertation is the result of four years and two months of research that began with a new modeling technique that uses disparate but complementary functionals, such as receiver functions and dispersion curves, to produce 1D models beneath broadband seismic stations in the Middle East, along with quantitative estimates of the uncertainties and independence of model parameters. Next, we use various aspects of this new technique to find velocity models for use in the migration of receiver functions computed for the Texas Gulf Coastal Plain and the eastern flank of the Rio Grande Rift (RGR). As a result of this research, we submitted three papers to peer-reviewed journals. The first appeared in 2015 in “Geophysical Journal International”; the second appeared (also in 2015) in “G-cubed (Geochemistry, Geophysics and Geosystems)”; the third was submitted to the “Journal of Geophysical Research” in March 2016, where it is currently under review.

Those involved with these three papers were my advisor, Dr. Robert J. Pulliam of Baylor University, with six other co-authors, Dr. Mrinal K. Sen of University of Texas at Austin, Dr. Utpal Dutta of University of Alaska Anchorage, Dr. Michael E. Pasyanos and Robert Mellors of Lawrence Livermore National Laboratory, Dr. Harold Gurrola of Texas Tech and Dr. Stephen P. Grand of University of Texas at Austin. Dr. Pulliam served as PI of the NSF-funded SIEDCAR project, which acquired the data on the eastern flank of RGR, and the THECB-funded GCP project, which acquired data across Texas’s

Gulf Coastal Plain, as well as the NNSA-funded Middle East seismic project. He also wrote the codes used to display the PPDs and parameter correlation matrices, and supervised the interpretation of results. Dr. Mrinal Sen, Co-PI of the Middle East project, wrote the FORTRAN codes we used to perform Very Fast Simulated Annealing and quantitative uncertainty estimates using Posterior Probability Density (PPDs) functions and parameter covariance matrix. Dr. Michael Pasyanos provided the Rayleigh wave group velocity dispersion curves for 11 seismic stations in the Middle East. Dr. Utpal Dutta helped me understand the joint modeling technique. Dr. Robert Mellors briefed us in understanding the geologic setting of the Middle East. Dr. Harold Gurrola, Co-PI of the GCP project, led the field party to acquire data across Texas's Gulf Coastal Plain and helped interpret the stacked Ps receiver function image. Dr. Stephen P. Grand was Co-PI of the SIEDCAR project and provided valuable comments concerning the interpretation of receiver functions in the third paper.

In addition to developing a new modeling methodology and applying it to three unique datasets, we also developed two ways to find velocity models for receiver function migrations, in chapters 3 and 4. Aside from the introductory and concluding chapters (one and five, respectively), each chapter follows the style required by the journal to which it was submitted.

## CHAPTER TWO

Crustal and Uppermost Mantle Structure in the Middle East: Assessing Constraints Provided by Jointly Modelling Ps and Sp Receiver Functions and Rayleigh Wave Group Velocity Dispersion Curves

This chapter published as: Mohit Agrawal, Jay Pulliam, Mrinal K. Sen, Utpal Dutta, Michael E. Pasyanos, and Robert Mellors

Crustal and Uppermost Mantle Structure in the Middle East: Assessing Constraints Provided by Jointly Modelling Ps and Sp Receiver Functions and Rayleigh Wave Group Velocity Dispersion Curves,

Geophys. J. Int. (May, 2015) 201 (2): 783-810 doi:10.1093/gji/ggv050

### *Summary*

Seismic velocity models are found, along with uncertainty estimates, for 11 sites in the Middle East by jointly modelling Ps and Sp receiver functions and surface (Rayleigh) wave group velocity dispersion. The approach performs a search for models that satisfy goodness-of-fit criteria guided by a variant of simulated annealing and uses statistical tools to assess these products of searches. These tools, a parameter correlation matrix and marginal posterior probability density (PPD) function, allow us to evaluate quantitatively the constraints that each data type imposes on model parameters and to identify portions of each model that are well-constrained relative to other portions. This joint modelling technique, which we call ‘multi-objective optimization for seismology’, does not require a good starting solution, although such a model can be incorporated easily, if available, and can reduce the computation time significantly. Applying the process described above to broadband seismic data reveals that crustal thickness varies from 15 km beneath Djibouti (station ATD) to 45 km beneath Saudi Arabia (station RAYN). A pronounced

low velocity zone for both  $V_p$  and  $V_s$  is present at a depth of  $\sim 12$  km beneath station KIV located in northern part of greater Caucasus, which may be due to the presence of a relatively young volcano. Similarly, we also noticed a 6-km-thick low velocity zone for  $V_p$  beginning at 20 km depth beneath seismic station AGIN, on the Anatolian plateau, while positive velocity gradients prevail elsewhere in eastern Turkey. Beneath station CSS, located in Cyprus, an anomalously slow layer is found in the uppermost mantle, which may indicate the presence of altered lithospheric material. Crustal  $P$ - and  $S$ -wave velocities beneath station D2, located in the northeastern portion of central Zagros, range between 5.2–6.2 and 3.2–3.8 km s<sup>-1</sup>, respectively. In Oman, we find a Moho depth of  $34.0 \pm 1.0$  km and  $25.0 \pm 1.0$  to  $30.0 \pm 1.0$  km beneath stations S02 and S04, respectively.

**Keywords:** Time-series analysis; Inverse theory; Probability distributions; Seismicity and tectonics; Computational seismology; Statistical seismology.

## *Introduction*

Accurate seismic velocity models of the crust and upper mantle are essential to finding accurate locations of seismic events and, specifically, for constraining event focal depths. Assessing and quantitatively describing model errors is a critical component of estimating velocity and attenuation structure but such assessment is difficult in non-linear inversions. The non-uniqueness of seismic modelling that relies on fitting a single ‘functional’, such as a receiver function or a surface wave dispersion curve, is unlikely to produce accurate and sufficiently detailed models of the Earth’s crust and upper mantle. Previous workers have documented the non-uniqueness and lack of stability of inversions that use receiver functions alone (e.g. Ammon *et al.* 1990; Sheehan *et al.* 1995; Gurrola *et al.* 1996; Gangopadhyay *et al.* 2007). However, optimal strategies for modelling disparate but potentially complementary data sets to produce reliable velocity profiles are not obvious. One of the objectives of this study is to develop and present an optimal strategy for seismic modelling of Earth structure by fitting more than one functional.

Linear, as well as non-linear, optimization techniques can be used to find minima of the misfit between observed and synthetic data functionals. Linear or local optimization methods, such as least squares methods, typically assume that the error (or misfit) surface is smooth, with only one local minimum. In contrast, nonlinear global optimization techniques can find the global error minimum and thus identify the single model that best explains observed data, even when the error surface is irregular, i.e., there are several local minima along with the single global minimum (which is common in geophysical problems). Nonlinear methods for optimization also work well in cases for which prior information about the geology of an area is limited, because they search the

space of possible models broadly. A number of nonlinear global optimization methods can be used for modeling purposes, such as genetic algorithms (e.g., Holland 1975; Davis & Principe 1991; Forrest 1993; Sen & Stoffa 1995), the neighbourhood algorithm (Sambridge 1998; 1999), Monte-Carlo methods (e.g., Metropolis & Ulam 1949; Hammersley & Handscomb 1964; Press 1968; Wiggins 1969), Markov Chain Monte Carlo (MCMC) methods (e.g., Agostinetti & Malinverno 2010; Bodin *et al.* 2011; Hauser *et al.* 2011; Pasyanos *et al.* 2006; Green 1995; Metropolis *et al.* 1953; Mosegaard & Tarantola 1995), and simulated annealing (e.g., Kirkpatrick *et al.* 1983; Press *et al.* 2007). In this study we use Very Fast Simulated Annealing (VFSA) to find the best-fit model and associated uncertainties (Ingber 1989; Sen & Stoffa 1995; Zhao *et al.* 1996; Gangopadhyay *et al.* 2007). VFSA has proven to be effective and tractable in previous geophysical applications (Zhao *et al.* 1996; Pulliam *et al.* 2006) and has been shown to converge more quickly than other methods while producing similar results (Ingber 1989; Sen & Stoffa 1995; Gangopadhyay *et al.* 2007).

The datasets we use in the study presented here are Ps receiver functions (PRFs), Sp receiver functions (SRFs) and surface wave dispersion curves for Rayleigh wave group velocities (SW). These multiple datasets have distinct but complementary sensitivities towards Earth structure and modeling them together, rather than individually, has the potential to reduce the number and diversity of models that produce acceptable fits to data (i.e., increase “uniqueness”). (Here we use the term “unique” in a sense that admits variable degrees of exclusivity; this allows us to use various modifiers, such as “fairly” and “highly.”)

We apply the technique described above to data from broadband, three-component seismic stations in the Middle East, including portions of northeast Africa and southwest Asia. This region is tectonically complex, so a method that is limited to finding a set of 1-D models that fit multiple datasets must choose among various non-unique models, as well as reconcile inconsistent data.

Assessments of constraints, uniqueness, and parameter independence are performed using statistical tools: the marginal posterior probability density (PPD) function and the model parameter correlation matrix. These tools allow us to evaluate the relative strength of constraints placed on model parameters by each data functional and to identify portions of each model that are well or poorly constrained. With these tools, we address the following questions: 1) How uniquely does each functional identify a “best” model? 2) How do model uniqueness and parameter independence improve with the inclusion of additional data functionals? In particular, what is the utility of S-wave receiver functions? 3) Is the number of acceptable models reduced by jointly fitting multiple data functionals?

### *Review of Middle East Tectonics*

The Middle East and the adjoining regions is complex tectonically, with multiple plate boundaries of differing types as well as areas of active intraplate deformation (e.g. Dewey & Sengor 1979). Because little is known about lithospheric structure in this area, even 1-D models produced at single stations offer important information. Around the Arabian plate, a continental collision is occurring in the north and east with the Eurasian plate while a new oceanic basin is opening in the Red Sea and Gulf of Aden to the south (Cochran 1983; Le Pichon & Francheteau 1978; Sengor & Kidd 1979) (see Figure 2.1).

Northwest of the Arabian Plate, the Dead Sea fault system is a north-south-striking left-lateral shear zone. At the western edge of the Arabian Plate lies the Arabian Shield, which differs from other shield areas in that it has been less stable tectonically over the long-term and witnessed high levels of volcanic activity during the Cenozoic (Seber *et al.* 1997). The translating and counter-clockwise motion of the Arabian plate is responsible for its separation from the African plate with active spreading at the Afar triple junction and associated rifts (Reilinger & McClusky 2011). In the southeast, the Arabian plate shows compression, as expressed by the Oman Mountains. Al-Lazki *et al.* (2002) and Shelton (1990) report that the crust is slightly thinner in the coastal range than in the southwestern Oman Mountains.

Several other strike-slip zones are found in the region, such as the right-lateral North Anatolian fault in Northern Turkey and left-lateral East Anatolian fault in eastern Turkey, which form the eastern and northern part of the Anatolian block (Seber *et al.* 1997). The Anatolian plateau is an uplifted volcanic plateau for which crustal thickness has been estimated to be around 40-50 km (Barazangi *et al.* 2006; Maggi & Priestley 2005). Receiver functions studies show that the lithospheric mantle is missing in this region (Gök *et al.* 2003; Zor *et al.* 2003; Al-Lazki *et al.* 2004; Angus *et al.* 2006). A complex geometry of delaminated lithospheric fragments was indicated by receiver functions and resistivity measurements beneath the Anatolian plateau (Ozacar *et al.* 2008; Türkoğlu *et al.* 2008).

A considerable amount of deformation, manifested by a fold-and-thrust belt, is taking place beneath the Zagros Mountains, located to the north of the Arabian plate. The Turkish-Iranian plateau is located northwest of Zagros and is characterized by volcanics

and strike-slip faulting (Gök *et al.* 2003; Zor *et al.* 2003; Al-Lazki *et al.* 2004; Angus *et al.* 2006).

The East African rift is a narrow, active continental rift zone that appears to be developing a divergent tectonic plate boundary in East Africa. Sandvol *et al.* (1998) find that crustal thickness varies from a minimum of  $8.0 \pm 1.5$  km in East Africa (Afar) to a maximum of  $64 \pm 4.8$  km in the lesser Caucasus.

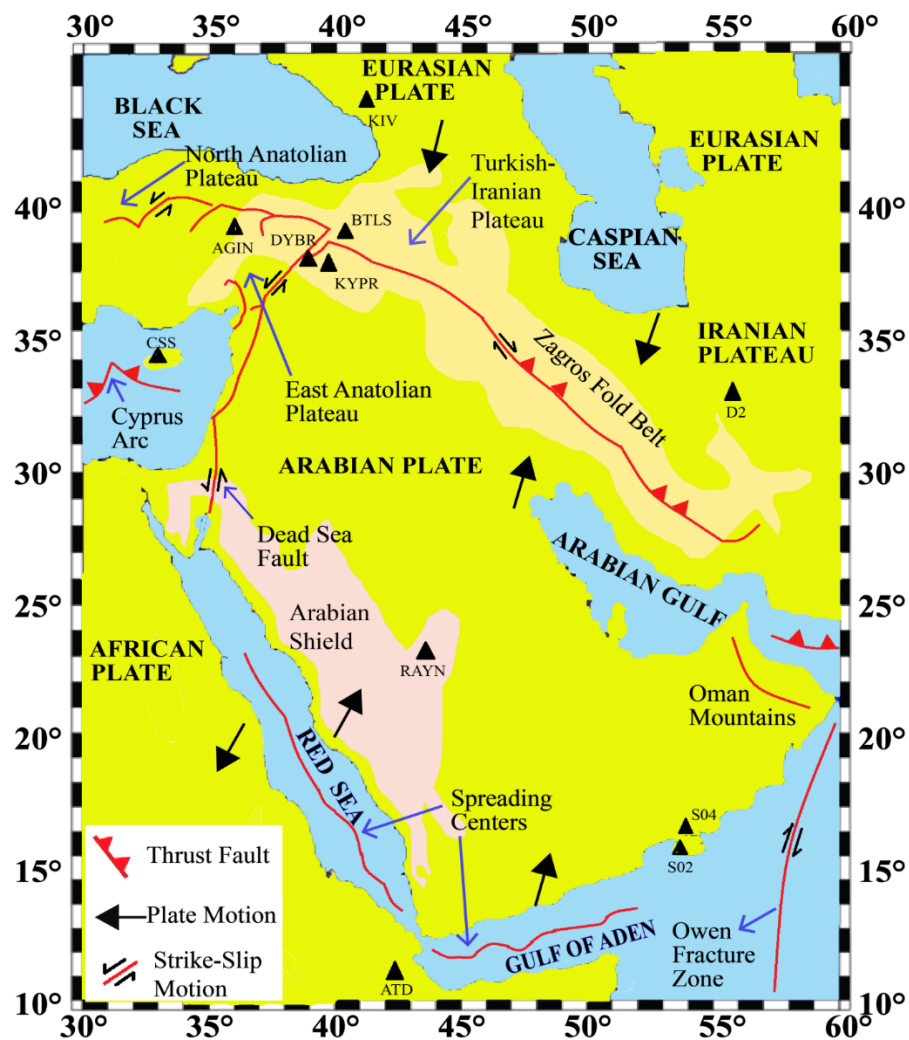


Figure 2.1 Distribution of seismic stations (black triangles) used for joint modelling on a simplified map of the Middle East and adjoining areas.

## *Data Functionals*

*Receiver Function:* Receiver functions are time series, computed from three-component seismograms that show the response of Earth structure beneath a “receiver”, or seismic station (Ammon 1997). Receiver functions are most sensitive to abrupt changes in seismic velocities, such as discontinuities, but only weakly sensitive to absolute velocities (Julia *et al.* 2000). Velocity structure obtained through inversion of receiver functions alone is also highly non-unique (Ammon *et al.* 1990).

Receiver functions have been used to model Earth structure by inversion or by iterative forward methods, such as grid search, genetic algorithms, simulated annealing, and the neighbourhood algorithm. Ps receiver functions (PRFs) have been modelled both individually and jointly with surface wave dispersion (e.g. Ammon *et al.* 2005; Ammon *et al.* 2004; Cakir & Erduran 2004; Chang *et al.* 2004; Dugda & Nyblade 2006; Herrmann *et al.* 2001; Julia *et al.* 2000; Julia *et al.* 2005; Lawrence & Wiens 2004; Ozalaybey *et al.* 1997; Pulliam *et al.* 2002; Pasyanos 2005; Tkalcic *et al.* 2006; etc). Modeling Ps receiver functions alone produces highly non-unique models. Nevertheless, certain characteristics of the model, such as average velocities over portions of the subsurface and impedance contrasts across certain layers, are often constrained by Ps receiver functions (Ammon *et al.* 2004, 2005). Which portions of the model and which layer impedance contrasts are constrained depends on the models themselves, as well as on data quality.

Sp receiver function (SRF) analysis searches for S-to-P conversions at seismic discontinuities. SRFs should, in principle, constrain P velocities in the upper mantle and crust and be more suitable than Ps receiver functions for studying mantle lithosphere (Yuan *et al.* 2006). For a particular station, the converted Sp phase arrives earlier than the

direct S phase (e.g. Faber & Muller 1980; Bock 1991; Farra & Vinnik 2000; Li *et al.* 2004; Kumar *et al.* 2005a, 2005b). In addition to constraints on Vp, Sp receiver functions offer additional benefits compared to Ps receiver functions: They are free from shallow-layer multiples in the time window of arrival of the main converted Sp phases and they sample a much greater distance laterally.

Receiver function computation is a deterministic deconvolution process that can be applied in either time or frequency domains (Clayton & Wiggins 1976). We used an iterative time domain approach that was first developed to estimate high-magnitude source time functions (Kikuchi & Kanamori 1982) and later used to remove source and path effects in receiver function calculation (Ligorria & Ammon 1999). During the process, a low-pass Gaussian filter ( $G(\omega) = \exp(-\omega^2/4a^2)$ , where  $\omega$  is angular frequency and  $a$  is a filter width parameter, is applied in order to remove high frequency noise. The Gaussian filter width parameter,  $a$ , controls the frequency content and, ultimately, the resolution of layer thickness. We used a Gaussian width of 1.5 (or 2 in some cases) for the present study because our main interest is in modeling gross features of the crust and uppermost mantle and also to minimize the effects of scattering on the receiver functions. All events were visually inspected and receiver functions with high signal-to-noise ratios were chosen. We stacked all receiver functions from all backazimuths to highlight key structural features beneath individual stations.

*Surface Wave Dispersion:* The speed of propagation of seismic surface waves is a function of frequency, i.e., seismic surface waves are “dispersive”. Put another way, individual harmonic components of the surface wave seismogram propagate at different speeds. For any given source-receiver pair, one can isolate from the seismogram each

harmonic component and measure its speed between source and receiver. Dispersion can either be characterized by phase velocity (the velocity of an individual peak or trough) or group velocity (which is the velocity of the surface wave energy). Here, we consider only group velocities because they are easier to measure (knowledge of the source phase is not needed) and can be measured for the shorter periods that we need in order to sample the crust.

A dispersion curve is a plot of group or phase velocity versus frequency (Figure 2.2). From a large set of measured dispersion curves, with sources and stations providing as uniform coverage of the Earth as possible, local phase velocity heterogeneities can be mapped as a function of longitude and latitude. At each location, perturbations in phase velocity with respect to a given reference model are weighted averages of seismic heterogeneities in the underlying mantle.

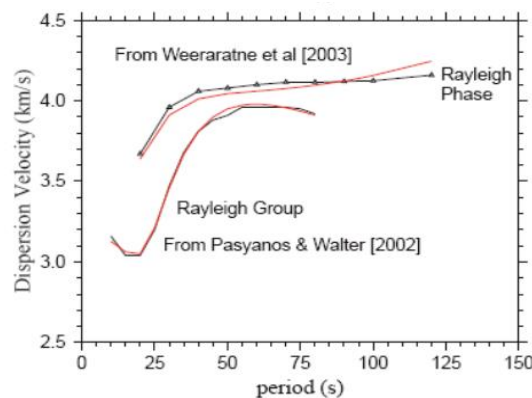


Figure 2.2 Example of surface (Rayleigh) wave dispersion measurements (black lines) and model predictions (red lines) (*modified from Ammon et al.2005*).

In contrast to receiver functions, dispersion curves are sensitive to the absolute values of shear velocities but less sensitive to the depth or sharpness of the discontinuities. In principle, modeling these different datasets jointly, rather than

individually, should improve the constraints imposed on models and result in greater reliability of the models. However, improvements in constraints and model reliability are not guaranteed, so they must be assessed quantitatively in conjunction with “best-fit” modeling.

### *Multi Objective Optimization in Seismology (MOOS)*

Our optimization algorithm is expected to minimize misfit of each of the datasets using three different “objective”, or “cost”, functions. The process of optimizing systematically and simultaneously a collection of objective functions is called Multi Objective Optimization (MOO). The general MOO is posed as follows:

$$\text{Minimize } F(\mathbf{m}) = [F_1(\mathbf{m}), F_2(\mathbf{m}), \dots, F_k(\mathbf{m})]^T, \quad (1)$$

where  $\mathbf{m}$  is the model vector and  $k$  is the number of objective functions. The objective function is minimized subject to some constraints. In our application, we use standard constraints such as bounds and positivity.

Contrary to single-objective optimization, MOO may be considered more of a concept than a definition. Typically, with noisy data there is no single global solution and it is often necessary to determine a set of points that all fit a predetermined definition of “optimum”. This is commonly done using what is known as Pareto optimality (Pareto 1906), which is defined as follows.

*Definition:* A model  $\mathbf{m}^*$  belonging in the model space is said to be Pareto optimal if and only if there does not exist any other model  $\mathbf{m}$  in the model space such that  $F(\mathbf{m}) \leq F(\mathbf{m}^*)$ , and  $F_i(\mathbf{m}) < F_i(\mathbf{m}^*)$  for at least one function. We often use a global criterion in searches for models belonging to a Pareto set, which is a scalar function that

mathematically combines multiple objective functions; it may or may not involve preference of one or the other.

### *Objective Function*

We use the following objective function that outputs a single scalar value.

$$\text{Error} = \mathbf{a}_1 \|\mathbf{d}_{srf}^{obs} - \mathbf{d}_{srf}^{syn}\|_p + \mathbf{a}_2 \|\mathbf{d}_{prf}^{obs} - \mathbf{d}_{prf}^{syn}\|_p + \mathbf{a}_3 \|\mathbf{d}_{sw}^{obs} - \mathbf{d}_{sw}^{syn}\|_p, \quad (2)$$

where, **srf**, **prf** and **sw** represents Sp receiver function, Ps receiver function and surface wave dispersion, respectively, for a given dataset  $\mathbf{d}^{obs}$  and  $\mathbf{d}^{syn}$  denotes observed from real dataset and synthetic from model, respectively, and  $\mathbf{a}_1$ ,  $\mathbf{a}_2$  and  $\mathbf{a}_3$  represent weights to be assigned to each data functional.

For cases involving real, noisy data, weights must be determined by trial and error. One important consideration in defining the global objective function for MOOS is to ascertain that no individual objective function introduces more impact than the others unless a greater impact is desired. We therefore use the following normalized objective function, defined in Sen & Stoffa (1996).

$$\text{Error} = \mathbf{1} - \frac{2\sum |\mathbf{d}_{obs}^i - \mathbf{d}_{syn}^i|^\alpha}{\sum |\mathbf{d}_{obs}^i + \mathbf{d}_{syn}^i|^\alpha + \sum |\mathbf{d}_{obs}^i - \mathbf{d}_{syn}^i|^\alpha} \quad (3)$$

where the sum is taken over all data points and the parameter  $\alpha$  indicates a norm.

Objective functions for receiver functions and dispersion curves look the same, except the value of  $\alpha$  is different. During early trials with real and synthetic data, we initially chose  $\alpha=1$  for all three objective functions. However, the objective function corresponding to the surface wave dispersion is smoothly varying, unlike those for the functionals that depend on the waveforms (e.g., Ps and Sp receiver functions), and we discovered that setting  $\alpha=0.5$  for surface wave dispersion produced better results.

*Global Optimization Method: Very Fast Simulated Annealing (VFSA)*

A common aim in geophysical inversion problems is to find the minimum value of an objective function, or error function,  $E(\mathbf{m})$ , where “ $\mathbf{m}$ ” is the model vector. Linear optimization techniques, such as least square methods, are best suited to finding local minima near the starting model, rather than the global minimum. Finding the global minimum typically requires employing a “global optimization” algorithm; there is a great variety of optimization problems for which Simulated Annealing (SA) has been found useful (e.g., Kirkpatrick *et al.* 1983; Geman & Geman 1984; and Korst & Aarts 1989; among others).

The preliminary concept of simulated annealing (SA) derives from statistical mechanics, in which an analogy is made between model parameter optimization and the particles of an idealized physical system. In the process of crystal annealing, the temperature of a solid in a heat bath is initially allowed to increase, so that all the particles are distributed randomly in a liquid state, and then gradually cooled, so that a “minimum energy” crystal structure is found. Cooling a material rapidly will cause it to convert into glass, finding a local minimum of energy. Cooling a material slowly allows it to find the best-organized, global minimum of energy (ground state), crystal structure. The numerical analogy, “simulated” annealing, requires a slow temperature cooling schedule that will allow the search for minima to be conducted broadly, so we can be sure that the global minimum has been found.

In geophysical inverse problems, SA begins with an initial model ( $\mathbf{m}_0$ ) with associated energy,  $E(\mathbf{m}_0)$ . The energy of the system is quantified by an error function, which is computed from least-square differences between computed and observed data.

The ground state is analogous to the global minimum of the least-squares error. The temperature  $\mathbf{T}$  is analogous to a free parameter that controls the entire search process (Sen & Stoffa 1995). With each iteration, a new model is generated randomly from a uniform distribution within a predefined subspace of the model parameter.

Assume that a model parameter  $m_i$  at iteration  $k$  is represented by  $m_i^k$  such that

$$m_i^{\min} \leq m_i^k \leq m_i^{\max}, \quad (4)$$

where  $m_i^{\min}$  and  $m_i^{\max}$  are the minimum and maximum values of the model parameter  $m_i$  which are set prior to the inversion. The above model parameter value is perturbed at the  $(k+1)^{\text{th}}$  iteration by using the following relation

$$m_i^{k+1} = m_i^k + y_i(m_i^{\max} - m_i^{\min}), \text{ where } -1 \leq y_i \leq 1 \text{ and } m_i^{\min} \leq m_i^{k+1} \leq m_i^{\max} \quad (5)$$

$y_i$  is a random number generated following the Ingber distribution (Ingber 1989). Then error,  $E(\mathbf{m}_{k+1})$ , associated with this new model is computed and compared with error of previously generated model  $\mathbf{m}_k$ . If the error,  $E(\mathbf{m}_{k+1})$ , is less than or equal to  $E(\mathbf{m}_k)$ , new model  $\mathbf{m}_{k+1}$  is accepted unconditionally and replaces the previous model  $\mathbf{m}_k$ . However, even if the acceptance criterion is not satisfied the new model may be selected with a probability of  $[e^{\partial E/\mathbf{T}}]$ , where  $\partial E$  is given by change in energy. This probability-dependent acceptance allows SA to escape a local minimum and continue its broad search of the model space. In order to make conventional SA more efficient, we use a variant of SA called Very Fast Simulated Annealing (VFSA), which chooses new models from a Cauchy-like distribution. Rather than choosing new models randomly, like conventional SA, this distribution function prefers models in proximity to the current model at low temperatures (Geman & Geman 1984; Szu & Hartley 1987; Ingber 1989, 1993). This process is repeated a sufficient number of times with temperature slowly decreasing

according to a predefined cooling schedule until the procedure converges. The temperature schedule is inversely proportional to the iteration number; i.e.

$$T(k) = T_0/k \quad (6)$$

where  $T_0$  and  $k$  are initial temperature and number of iterations. Very Fast Simulated Annealing (VFSA) incorporates temperature dependence into the acceptance criterion for each model parameter, which adds flexibility to its applications and speeds convergence while arriving at substantially the same results (Sen & Stoffa 1995; Gangopadhyay *et al.* 2007). The method is used by Sen and Stoffa (1996) for a number of geophysical applications.

#### *Uncertainty Estimation*

Error functions associated with models often either have broad minima or are multi-valued, indicating that other possible solutions are either slightly different or very different from our single, best-fit model, respectively. We use all the models to construct an approximate marginal posterior probability density (PPD) function using statistical measures of goodness-of-fit (variance) and parameter independence (correlation) (Sen & Stoffa 1996) to represent the solution. While the variance gives the measure of the spread about the mean and thus provides the variability of each individual parameter, the correlation of one parameter with all other parameters reflects the ambiguities of interpretation. Therefore, it becomes necessary to search the model space carefully and to identify models that provide the highest degree of fitness between data functionals. VFSA proves to be efficient in conducting such searches, and the products of multiple searches enable us to estimate uncertainties associated with the best-fit model. The estimation of such uncertainties is particularly necessary in joint modeling problems because they

allow us to determine whether, and to what extent, the number of possible models is reduced with the inclusion of each data functional and to evaluate tradeoffs between model parameters (Pulliam & Sen 2005). Statistical tools such as the marginal posterior probability density (PPD) function and the parameter correlation matrix are most useful for evaluating the reliability of results.

Previous workers have cast inverse problems in a Bayesian framework in order to estimate model parameters in the context of prior information (e.g., Tarantola 1994; Sen & Stoffa 1995) and 'importance sampling', based on Gibbs' sampler, has been employed previously to improve the efficiency of searches (Sen & Stoffa 1995; Pulliam & Sen 2005). The main strategy of 'importance sampling' is to make sampling coarser in the region of the model space where the error function is varying smoothly and to make sampling finer in regions that are characterized by rapid variations and/or in which many acceptable solutions lie. Gibbs' probability distribution was found to play a key role in achieving such concentrated sampling (Sen & Stoffa 1995).

The PPD function [ $\sigma(\mathbf{m} \mid \mathbf{d}_{\text{obs}})$ ], for a model  $\mathbf{m}$  and observed data  $\mathbf{d}_{\text{obs}}$ , is defined as the product of a likelihood function [ $e^{-E(\mathbf{m})}$ ], where  $E(\mathbf{m})$  is an error function, and the prior probability density function,  $\mathbf{p}(\mathbf{m})$ . The prior probability density function describes information one has about the model without knowledge of the data and defines the probability of the model  $\mathbf{m}$  independent of the data. The likelihood function depends on the distribution of errors in the data, and therefore requires prior knowledge of the error distribution. A "multiple VFSA" approach was found to be the most efficient among several approaches examined to form the PPD (Sen & Stoffa 1995 and references therein). Multiple VFSA uses several different random starting models (20 in this study)

along with the set of models sampled to estimate uncertainties. All sampled models are used to estimate marginal probability density functions and the parameter correlation matrix to characterize uncertainties associated with the model.

If the PPD is known, then covariance can be obtained through a multidimensional integral of the form

$$\mathbf{I} = \int \mathbf{f}(\mathbf{m}) \sigma(\mathbf{m} | \mathbf{d}_{obs}) d\mathbf{m}, \quad (8)$$

Where  $\mathbf{f}(\mathbf{m}) = (\mathbf{m} - \langle \mathbf{m} \rangle) (\mathbf{m} - \langle \mathbf{m} \rangle)^T$  for the parameter covariance matrix. Tradeoffs between model parameters are described quantitatively by the parameter correlation matrix, which is computed by normalizing the covariance between model parameters (Sen & Stoffa 1996). In later sections we will describe our results for the Middle East along with PPDs and parameter correlation matrices, so that all results can be evaluated in the context of their associated uncertainties, uniqueness, and the quality of constraints.

### *Data and Methodology*

Figure 2.1 shows permanent broadband seismic stations located in the Middle East that are used in this study. Three-component seismograms were downloaded from the IRIS Data Management Center for the years 1999-2006 for 11 seismic stations. The receiver functions and Rayleigh wave group velocity dispersion curves were computed from these data. Table 1 lists the station codes, names and locations with their estimated Moho depths. Events were selected to have magnitudes of 5.0-7.5 and epicentral distances of 60°-85° for Sp receiver functions and 30°-95° for Ps receiver functions. Complexities in source time functions were largely avoided by excluding very large earthquakes. Because of the specific ray geometry of S-to-P converted phases, the use of Sp receiver functions is limited to a fairly narrow range of epicentral distances. The

number of earthquakes that satisfy the selection criteria described above is fairly small (~79) for SRFs and ~130 for PRFs in the greater Middle East region. A 4-pole low-pass filter with corner frequency of 0.25 Hz was applied and data were then decimated to a sample interval of 0.5 s.

Receiver function calculation involves two main steps: rotation and deconvolution (Li *et al.* 2004). Waveforms were rotated from Z-N-E (vertical, north-south, east-west) components to Z-R-T (vertical, radial, transverse) components using station-event backazimuths and were manually inspected to pick the P-wave arrival and S-wave arrival for PRFs and SRFs, respectively, using Seismic Analysis Code (SAC). We then windowed the seismograms to 10 s before and 20 s after the P-wave arrival for PRFs, and 20 s before and 10 s after the S-wave arrival for SRFs. The coefficient of S-to-P conversion has opposite polarity of P-to-S conversion coefficients so, for ease of comparison, the polarity and time axis were reversed for SRFs, as is common. We use an iterative time domain deconvolution approach for the computation of receiver functions, as described in section 3.1.1.

Table 2.1 List of seismic station codes, names and locations with their estimated Moho depths.

Station code	Station name	Latitude	Longitude	Estimated Moho depth (km)
CSS	Mathiatis, Cyprus	34.96	33.33	35.0±1.0
AGIN	Agin, Turkey	38.93	38.71	37.0±1.0
DYBR	Diyarbakir, Turkey	37.82	40.31	36.0±2.0
BTLS	Bitlis, Turkey	38.43	42.12	36.0±2.0
KYPR	Kiyapinar, Turkey	37.55	41.16	37.0±2.0
S02	Ghado, Oman	17.12	53.99	34.0±1.0
S04	Rawya, Oman	17.44	54.04	(25.0±1.0)-(30.0±1.0)
D2	D2, Iran	32.43	54.70	39.0±2.0
RAYN	Ar Rayn, Saudi Arabia	23.52	45.50	45.0±2.0
ATD	Arta Tunnel, Djibouti	11.53	42.84	15.0±1.0
KIV	Kislovodsk, Russia	43.95	42.68	43.0±2.0

Rayleigh wave group velocity dispersion curves were obtained from a surface wave dispersion study of the region (Pasyanos 2005). The multiple filter method of Dziewonski *et al.* (1969) was used to measure group velocities. This method utilizes a single station and applies a narrow bandpass Gaussian filter to the broadband, vertical-component, displacement seismogram over many different periods (e.g., Herrmann 1973). At each period the maximum amplitude and corresponding arrival time were picked on the envelope and group velocities were computed using the source-receiver great-circle arc distance. In this study we assigned equal weights to each data functional during their joint analysis.

We consulted previously published 1-D velocity models for each station, where available, in order to construct search limits for modeling. Where no previous model could be found, we used ak135 (Kennett *et al.* 1995). For each VFSA run, we set the initial temperature at  $10^{-4}$  units and allowed it to cool down to  $10^{-21}$  units during the process. We discovered, after a set of trials, that the misfit error changed very little after  $\sim 700$  iterations (Figure 2.3), so we set the maximum number of iterations to 1000 to provide a reasonable margin for error. We allowed four model parameters (Poisson's ratio, shear velocity, layer thickness and density) for each of 10 layers to vary within  $\pm 10\%$  of initial values. We also conducted some searches with bounds of  $\pm 20\%$  and  $\pm 30\%$  of the initial values but our inversion process produced results within one standard error for all cases. Significant departures from previously published models are not realistic, considering geologic and tectonic settings of the structure beneath stations under investigation, and searches over such broad ranges are computationally intensive and time-consuming. Therefore, in order to maintain reasonable computation requirements

and to obtain feasible and realistic models, we allowed model parameters to vary within  $\pm 10\%$  in most cases.

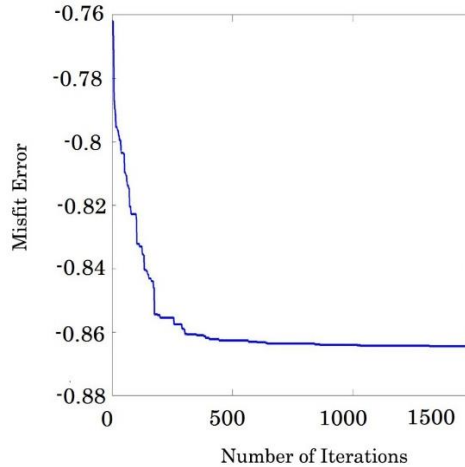


Figure 2.3 Plot of convergence of joint error versus number of iterations (1000) for station S02.

We divided our optimization process into two parts. First, we found the best-fit model using 1000 iterations. Second, we computed uncertainties associated with the best-fit model identified in Step 1 by running our inversion code for 20 VFSA runs (i.e.  $1000 \times 20 = 20,000$  iterations). In the next section we will demonstrate the effects of fitting one, two, or three functionals, using both synthetic and real data, and how estimates of the marginal posterior probability distribution and parameter correlation matrix can be used to assess the constraints placed by the data functionals on model parameters. In later sections we will show results using all three data functionals for each of a set of broadband seismic stations located in the Middle East.

### *Joint Modeling of Multiple Datasets*

There are several advantages to jointly fitting multiple datasets. First, each dataset has unique sensitivities to Earth structure. For example, receiver functions are primarily

sensitive to vertical shear wave travel times between discontinuities (Julia *et al.* 2000). Mutually satisfying constraints imposed by the three datasets may constrain a larger subset of model parameters than a single set alone. In this study, we used Rayleigh wave group velocity dispersion curves, PRFs, and SRFs for two main reasons. First, a recent study by Gök *et al.* (2007) shows that uncertainties associated with fitting Rayleigh wave group velocity dispersion curves and receiver functions are always less than uncertainties that result from fitting Love waves and receiver functions. Second, in the presence of radial anisotropy, Love, Rayleigh, and receiver functions cannot be fit well when used jointly to model subsurface structure (Gök *et al.* 2006). In this section, we show results of a quantitative evaluation of the constraints imposed by each of three data functionals on the model fit, including assessments via estimation of marginal PPDs and the parameter correlation matrix for fits to individual functionals and combinations of functionals.

The MOOS code can, in principle, solve for four independent model parameters: Poisson's ratio,  $V_s$ , layer thickness and density. We calculate  $V_p$  values using Poisson's ratio and  $V_s$ . In practice, density tends to be difficult to constrain independently, so in this study we hold density constant.

### *Marginal Posterior Probability Distributions*

Figures 2.4 (c), 2.4 (d) and 2.4(e) show marginal Posterior Probability Density (PPD) functions for  $V_p$ ,  $V_s$  and layer thickness, respectively, for modeling performed by fitting the PRF alone. The colored portions of PPDs represent search ranges; hotter (yellow and red) colors indicate a higher probability that the true velocity will be found at that value. Ideally each layer would have a single-valued, distinct, and highly peaked distribution. Such a case would indicate that the data impose strong constraints on that

model parameter. Note that layer thickness PPDs are not immediately interpretable in terms of depth because the depth to each layer depends on the thicknesses of layers above. In our plots, the y-axis of thickness PPDs therefore indicates layer numbers.

### *Parameter Correlation Matrices*

As shown in Figure 2.4(f), each model layer consists of four independent parameters ( $V_p$ ,  $V_s$ , thickness ( $dz$ ), and  $\rho$ ), four small squares combined together represent a model layer on both axes. Correlation values range from -1 to +1 and are symmetric about the diagonal of the matrix; for the sake of clarity we only show values below the diagonal. Off-diagonal colored squares indicate cross-correlations (tradeoffs) between corresponding model parameters. The numbers above the diagonal of each parameter correlation matrix represents layer number and there corresponding model parameters ( $V_p$ ,  $V_s$ ,  $dz$  and  $\rho$ ). Diagonal elements represent auto-correlations, i.e., they are perfectly correlated with itself. Hence they are identically one for all values. In an ideal case in which all data functionals can be fitted to find a unique, best-fit model, different model parameters would be resolved independently, so off-diagonal elements would be zeros (i.e. all green). In reality, all geophysical problems have tradeoffs (correlations) between parameters, due to imperfect sampling of the subsurface by the data used to constrain models. By “imperfect sampling” we mean that our knowledge of physical processes relating a model to data is often imperfect. Tradeoff between model parameters can be due to non-uniqueness of model parameters, to data noise (either random or systematic), which corrupts the information contained in data, or to approximations (made in the interest of tractability or fast computation) of the physical processes by which forward calculations are produced.

Synthetics using single functional i.e. PRF alone

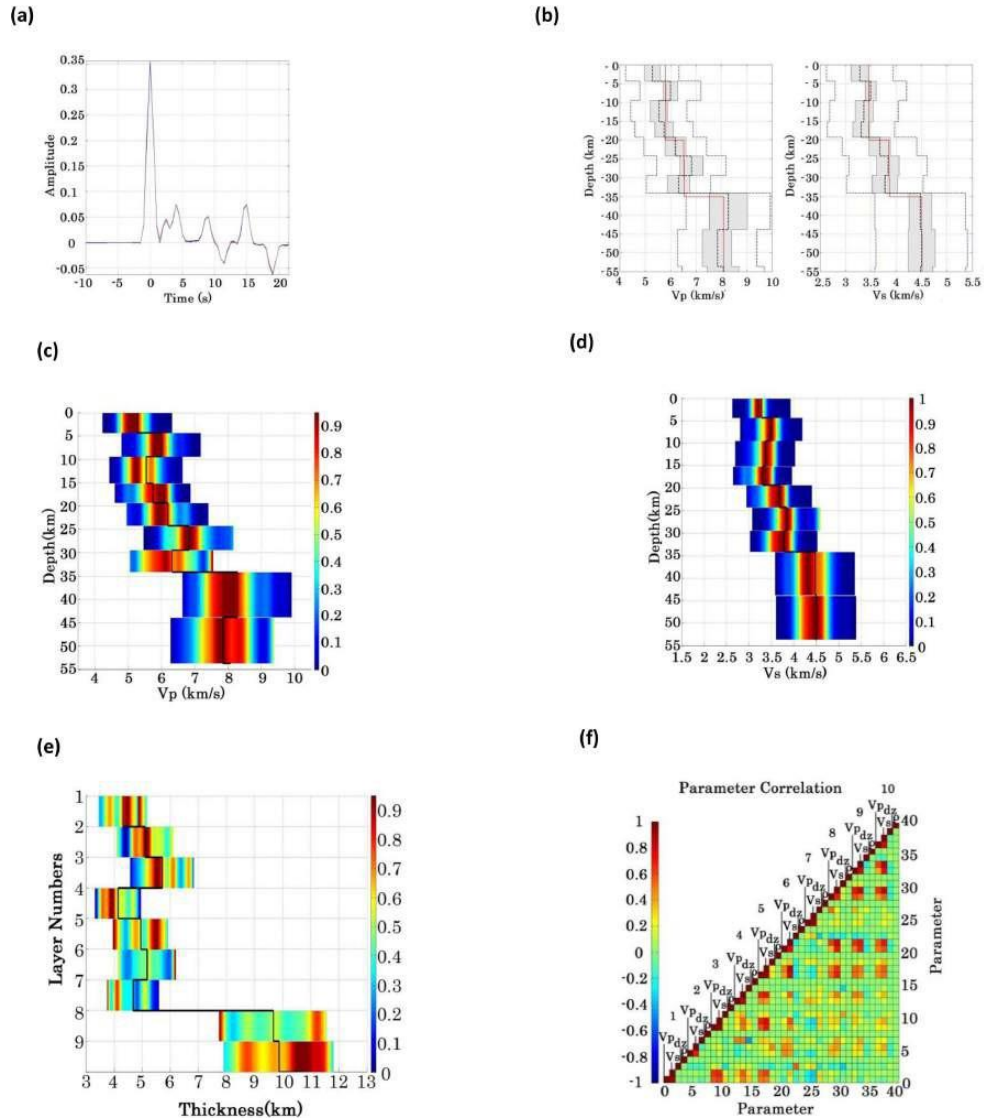


Figure 2.4 Plots show synthetic modelling via MOOS by fitting the Ps receiver function (PRF) only. Panel (a) compares computed (red) and synthetic (blue) PRF functionals. Panel (b) shows the single best-fitting model (dashed black line), the reference Earth model (ak135, red line) and model search space of  $\pm 20$  per cent (dashed blue line) with respect to the best-fitting model. The shaded portion in (b) represents one standard error of the best-fitting model. Plots of marginal PPD functions of  $V_p$ ,  $V_s$  and layer thickness are shown in Panels (c)–(e). The solid black line superimposed on PPDs shows the best-fitting model. In this case, the  $V_p$ ,  $V_s$  and layer thickness PPDs show several broad peaks for most layers.  $V_s$  is better constrained than  $V_p$ , indicating that PRFs are more sensitive to  $V_s$  than  $V_p$ . Panel (f) shows high positive trade-offs in the parameter correlation matrix, which indicates significant interdependence of free parameters (i.e. high non-uniqueness). See text for further details.

Synthetics for two functionals i.e. PRF and SW

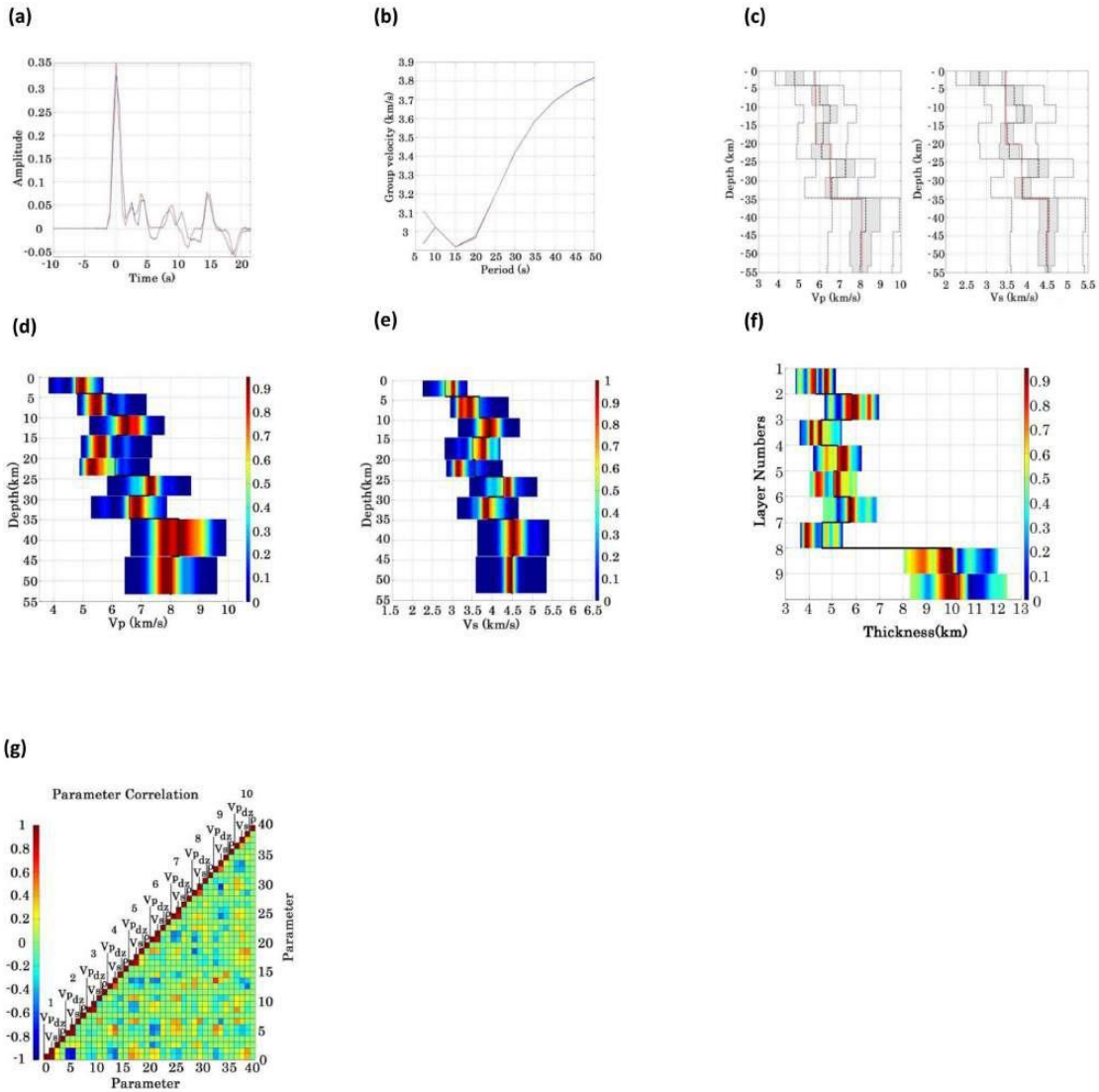


Figure 2.5 Results of synthetic modelling via MOOS in which the Ps receiver function (PRF) and Rayleigh wave group velocity dispersion curve (SW) are fitted jointly. All symbols and colours are the same as in Fig. 2.4. Panels (a) and (b) show fits to PRF and SW functionals, respectively. Panel (c) shows the best-fitting  $V_p$  and  $V_s$  models. PPDs (d–f) show that fitting two functionals limits the range of acceptable models, as indicated by narrower peaks for high-probability values, but the multiple peaks still appear in the layer thickness PPD (f), indicating that disparate models still fit the data to acceptable levels. Nevertheless, constraints are improved dramatically for  $V_s$  (e), and less significantly for  $V_p$  (d) and layer thickness (f). Panel (g) shows the parameter correlation matrix, in which relative correlations are reduced with respect to the single functional case (Fig. 2.4f), indicating greater parameter independence and stronger constraints on individual (rather than combinations of) parameters.

Despite being imperfect, the sampling we achieve may be sufficient for our purposes, and the most important point is that the model parameter correlation matrix provides an estimate of the strength of constraints imposed by data.

### *Synthetic Tests*

To evaluate the performance of VFSA and associated statistical assessment tools, synthetic tests have been performed in which synthetic dispersion curves and receiver functions (both PRFs and SRFs) were calculated from the ak135 1-D velocity model. A model space was constructed in which ten layers in which each layer ranged over -20% to +20% perturbations to Poisson's ratio,  $V_s$ , and layer thickness of ak135 and a search guided by VFSA was conducted. The final, best-fit models' dispersion curves and receiver functions match their synthetic counterparts closely, but not exactly. Fits to a single functional (e.g., PRF alone), to two functionals (e.g., PRF and SW), and to three functionals (e.g., PRF, SW, and SRF), are shown in Figures 2.4(a), 2.5(a-b), and 2.6(a-c), respectively. The best-fitting models for each of the individual cases are shown in Figures 2.4(b), 2.5(c), and 2.6(d). After analysing PPDs for single (PRF alone; Figures 2.4(c), 2.4(d) and 2.4(e)), double (PRF and SW; Figures 2.5(d), 2.5(e) and 2.5(f)) and triple (PRF, SRF, and SW; Figures 2.6(e), 2.6(f) and 2.6(g)) functional cases, we find that  $V_p$ ,  $V_s$  and layer thickness are constrained more uniquely in the triple functional case than in the single and double functional cases, as indicated by narrower peaks for the triple functional case.  $V_p$  and  $V_s$  PPDs show several broad peaks while multiple, broad peaks can be seen in thickness PPDs for most layers in fits to one and two data functionals.

### Synthetics for all functionals

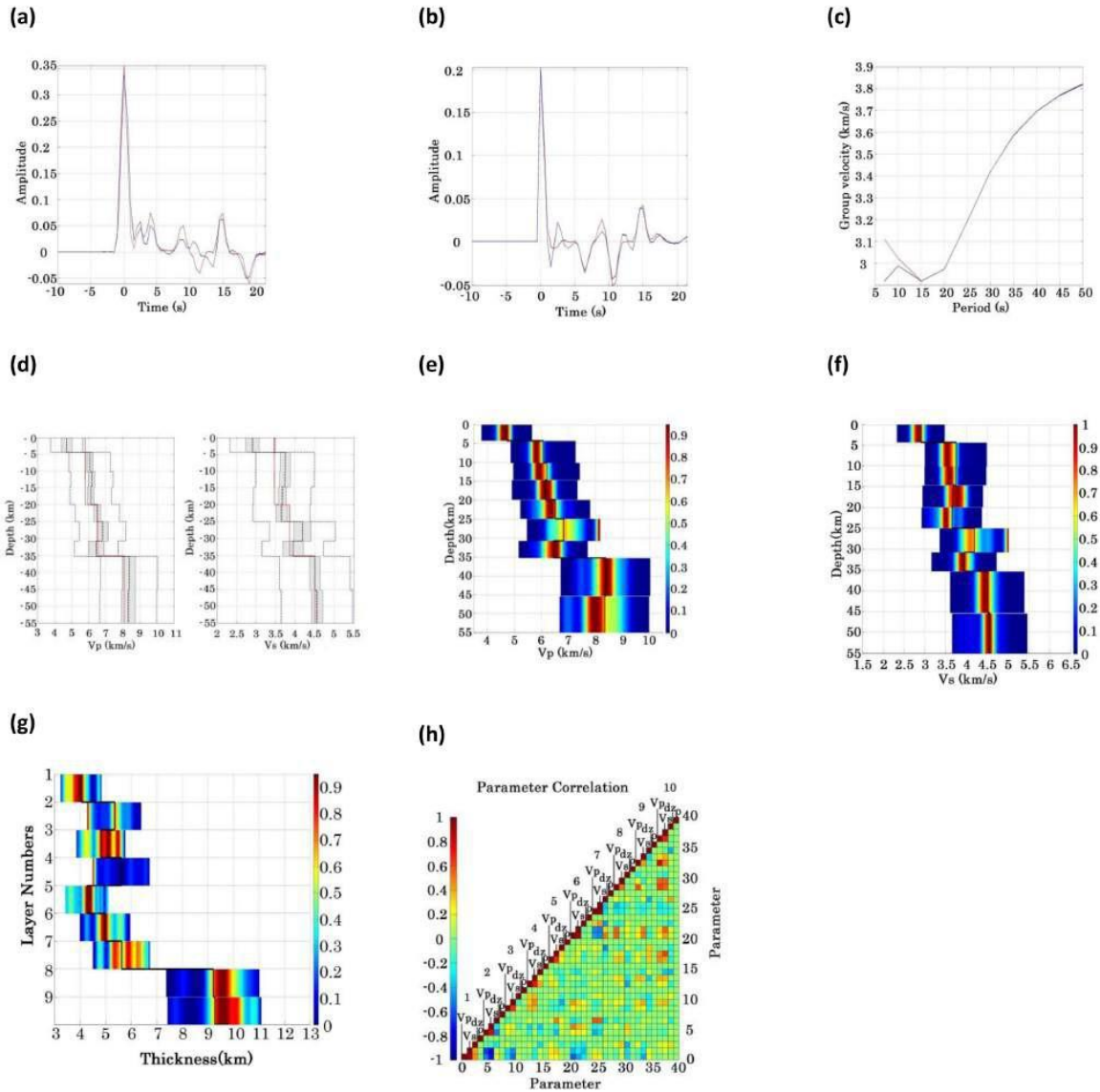


Figure 2.6 Panels (a), (b) and (c) show fits for modelling all data functionals jointly. (d) Shows the inverted  $V_p$  and  $V_s$  velocity profiles. Panels (e), (f) and (g) indicate that fitting the SRF in addition to the PRF and SW functionals increases the uniqueness of the model, as shown by much narrower peaks in the  $V_p$ ,  $V_s$  and layer thickness PPDs. This case shows the strongest constraints overall but the improvement is most significant for  $V_p$ . There is little improvement in  $V_s$  constraints, likely because the SRF is more sensitive to  $V_p$  than to  $V_s$ . This case also shows reduced correlations between model parameters (h). Lower trade-off values between layers in the mantle (layers 8–10) reflects the greater sensitivity of SRF to these depths.

However, PPD peaks for the two-functional case are generally sharper (less broad) than are corresponding peaks for the single functional case, indicating that jointly fitting two functionals produces a more unique solution.

Further, we find that the data functionals constrain shear wave velocity structure better than compressional wave velocity structure, as indicated by narrower peaks in Figures 2.4(d), 2.5(e), and 2.6(f) compared to Figures 2.4(c), 2.5(d), and 2.6(e).

The parameter correlation matrix for the single functional case (Figure 2.4(f)) has high positive tradeoff values, which indicates greater dependence of model parameters. Jointly fitting two (Fig. 2.5(g)) and three (Fig. 2.6(h)) functionals results in lower correlations between parameters, in general, indicating that individual parameters are better constrained. Tradeoff values for layers in the mantle are reduced significantly by jointly fitting the SRF (Fig. 2.6(h)).

These tests demonstrate that VFSA performance was satisfactory, even though we search a broad swath of model parameter space and we select starting models at random from within the input search bounds.

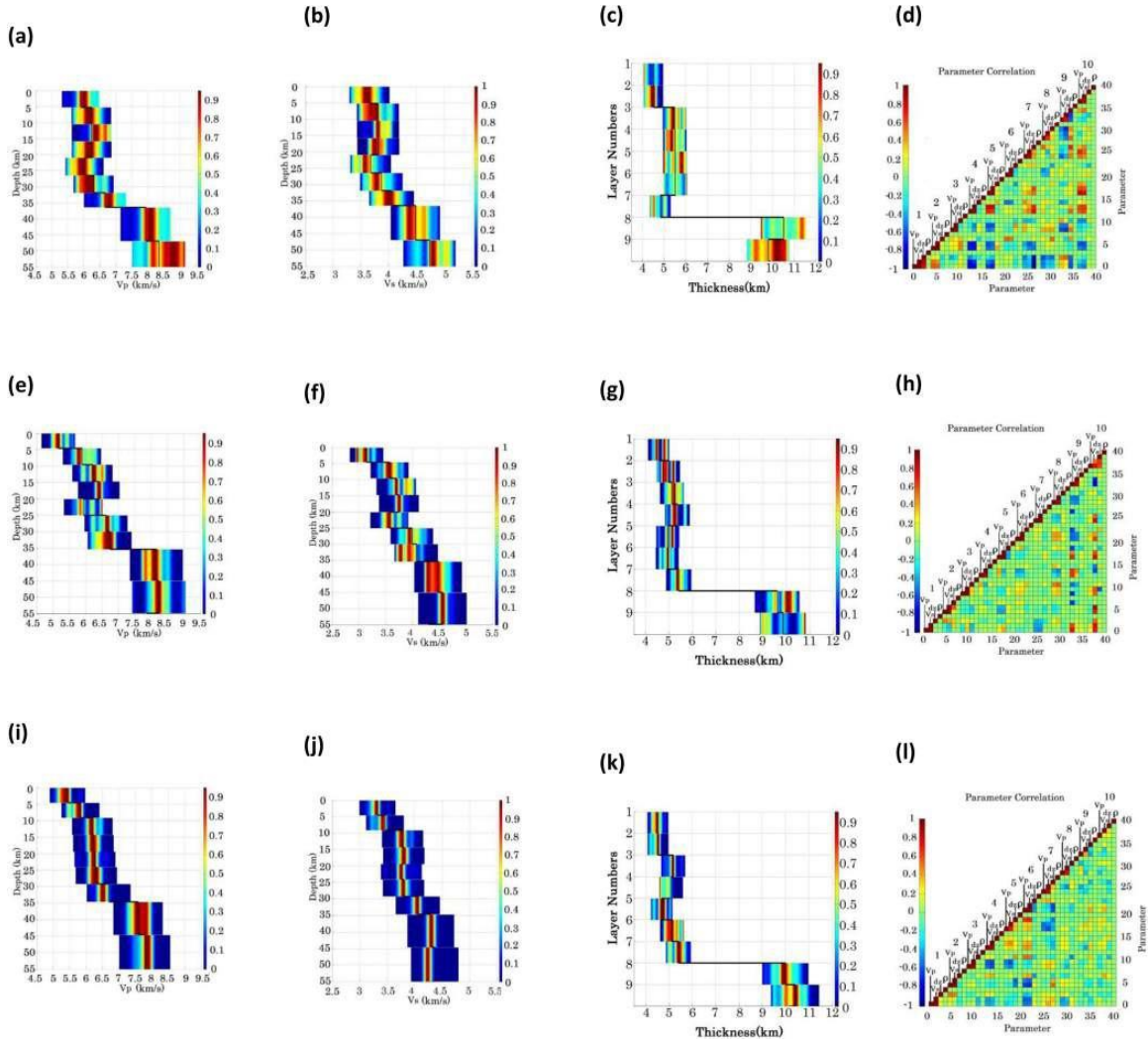


Figure 2.7 Plot of marginal posterior probability density (PPD) functions of  $V_p$ ,  $V_s$  and layer thickness, and the parameter correlation matrix for (a)–(d): single data functional, (e)–(h): two data functionals, (i)–(l): three data functionals for station S02. Panels (m)–(o) compare the observed (red) and synthetic (blue) data functionals for the Ps receiver function, Sp receiver function, and surface wave dispersion, respectively. Panel (p) shows the single best-fitting model (dashed black line), the reference Earth model (ak135, red line) and the model search space, which is  $\pm 10$  per cent (dashed blue line) of the best-fitting model. Shaded portion in panel (p) represents one standard error of the best-fitting model. See text for further details.

### Data Example

Based on fitting multiple data functionals for station S02 (in Oman) we observe some variability among models that fit the data acceptably. Hence we use statistical tools to describe the range of models that fit the data to acceptable levels

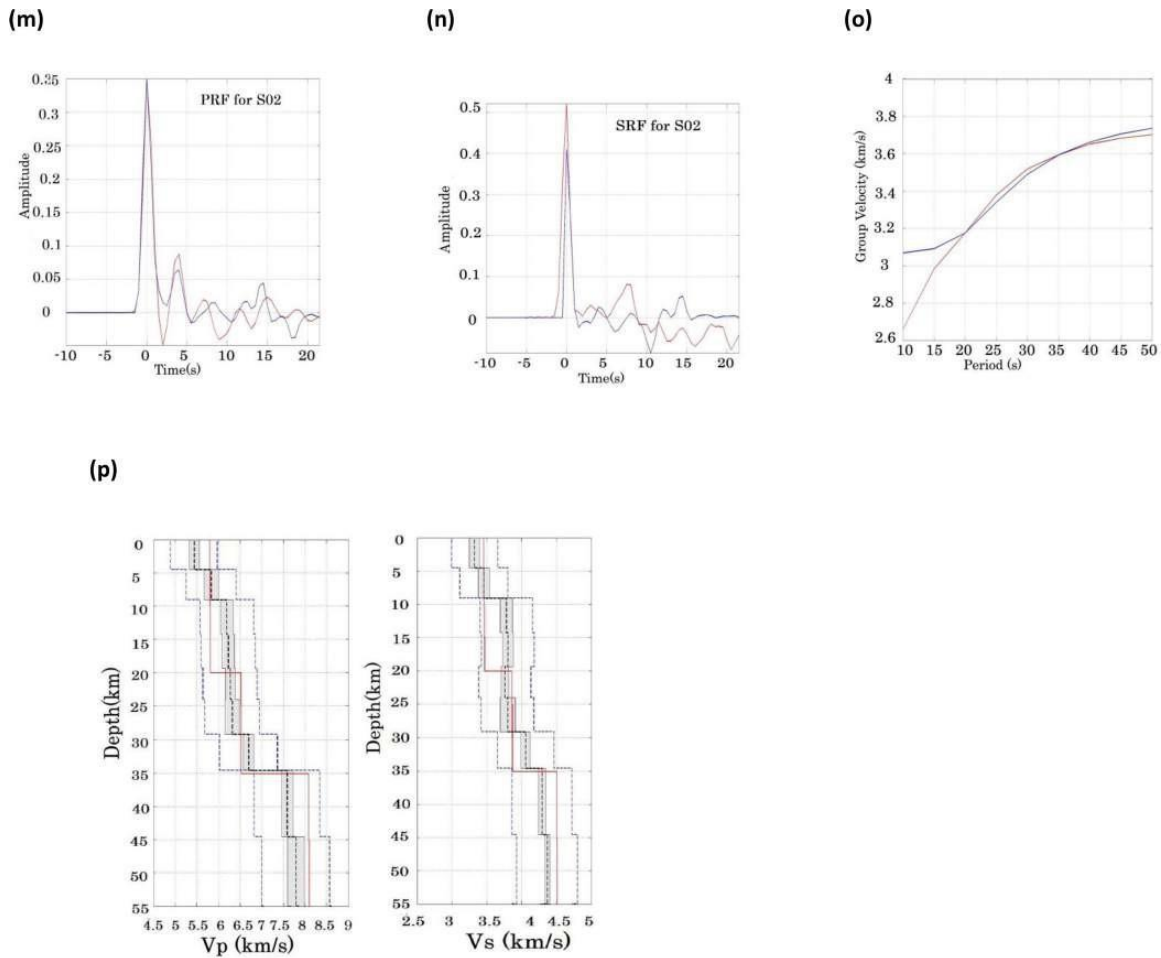


Figure 2.7 (Continued)

(marginal posterior probability density functions) and to characterize the independence of model parameter estimates (model parameter correlation matrix).

*Single Data Functional:* Figures 2.7 (a-d) show results for fits made to just a single functional (i.e., only PRFs). Note the relatively poor constraint of  $V_p$  with respect to  $V_s$  for this single data functional fit. Figures 2.7(a) & 2.7(b) show several disparate peaks for most layers, plus one layer at 50 km depth where the PPD for  $V_p$  “ $V_p$  PPD” shows a very broad peak, indicating a high level of uncertainty. The layers for which our results show single peaks have moderately wide regions of higher probability (hotter colors), indicating non-uniqueness and, therefore, inadequate constraints on those parameters. Most of the layers (layer no. 1, 2, 6, 7 and 8) do not show highly peaked PPD values for best-fit layer thicknesses, suggesting that the PRF alone imposes weak constraints on that parameter (Figure 2.7(c)).

Figure 2.7(d) shows the parameter correlation matrix. Green colors indicate that model parameters are constrained independently, except in the case of density. Density is coded to be a free parameter but, due to poor constraint in general, is held constant in the modeling presented here. Red and blue colors indicate strong positive and negative correlations between model parameters, respectively, which means that those parameters are not constrained independently. Note the widespread appearance of highly correlated model parameters in the parameter correlation matrix that corresponds to modeling PRFs alone. Our expectation is that adding additional functionals will decrease model parameter correlations and increase the peakedness of  $V_s$ ,  $V_p$  and thickness PPDs.

*Two Data Functionals:* Figures 2.7(e-h) show assessments that result from jointly fitting a  $P_s$  receiver function and a Rayleigh wave group velocity dispersion curve. The PPDs (Figures 2.7(e), 2.7(f) and 2.7(g)) indicate that the range of acceptable models has been reduced, compared to the single-functional case, as is indicated by narrower peaks for

high probability values of  $V_p$ ,  $V_s$  and thickness. While non-uniqueness has generally decreased, the  $V_p$  PPD (Figure 2.7(e)) shows two distinct peaks for the 3<sup>rd</sup> and 8<sup>th</sup> layers. Likewise, the  $V_s$  PPD (Figure 2.7(f)) shows distinct peak values for the 1<sup>st</sup> and 7<sup>th</sup> layers. Also, double peaks were found for the top two layers and no high peak value for the deepest layer in the layer thickness PPD (Figure 2.7(g)). Moreover, we observe a broad region of high PPD velocity values for the layer at 40 km depth, indicating that inclusion of more data functionals may still benefit the constraints imposed by these two data functionals. The parameter correlation matrix (Figure 2.7(h)) shows greater independence of model parameters in shallower layers, indicating that constraints on parameters have improved significantly with the addition of surface wave data.

*Three Data Functionals:* Figures 2.7(i-l) show results for the case in which all three data functionals are fit jointly. PPDs for this case show the strongest constraints for  $V_p$ ,  $V_s$  and thickness: a significant reduction in non-uniqueness with respect to single and double data functionals cases. Note that the PPD for  $V_s$  shows narrower and consistently single-valued peaks at every depth interval than for  $V_p$  (Figures 2.7(i) and 2.7(j)). This is characteristic of the great majority of our results and is ultimately due to the physics of seismic wave propagation, namely the weaker sensitivity of PRFs and Rayleigh wave dispersion data to  $V_p$  than to  $V_s$ . The layer thickness PPD found from joint modeling of all data functionals shows significant improvement over the one- and two-functional cases, as indicated by narrower peaks of high probability regions (Figure 2.7(k)). The parameter correlation matrix (Figure 2.7(l)) shows an improvement at deeper depths, which likely results from the longer wavelengths of SRFs, which limit their sensitivity to crustal structure and render them most useful for constraining structure at and below the

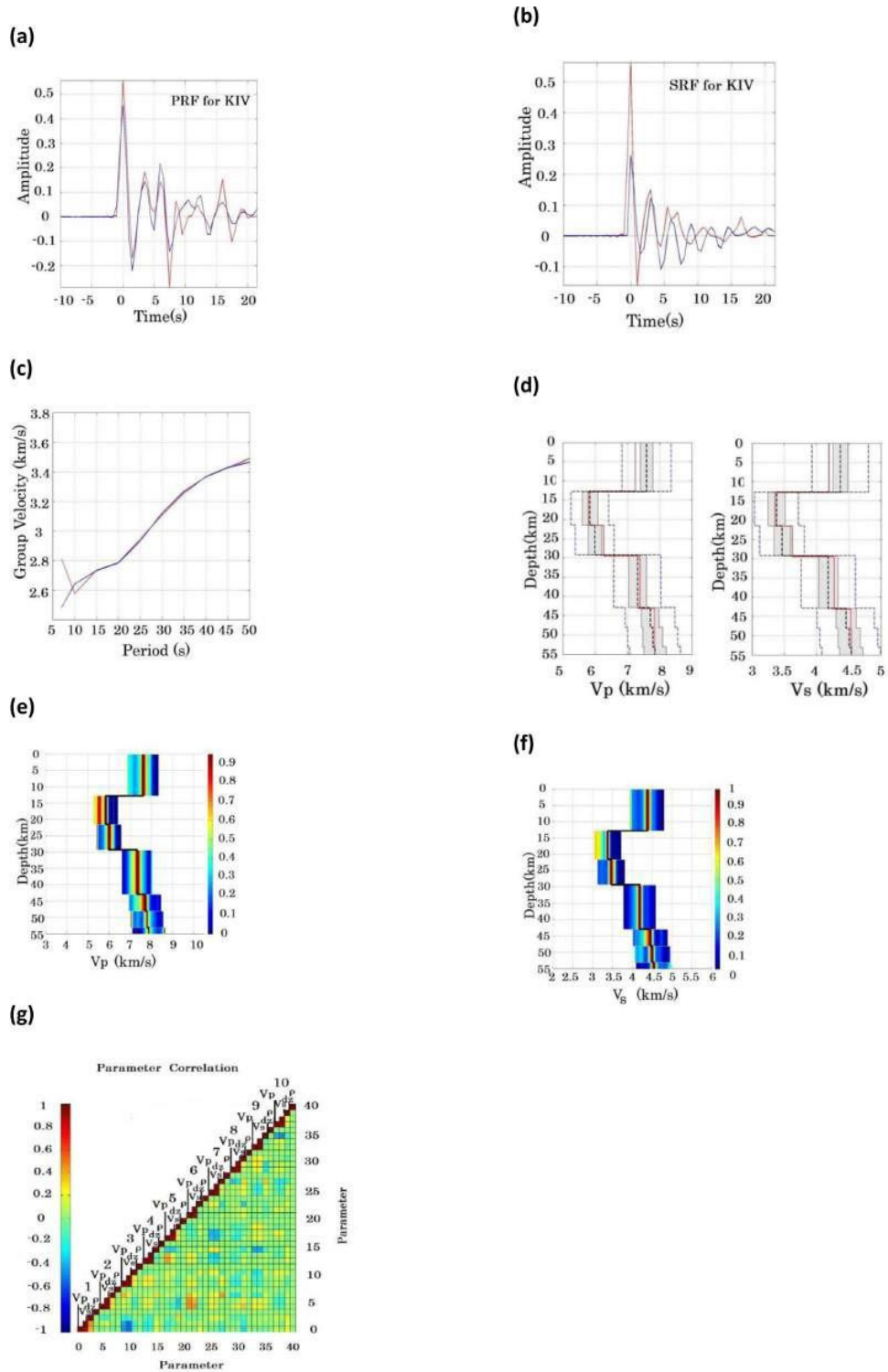


Figure 2.8. (a)–(c) Data functional matches for station KIV and (e)–(g) corresponding PPDs and the parameter correlation matrix. Panel (d) represents the best-fitting models (dashed black line) and initial model from Sandvol *et al.* (1998) (red line), along with one standard error of the best-fitting model (shaded portion). All colours and symbols are the same as in Fig. 2.7.

Moho. However, the independence of shallower layers has degraded with respect to the two-functional case and this highlights an important result. SRFs are generally noisier than PRFs and show greater variability, perhaps because they can be computed reliably for a narrower range of epicentral distances than can PRFs, so each station's dataset typically contains many fewer SRFs than PRFs. While jointly modeling PRFs and surface wave dispersion almost always improves the constraints on models, as evaluated by PPDs and parameter correlation matrices, adding SRFs often produces mixed results. The important point is that the assessment tools described here can identify cases in which the inclusion of distinct but complementary data functionals reduces non-uniqueness in modeling. Figures 2.7(m-o) show joint fits to all three data functionals; Figure 2.7(p) shows velocity models for  $V_p$  and  $V_s$ . Shaded portions in figures for velocity models indicate the error range in terms of one standard error around the best-fit model.

#### *Joint Modeling of the Crust and Uppermost Mantle beneath the Middle East*

A total of eleven velocity models were produced by MOOS for locations that correspond to broadband seismic stations distributed across the Middle East, as discussed above. The models were grouped into seven regions: eastern Turkey, Cyprus, southern Russia (in greater Caucasus), Iran, Saudi Arabia, Oman, and Djibouti. Models were inspected visually to identify the Moho, based on significant changes in shear wave and compressional wave velocities between layers. In figures (2.8 to 2.17) that illustrate data fits for each station, blue and red waveforms represent synthetic and observed data functionals respectively. Best matches between synthetics and data were analysed based on a "wiggle to wiggle" basis, in which arrival times of wiggles in synthetics were evaluated with respect to arrival times in observed receiver functions. Since the cost

function we minimize in MOOS represents the normalized cross-correlation of observed and computed waveforms, we do not expect to fit the amplitudes in receiver functions. We made this choice of cost function for several reasons, including robustness in trials with real and synthetic data and the observation that amplitudes of receiver functions depend critically on choices made in deconvolution and can vary significantly due to lateral variations in Earth structure that are not parameterized in our model. We encourage our readers to look at supplementary figures for thickness PPDs of all the investigated seismic stations in Middle East.

### *Southern Russia*

Broadband digital seismic station KIV is located in the northern Caucasus, where a very low mid-crustal velocity zone was found in earlier studies (Sandvol *et al.* 1998; Gök *et al.* 2011). Our results also confirm the possibility of this pronounced mid-crustal low velocity zone. We show fits to Ps and Sp receiver functions and Rayleigh wave group velocity dispersion curve in Figures 2.8(a), 2.8(b) and 2.8(c) respectively. Figures 2.8(e-g) show the PPDs and correlation matrix. Geologically, KIV is situated in the northern part of the greater Caucasus which is basically a thrust-and-fold belt where significant deformation is occurring between the Eurasian and Arabian plates. Previous studies have suggested that subduction is occurring under the Greater Caucasus (Khain & Lobkovskiy 1994; Vernant & Chery 2006). A dense population of low tradeoff values in the parameter correlation matrix shows that the model parameters are constrained independently, indicating fairly high uniqueness. We are able to obtain a best-fit model that is fairly unique, as is indicated by single, peaked PPD values, except for few layers that show relatively greater widths of higher probability regions (e.g., layers at 15 km and 45 km

depths). Comparatively larger numbers of velocity estimates are possible for those particular layers, and hence contribute to increased uncertainties associated with the model. Velocity estimates reported by Sandvol *et al.* (1998) fall into higher probability regions in our PPD, although our “best-fit” models differ in some respects from theirs. For example, Figure 2.8(d) shows that shear wave velocities between ~22 km and ~43 km depth differ from  $V_s$  estimates of Sandvol *et al.* (1998), but Figure 2.8(f) shows that their  $V_s$  estimates are included in higher probability regions of the PPD. Our shear wave velocity model (Figure 2.8(d)) indicates a crustal thickness of approximately ~43 km beneath this station, which is consistent with the Moho depth estimate of Sandvol *et al.* (1998). P- and S-wave velocities in the crust beneath this station range from 5.8-7.3 km/s and 3.4-4.2 km/s, respectively, and a distinct low velocity zone below ~12 km depth can also be seen, which is also consistent with the result of Sandvol *et al.* (1998). This may be due to the presence of a relatively young volcano, which may imply the existence of partial melt associated with a mid-crustal pluton related to recent subduction in Greater Caucasus (Cermak *et al.* 1987). High heat flow in the Greater Caucasus and a very large velocity contrast is consistent with the existence of a magma chamber. A previous structural geology study indicated that a large nappe root is thought to underlie the Greater Caucasus; the top of this root, at the contact of the pre-Jurassic basement and Jurassic slates and shale would produce a negative impedance contrast (Dotduyev 1986).

### *Djibouti*

Station ATD is located at an elevation of 610 m, within the Afar depression on the southern edge of Gulf of Tadjoura, where the Gulf of Aden ridge joins the East African

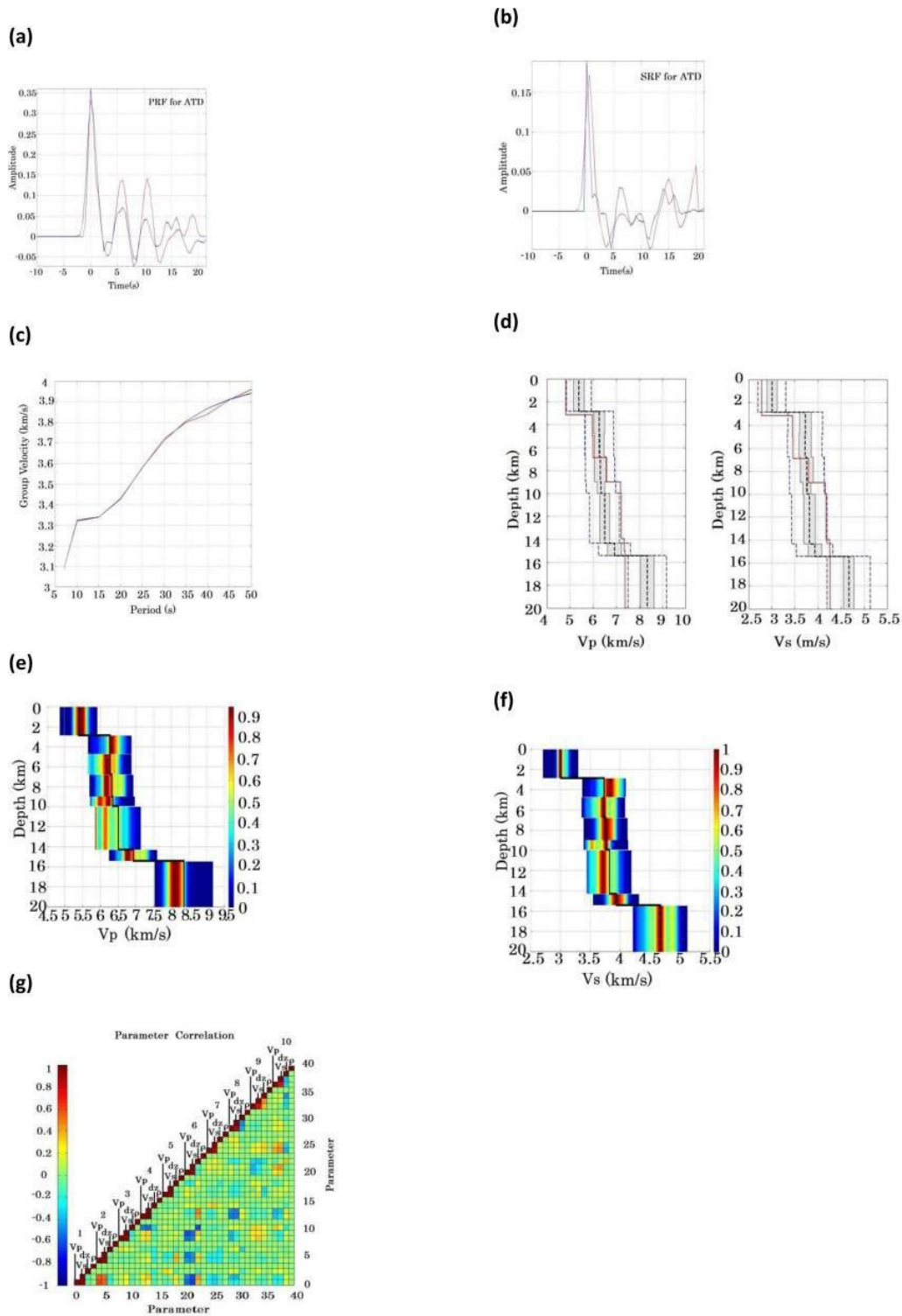


Figure 2.9 (a)–(c) Data functional matches for station ATD; (d) represents the best-fitting model (dashed black line) and initial model from Sandvol *et al.* (1998) (red line) along with one standard error of best-fitting model. Panels (e)–(g) represent PPDs and parameter correlation matrix. All colours and symbols are same as in Fig. 2.7.

rift (Courtilot 1980). Significant variations in estimates of crustal thickness can be seen in previous studies of this station (e.g., Ruegg 1975; Sandvol *et al.* 1998; Dugda & Nyblade 2006; among others). A Moho depth of about 8 km was estimated by Sandvol *et al.* (1998), by means of Ps receiver functions alone. A deep sounding experiment interpreted the depth of the Moho to be 10 km (Ruegg 1975). Also, more recently, a Moho depth of approximately 22-25 km was estimated beneath this station by H- $\kappa$  stacking and joint, linear inversion of Ps receiver functions and Rayleigh wave group velocity dispersion curves (Dugda & Nyblade 2006). We estimate crustal thickness to be about  $\sim$ 15km, where a sharp increase in the velocity gradient with depth can be identified in the velocity models. Fits to each data functional are shown in Figures 2.9(a-c) while results for Vp and Vs models with corresponding PPDs and parameter correlation matrix are shown in Figure 2.9(d) and Figures 2.9(e-g), respectively. In Figure 2.9(d), the dashed black line represents the best-fit model and the red line represents the velocity estimates produced by Sandvol *et al.* (1998). For some depths our velocity estimates are consistent with Sandvol *et al.* (1998) but they differ slightly in the upper crust and in uppermost mantle. Moreover, PPD includes the velocity estimates of Sandvol *et al.* (1998), wherever our best-fit model departs from their estimates (Figures 2.9(e) and 2.9(f)). Vp and Vs in the crust range between 5.3-6.9 km/s and 3.0-3.8 km/s, respectively. A dense distribution of off-diagonal correlation values (widespread dark blue color) between model parameters represents a high degree of model parameter dependence, however, broad and multiple peaks in the marginal posterior probability density functions for P- and S-wave velocities indicate a high level of non-uniqueness, as well. Vp is poorly constrained in

layer 6, as indicated by multiple low amplitude peaks in the PPD (Figure 2.9(e)) and relatively high negative tradeoffs with respect to other layers (Figure 2.9(g)).

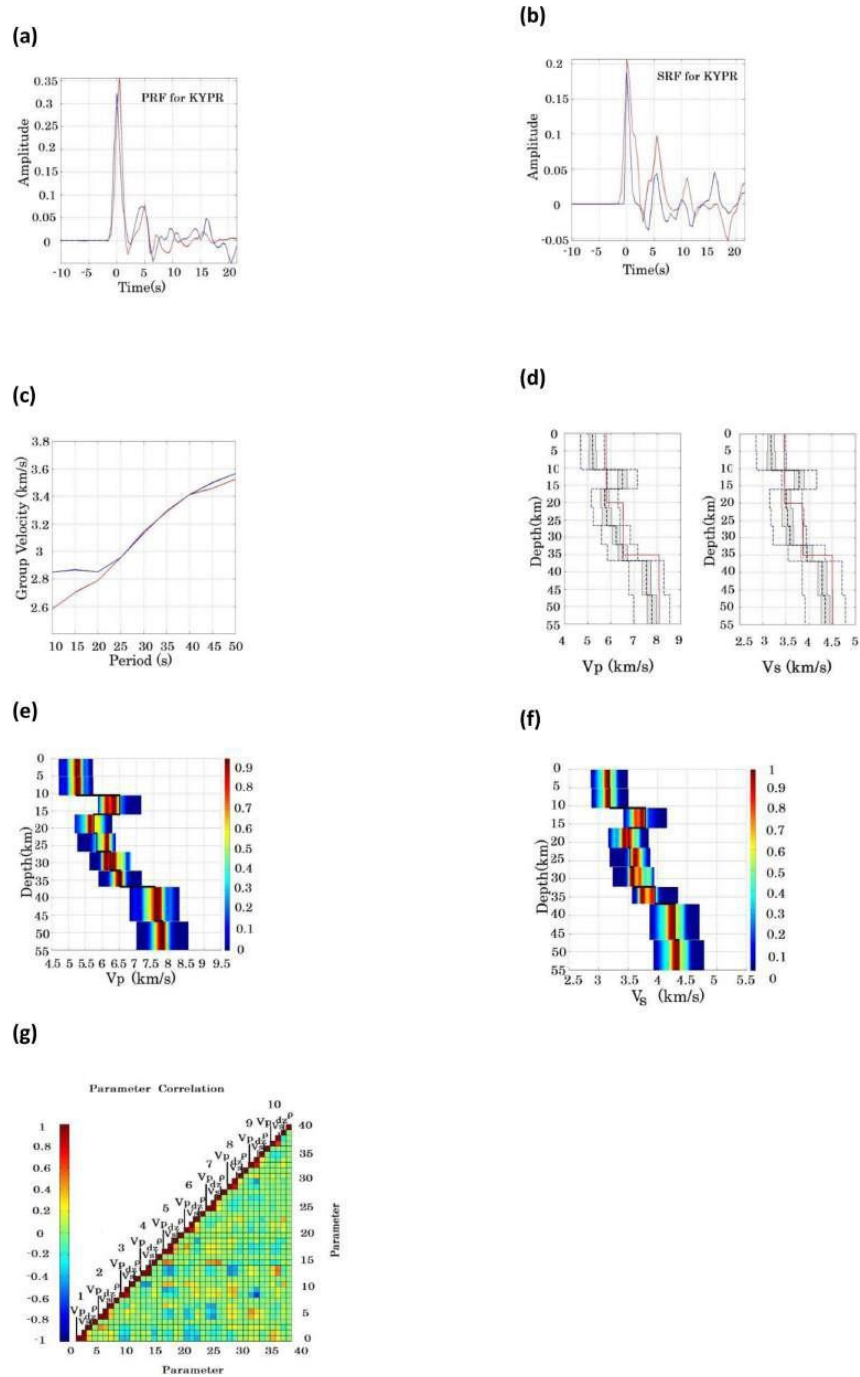


Figure 2.10. (a)–(c) Fits for data functionals and (d)–(g) corresponding best-fitting  $V_p$  and  $V_s$  models, PPDs, and parameter correlation matrix for station KYPR. All symbols and colours are same as in Fig. 2.7.

### *Eastern Turkey*

The region encompassing Eastern Turkey includes the seismic stations KYPR, DYBR, AGIN, and BTLS (Figure 2.1). The Eastern Turkey seismic experiment (ETSE) was carried out in order to determine crustal structure beneath the Anatolian plateau and these stations, which operated for 22 months in 1999-2001, were part of that study (Al-Lazki *et al.* 2003; Gök *et al.* 2000, 2003; Sandvol *et al.* 2003). The region investigated in eastern Turkey has several important tectonic features: the Anatolian microplate, the Pontides, the Bitlis suture, the eastern Anatolian fault zone, the Arabian plate, and the north Anatolian fault zone. Fits for data functionals are shown in Figures 2.10(a-c) for station KYPR. Based on our results, we estimate crustal thickness of  $\sim 37$  km beneath station KYPR (Figure 2.10(d)). We also find a  $\sim 6$  km thick high velocity zone ( $\sim 6.6$  km/s for  $V_p$  and  $\sim 3.8$  km/s for  $V_s$ ) below  $\sim 10$  km depth, which is consistent with the results of previous studies (e.g. Zor *et al.* 2003; Sengor & Kidd 1979; Dewey *et al.* 1986). Crustal P- and S-wave velocities in the proximity of this station lie between 5.1-6.5 km/s and 3.2-3.9 km/s, respectively. In Figure 2.10(d) the blue dashed line represents the upper and lower bounds of 10% around the best-fit model (black dashed line), within which marginal posterior probability density functions and the parameter correlation matrix were computed. The shading shows the range within one standard error of the best-fit model. The black solid line on PPDs (Figures 2.10(e-f)) indicates the best-fit model. As can be seen in PPDs for  $V_p$  and  $V_s$ , the higher probability region is confined to a narrow band of the model space for most layers, mostly near the best-fit model, indicating that the model found by MOOS is well-constrained, fairly unique, and reliable. However, the third, sixth, and seventh layers in our PPDs could still benefit from additional constraints.

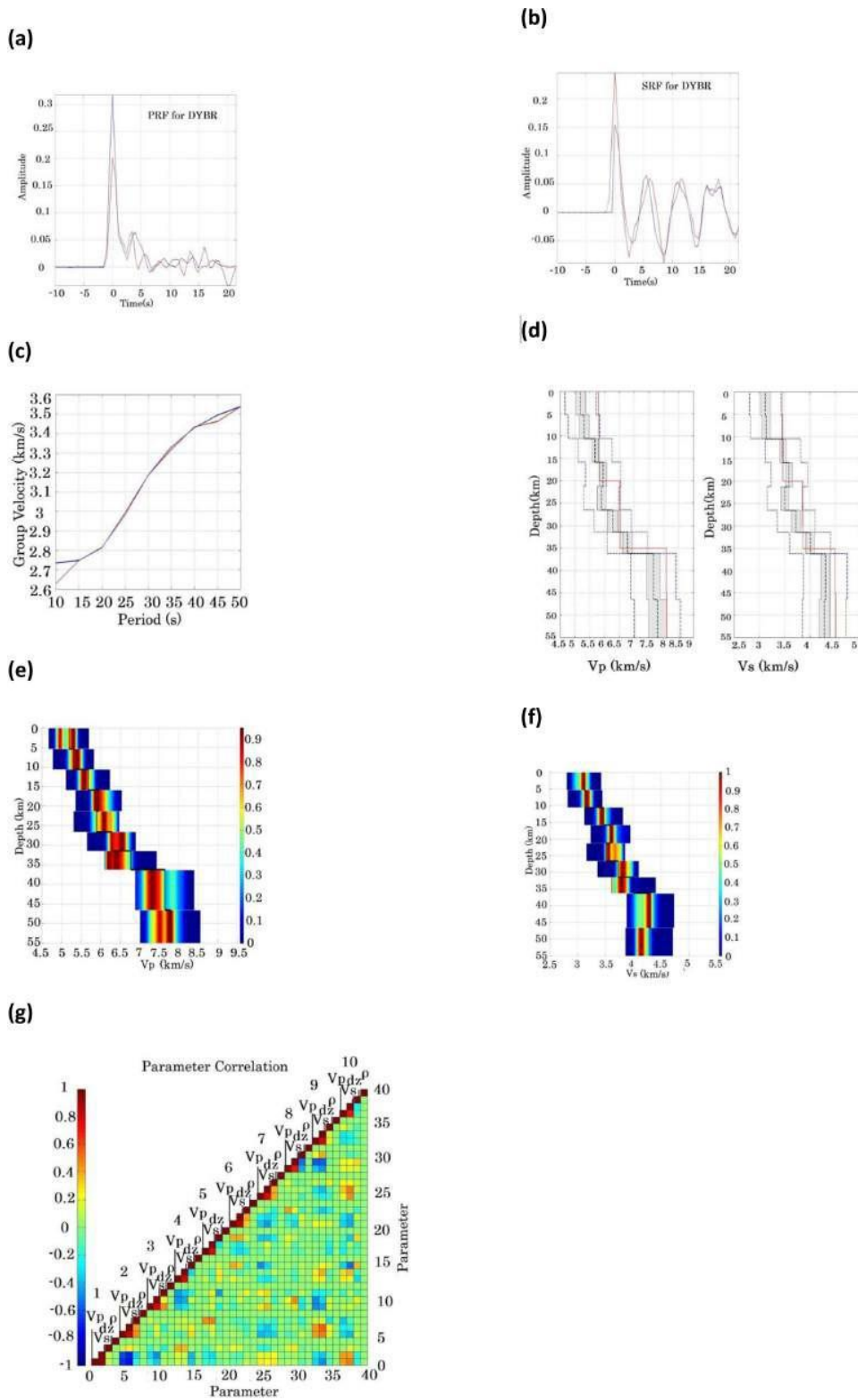


Figure 2.11 (a)–(c) Receiver functions and Rayleigh wave dispersion fits for station DYBR; corresponding best-fitting velocity models are shown in (d). PPDs and parameter correlation matrix are in (e)–(g). All symbols and colours are the same as in Fig. 2.7.

Lower tradeoff values in the parameter correlation matrix (Figure 2.10(g)) also indicate that the model we find is fairly unique and well-constrained.

Note that there are some layers for which velocities of the best-fit solution do not lie in the “high probability” region of the PPDs (red color). The “high probability” regions simply reflect the fact that the majority of models that fit the data acceptably have values in that range. The best-fit model, i.e., the model that explains the observations better than all other models, need not trace the highest probability region from layer to layer.

Station DYBR is located southwest of station KYPR at an elevation of 619 m. Fits for data functionals are shown in Figures 2.11(a-c) for station DYBR. Results for station DYBR indicate that the depth of the Moho should be ~36 km, which matches the estimates of  $\sim 33.7 \pm 1.0$  km results produced earlier (Ozacar 2007). The velocity structure beneath station DYBR is relatively simple, showing a gradational increase in P- and S-wave velocities with depth, except for the layer at 25 km depth. Crustal P- and S-wave velocities range from 5.2-6.8 km/s and 3.2-4.0 km/s, respectively (Figure 2.11(d)). Increasing “peakedness” (or “narrowness”) of the high probability region in the Vs PPD indicates that the non-uniqueness of the model is fairly small and therefore that constraints are strong (Figures 2.11(e) and 2.11(f)). Lower tradeoffs between model parameters also confirm this result (Figure 2.11(g)).

We found the depth of the Moho beneath seismic stations AGIN and BTLS to be 37 km and 36 km, respectively, which is consistent with previous results (Ozacar 2007). Average crustal thicknesses at each station location are compiled in Table 2.1. Fits for data functionals for station AGIN are shown in Figures 2.12(a-c). Crustal P- and S-wave

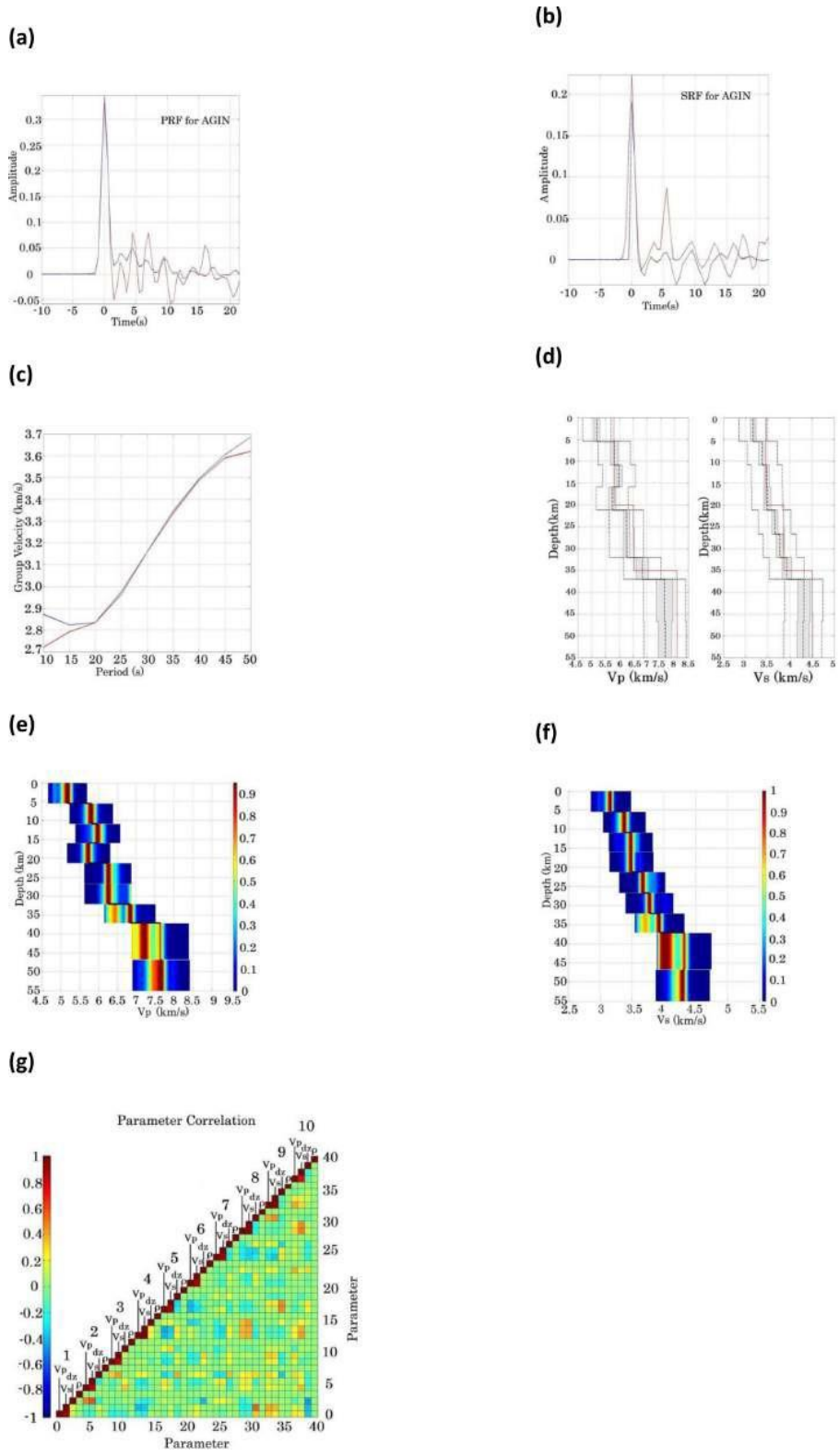


Figure 2.12 (a)–(g) Best-fitting velocity models, data functional matches and corresponding uncertainties for station AGIN. All symbols and colours are the same as in Fig. 2.7.

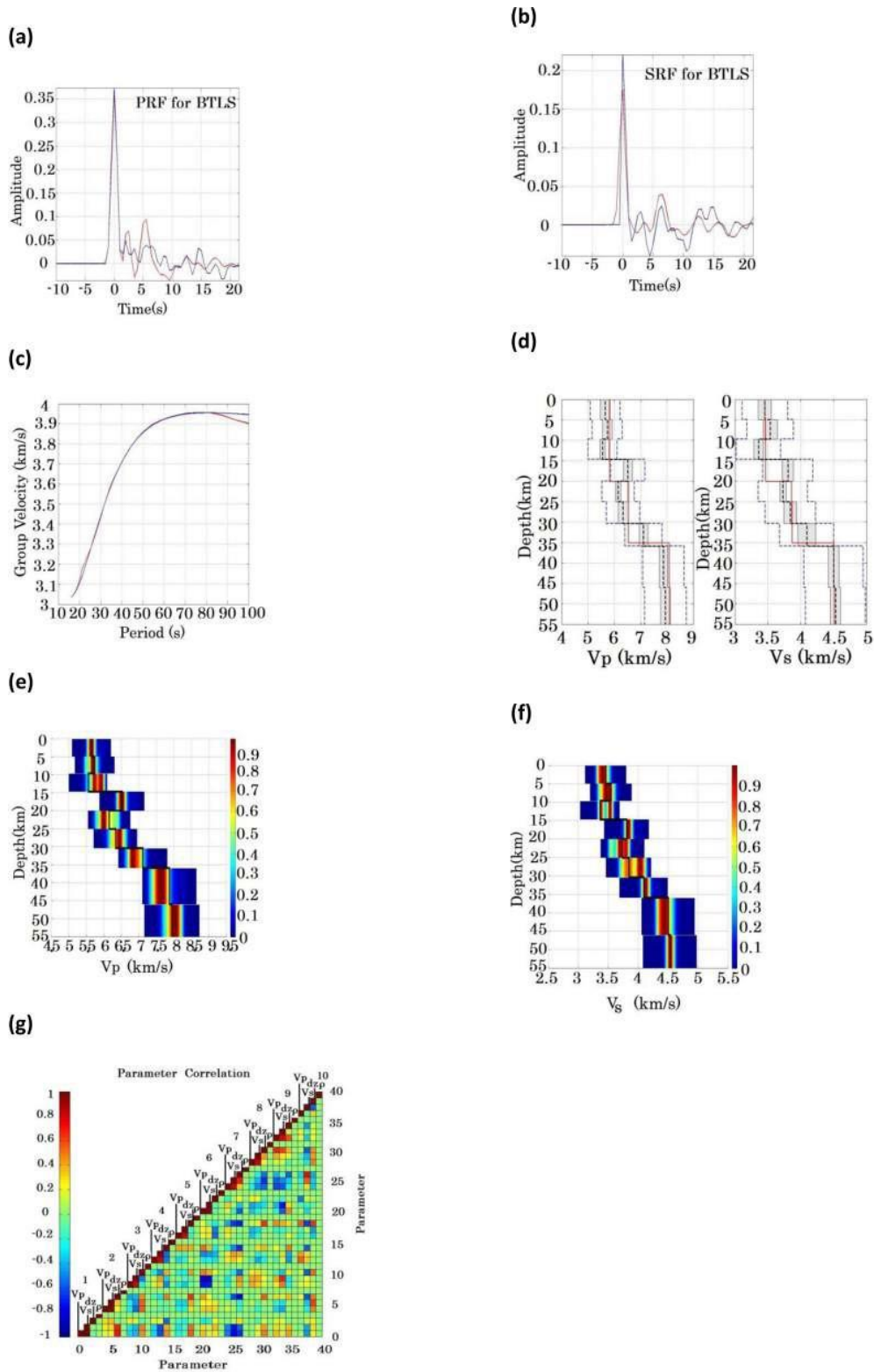


Figure 2.13 (a)–(g) Computed and observed data functional fits, best-fitting velocity models, PPDs and parameter correlation matrix for station BTLS. All symbols and colours represent same as in Fig. 2.7.

velocities range from 5.2-6.8 km/s and 3.2-3.9 km/s, respectively (Figure 2.12(d)). We also noticed a low velocity zone for  $V_p$  ( $\sim 5.7$  km/s of 6 km thickness) at 20 km depth. PPD values are generally single-peaked, except between  $\sim 32$  km and  $\sim 55$  km depth (Figures 2.12(e-f)). The parameter correlation matrix shows low tradeoffs between model parameters, indicating a fairly well-constrained model (Figure 2.12(g)). Matches for receiver functions and the dispersion curve are shown in Figures 2.13(a-c) for station BTLS. Beneath this station, crustal P- and S-wave velocities range between 5.6-7.1 km/s and 3.6-4.1 km/s respectively (Figure 2.13(d)). Here we observe low velocity zones for both  $V_p$  and  $V_s$  at depths of 12 km and 22 km, respectively, consistent with other models for seismic stations in eastern Turkey. The presence of a low velocity zone beneath these seismic stations may confirm the presence of young basaltic volcanics in the region, as reported by Zor *et al.* (2003). PPD peaks for  $V_p$  are generally narrow and single-valued, except for two peaks at 12 km depth and relatively broader peaks for layers beneath the Moho (Figure 2.13 (e)). The  $V_s$  PPD seems to indicate that  $V_s$  is less well-constrained, because multiple and/or broad peaks appear for most layers (Figure 2.13(f)). PPD results seem to be consistent with higher tradeoffs in the corresponding parameter correlation matrix, which shows that model parameters could still benefit from additional constraints (Figure 2.13(g)).

### *Cyprus*

Station CSS is located on the eastern flank of the ophiolitic outcrop of the Troodos Massif on Cyprus, in the Mediterranean Sea (Robertson 2000). The central part of Cyprus comprises complex geological structure, including a 6-8-km-thick ophiolitic sequence and crust that is approximately 20-25 km thick (Hofstetter & Bock 2004;

Makris & Wang 1995). Data functional matches, along with uncertainty estimates, are shown in Figure 14. Earlier receiver function studies (e.g., Vanacore *et al.* 2013; Hofstetter & Bock 2004) and tomography results (Koulakov & Sobolev 2006) estimate the depth of the Moho to be 30-33 km, which is consistent with our modeled crustal thickness of ~35 km (Figure 2.14(d)). Our velocity estimates are fairly similar to those published by Hofstetter et al. (2004), represented by the dot-dashed black line in Figure 2.14(d), except for some portions of the upper and lower crust. We also observe an anomalously high velocity zone of ~5 km thickness beginning at ~5 km depth, for which P- and S-wave velocities are found to be near about 6.6 km/s and 4.0 km/s, respectively. Crustal P- and S-wave velocities range from 5.1-6.7 km/s and 3.1-4.3 km/s, respectively. There appear to be a low velocity zone at 22 km depth both for  $V_p$  and  $V_s$ . Our model for seismic station CSS, also predicts a low velocity layer that has P- and S-wave velocities of ~7.7 and 4.2 km/s, in the uppermost mantle at 52 km depth. This anomalously slow layer may be due to the presence of altered lithospheric material beneath this seismic station. Higher tradeoff values in the upper crustal layers (Figure 2.14(g)) indicate fairly high levels of non-uniqueness in our models, especially for the 1<sup>st</sup> and 2<sup>nd</sup> layers, where multi-valued regions of higher probability can be seen in the PPDs (Figures 2.14(e) & 2.14(f)). But, in general, a narrower range of PPD values for  $V_s$  than for  $V_p$  shows that  $V_s$  is better constrained than  $V_p$  in almost all layers.

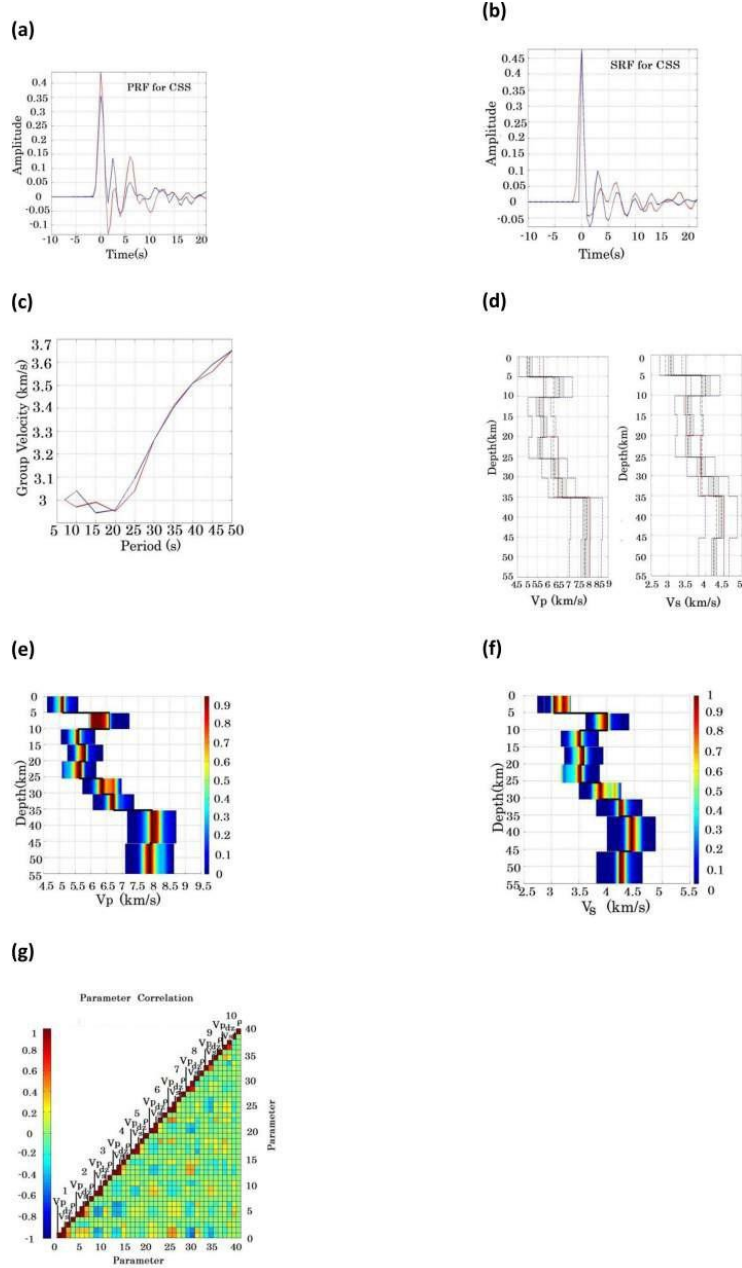


Figure 2.14. (a)–(c) Receiver functions and Rayleigh wave dispersion fits for station CSS (in Cyprus); corresponding best-fitting velocity models are shown in (d). PPDs and parameter correlation matrix are in (e)–(g). All symbols and colours are the same as in Fig. 2.7. In (d), the dot–dashed line represents velocity estimates published by Hofstetter & Bock (2004).

## Oman

Oman, in the southern part of the Arabian Peninsula, is surrounded by the Makran subduction zone and a divergent plate boundary (in the Gulf of Aden) to the south, the Oman Sea to the north, and a transform plate boundary (the Owen – Murray fracture zone) to the east. Shear and compressional wave velocity profiles were obtained for two seismic stations in Oman, S02 and S04, which belong to a temporary network of eleven broadband stations in the Dhofar area that were deployed in March 2003. In central Arabia, crust and uppermost mantle structure has been probed by many geophysical techniques (e.g. Al-Lazki *et al.* 2002; Al-Amri, 1998, 1999) but the structure beneath southern Oman has not received much attention. As a result, little is known about seismic velocities of the crust and uppermost mantle beneath the southern part of the Arabian plate.

S02 is located north of the city of Salalah on the Jabal Qara fault, which bounds the Salalah basin, and above a pre-rift sedimentary formation. Our best-fit model and associated uncertainties are shown in Figures 2.7(i-p).  $V_p$  and  $V_s$  values show a sharp increase at ~34 km, which we estimated as the depth of the Moho. Beneath station S02, crustal seismic velocity ranges are 5.4-6.6 km/s for  $V_p$  and 3.4-4.1 km/s for  $V_s$  (Figure 2.7(p)). PPDs for station S02 indicate that the  $V_p$ ,  $V_s$  and thickness models are subject to strong constraints (Figures 2.7(i), 2.7(j) and 2.7(k)), and this result is supported by lower tradeoff values in the parameter correlation matrix (Figure 2.7(l)).

Station S04 is located on pre-rift sediments in Rawya (Tiberi *et al.* 2006). We obtain a sharp increase in P- and S-wave velocities both at 25 km and 30 km depths, so

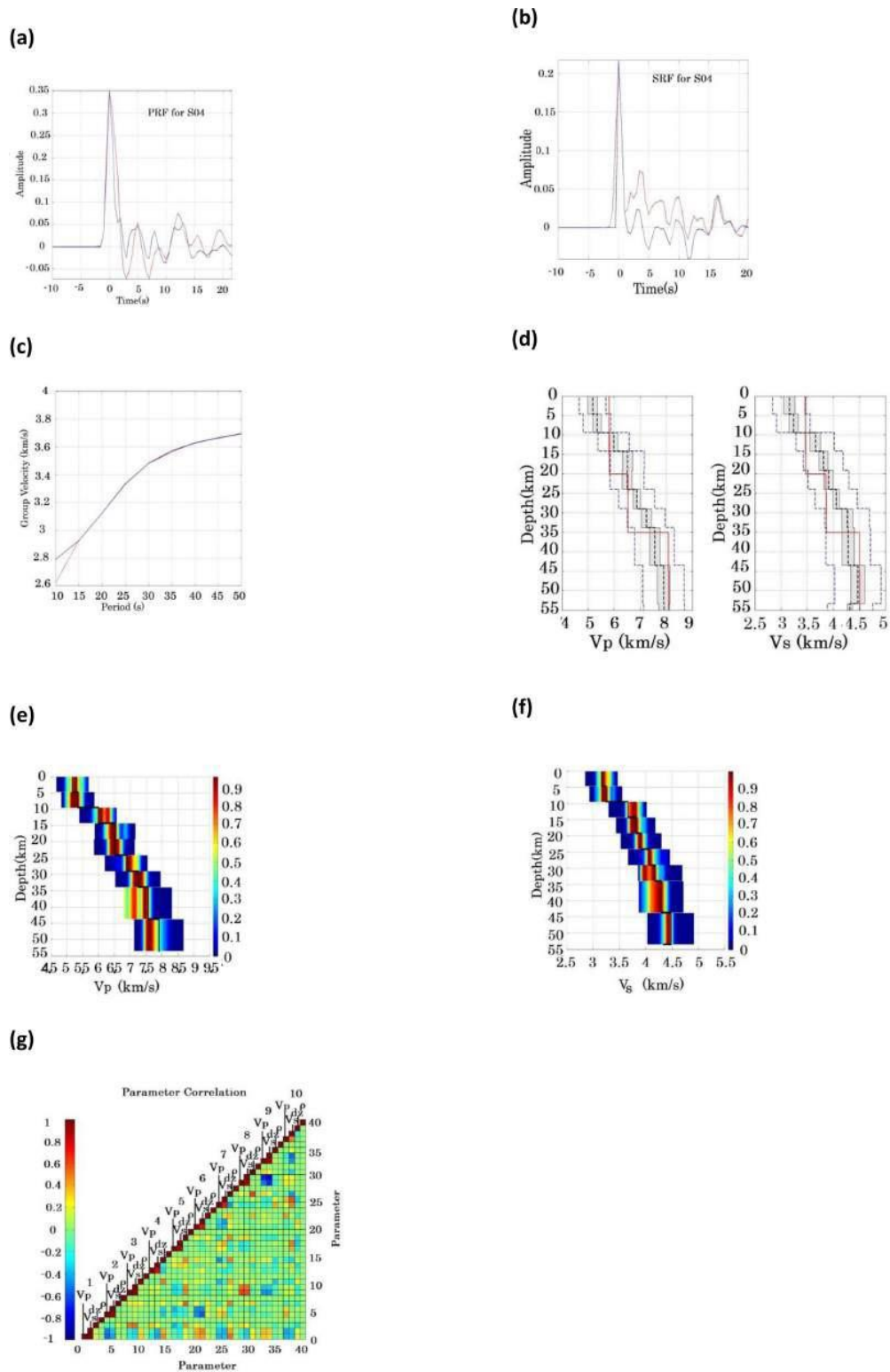


Figure 2.15 (a)–(g) Computed and observed data functional fits, best-fitting velocity models, PPDs and correlation matrix for station S04. All symbols and colours are same as in Fig. 2.7.

our estimate for Moho depth beneath this station varies from 25 km to 30 km, which is consistent with estimates of previously published studies (e.g. Tiberi *et al.* 2006). Fits for data functionals are shown in Figures 2.15(a-c). Crustal P- and S-wave velocities ranges are 5.2-6.8 km/s and 3.3-4.1 km/s, respectively (Figure 2.15(d)). The PPD plot for P-wave velocity shows greater uncertainties than S-wave velocity (Figures 2.15(e) and 2.15(f)). We are able to obtain fairly sharp, single-valued peaks for  $V_p$  and  $V_s$  for intra-crustal layers, except for layers at 12 km and 30 km depths. However, P- and S-wave profiles below the Moho still need additional constraints, as indicated by the appearance of multiple peaks in the PPDs.

### *Iran*

Seismic station D2, located in Iran, was one of a set of temporary seismic stations installed during the Central Zagros experiment “Zagros01” and operated from November 2000 to April 2001 (Paul *et al.* 2006). Zagros01 stations extended from the Persian Gulf (Bushehr) to the central region of Iran (Posht-e-Badam) (Paul *et al.* 2010). Station D2 was located on the northeastern segment of the Zagros01 profile which crosses the southwestern part of the central Iranian micro-continent (CIMC) block (Paul *et al.* 2006). Most of the published work concerning subsurface structure in this region relies either on Bouger anomaly modeling or on seismic reflection experiments (e.g. Blanc *et al.* 2003; McQuarrie *et al.* 2004; Sherkati & Letouzey 2004). Paul *et al.* (2006) estimated the depth of the Moho beneath the CIMC to be ~41 km from P-receiver functions alone. Our modeling results estimate a crustal thickness of ~39 km beneath this station. Fits for data functionals are shown in Figures 2.16(a-c). Figure 2.16(d) shows that crustal P- and S-wave velocity beneath station D2 ranges between 5.2-6.2 km/s and 3.2-3.8 km/s,

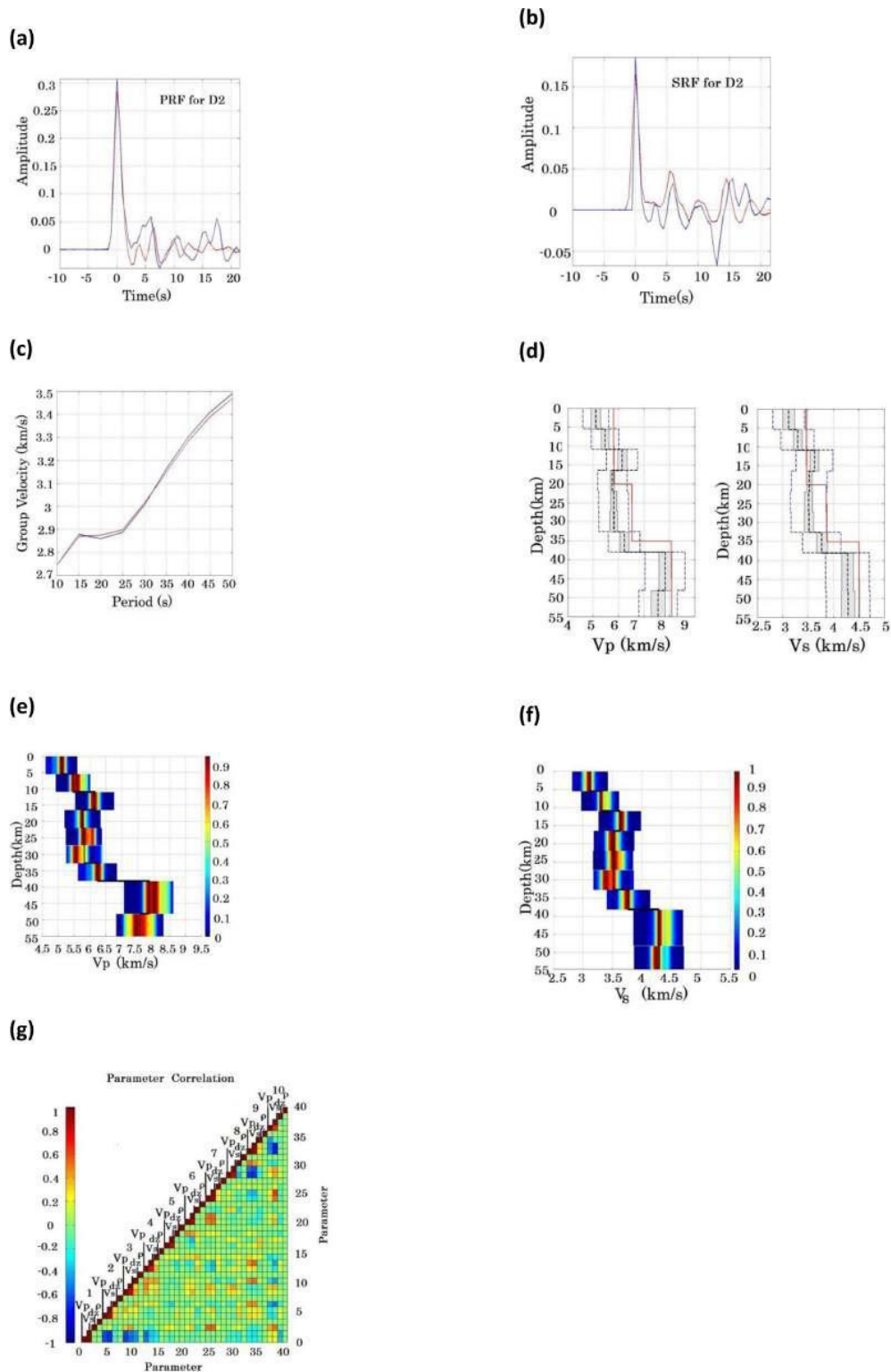


Figure 2.16 (a)–(g) Computed and observed data functional fits, best-fitting velocity models, PPDs and correlation matrix for station D2 (in Iran). All symbols and colours represent same as in Fig. 2.7.

respectively. In addition, a relatively sharp increase in P-wave velocity (5.5 km/s to 6.2 km/s) and S-wave velocity (3.2 km/s to 3.6 km/s) is observed at 12 km depth, indicating the possible existence of a midcrustal Conrad discontinuity at this depth.

PPD values (Figure 2.16) show that the  $V_p$  and  $V_s$  velocity profiles are fairly well-constrained, with stronger constraints on  $V_s$  than on  $V_p$ . For example, MOOS could not identify well-constrained values for  $V_p$  and  $V_s$  at 25 km and 35 km depths, respectively. The layers at 45 km and 50 km depths show significant variations in  $V_p$  even though the  $V_s$  values for the same layers are better constrained. This is an expected result for fits to group velocity dispersion and  $P_s$  receiver functions because both functionals are more sensitive to  $V_s$  than to  $V_p$ . The correlation plot (Figure 2.16(g)) shows fairly low tradeoffs for the majority of the crust and uppermost mantle, with the exception of the shallowest layer and layers just below the Moho.

### *Saudi Arabia*

Station RAYN (Ar Rayn, Saudi Arabia), on the eastern edge of the Arabian shield, is situated on an exposed corner of the Ar-Rayn terrane that is mostly covered by sediments. Fits for data functionals are fairly good (Figures 2.17(a-c)); we estimate the Moho to be ~45 km beneath RAYN, as indicated by large increases in both  $V_p$  and  $V_s$ .

Single-peaked values for most of the layers in PPDs indicate that our data functionals generally constrain crustal and uppermost mantle structure well, especially for  $V_s$ , although constraints on  $V_p$  at depths of 22 km and 32 km (see Figures 2.17(e-f)) are poor. Our PPDs for  $V_s$  indicate multiple peaks for layers four and six. Levin & Park (2000) report the Moho to be at 41 km depth, while a depth of ~44 km was reported by Al-Damegh *et al.* (2005); both studies modeled  $P_s$  receiver functions only. We estimate

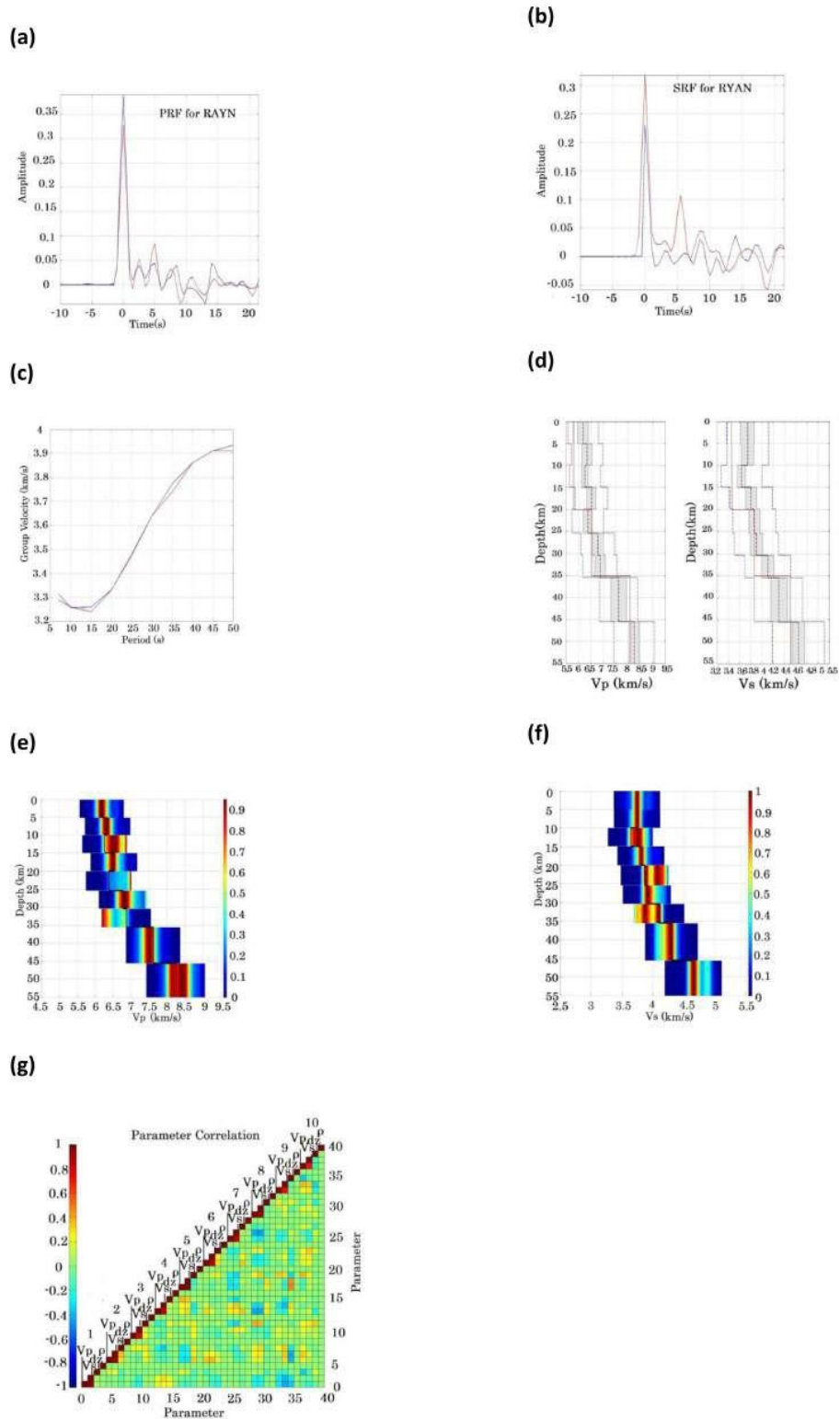


Figure 2.17 (a)–(c) Receiver functions and Rayleigh wave dispersion fits for station RAYN (in Saudi Arabia); corresponding best-fitting velocity models are shown in (d). PPDs and parameter correlation matrix are in (e–g). All symbols and colours are the same as in Fig. 2.7.

the Moho depth at approximately 45 km beneath RAYN, as indicated by a large increase in  $V_p$  and  $V_s$  (Figure 2.17(d)). P- and S-wave velocities in crust range from 6.2-6.8 km/s and 3.6-4.3 km/s respectively beneath this station. Lower tradeoff values in the parameter correlation matrix, both for crust and uppermost mantle, indicate that the datasets constrain the structure fairly well (Figure 2.17(g)).

### *Discussion and Conclusion*

We estimate crustal and uppermost mantle structure beneath eleven stations in the Middle East and adjoining areas by jointly modeling seismic data functionals, including  $P_s$  receiver functions,  $S_p$  receiver functions, and Rayleigh wave group velocity dispersion curves. We demonstrate the usefulness of a joint modeling technique namely MOOS (Multi-Objective Optimization for Seismology) by assessing the constraints imposed on model parameters using statistical tools. These tools include marginal Posterior Probability Density (PPD) functions for each independent parameter and model parameter correlation matrix. We estimate these assessment tools using the products of a broad search of the model space driven by a global nonlinear optimization technique called Very Fast Simulated Annealing (VFSA). Using these assessment tools, we also demonstrate cases in which the joint fitting of  $P_s$  and  $S_p$  receiver functions and Rayleigh wave group velocity dispersion curves provide better constraints of compressional wave velocity, shear wave velocities and thickness, reducing both the number of acceptable models and tradeoffs between model parameters, than does a single data functional. In addition to reducing non-uniqueness, the assessment tools have the potential to identify characteristics of acceptable models that are *required by* the data, rather than those that are simply *consistent with* the data.

Models obtained for seismic stations generally agree with estimates of  $V_p$  and  $V_s$  values from previously published receiver functions and surface wave dispersion studies. Crustal thicknesses vary in the region from  $\sim 15$  km beneath ATD, located in Djibouti, to  $\sim 45$  km beneath RAYN, in Saudi Arabia. Crustal P- and S-wave velocities range between 5.1-7.3 km/s and 3.0-4.3 km/s, respectively. Models obtained for station ATD are highly non-unique, which might be due to complex geological structure beneath the station or to high levels of noise in the data.  $V_s$  is generally more well-constrained than  $V_p$ , as indicated by nearly single-peaked values of PPDs for stations we investigated. In general, we found constraints to be less strong in deeper parts of the models than in shallower parts.

Assessments of modeling results are essential complements to single, best-fit models. They reveal cases in which modeling has been successful and can help guide the operator to additional data functionals that might provide useful additional constraints, and thereby reduce non-uniqueness and tradeoffs further. Relationships between physical parameters and geophysical observables are commonly nonlinear, so linear methods are likely to misidentify a model that represents a local minimum as the “true” model and to overestimate the degree of confidence one should have in that model. Further, global search methods that incorporate multiple data types should be preferred to linear methods that propose to model a single data functional.

#### *Acknowledgments*

We thank C.J. Ammon and R.B. Herrmann for making their codes available for the computation of receiver functions and surface wave dispersion and three anonymous reviewers for their constructive suggestions and criticism. We thank the Incorporated

Research Institutions for Seismology (IRIS), Geoscope, and GEOFON for their roles in acquiring, archiving, and disseminating broadband seismic data for the Middle East. This research was supported by funding from the National Nuclear Security Administration (Contract DE-AC52-09NA29327) and the W.M. Keck Foundation. This work was performed under the auspices of the U.S. Department of Energy by Lawrence Livermore National Laboratory under contract DE-AC52-07NA27344. This is LLNL contribution LLNL-JRNL-642041.

## References

- Agostinetti, N. P. & Malinverno, A., 2010. Receiver function inversion by trans-dimensional Monte Carlo sampling, *Geophys. J. Int.*, **181**, 858–872.
- Al-Amri, A.M., 1998. The crustal structure of the western Arabian platform from the spectral analysis of long-period P-wave amplitude ratios, *Tectonophysics*, **136**, 271–283.
- Al-Amri, A., 1999. The crustal and upper-mantle structure of the interior Arabian Platform. *Geophys. J. Int.*, **136**, 421–430.
- Al-Damegh, K., Sandvol, E. & Barazangi, M., 2005. Crustal structure of the Arabian Plate: new constraints from the analysis of teleseismic receiver functions, *Earth planet. Sci. Lett.*, **231**, 177–196.
- Al-Lazki, A., Seber, D., Sandvol, E., Turkelli, N., Mohamad, R. & Barazangi, M., 2003. Tomographic  $P_n$  velocity and anisotropy structure beneath the Anatolian plateau (eastern Turkey) and the surrounding regions, *Geophys. Res. Lett.*, **30**, 8043, doi:10.1029/2003GL017391.
- Al-Lazki, A. I., Sandvol, E., Seber, D., Barazangi, M., Turkelli, N. & Mohamad, R., 2004. On tomographic imaging of mantle lid velocity and anisotropy at the junction of the Arabian, Eurasian and African Plates, *Geophys. J. Int.*, **158**, 1024–1040, doi:10.1111/j.1365-246X.2004.02355.x.
- Al-Lazki, A.I., Seber, D., Sandvol, E. & Barazangi, M., 2002. A crustal transect across the Oman mountains of the eastern margin of Arabia, *GeoArabia*, **7**, 47–78.
- Ammon, C.J., 1997. An overview of receiver function analysis. <http://eqseis.geosc.psu.edu/~cammon/HTML/RftnDocs/rftn01.html>
- Ammon, C.J., Herrmann, R.B., Pasyanos, M.E, Walter, W.R, Sevilla, W. & Randall, G., 2005. Simultaneous Inversion of Receiver Functions and Surface-Wave Dispersion Measurements for Lithospheric Structure beneath Asia and North Africa, *Proc. 27th Seismic Research Review: Ground-Based Nuclear Explosion Monitoring Technologies*, Palm Springs, CA, pp. 3-12.
- Ammon, C.J., Kosarian, M., Herrmann, R.B, Pasyanos, M.E., Walter, W.R. & Tkalcic, H., 2004. Simultaneous Inversion of Receiver Functions, Multi-mode Dispersion, and Travel-time Tomography for Lithospheric Structure Beneath the Middle East and North Africa, *Proc. 26th Seismic Research Review - Trends in Nuclear Explosion Monitoring*, Orlando, FL, pp. 17-28.
- Ammon, C.J., Randall, G.E. & Zandt, G., 1990. On the non-uniqueness of receiver function inversions, *J. Geophys. Res.*, **95**: 15,303-15,318.

- Angus, D. A., Wilson, D.C., Sandvol, E. & Ni, J.F., 2006. Lithospheric structure of the Arabian and Eurasian collision zone in eastern Turkey from S-wave receiver functions, *Geophys. J. Int.*, **166**, 1335–1346, doi:10.1111/j.1365-246X.2006.03070.x.
- Barazangi, M., Sandvol, E. & Seber, D., 2006. Structure and tectonic evolution of the Anatolian plateau in eastern Turkey, *GSA Today*, **409**, 463–473.
- Blanc, E.J.P., Allen, M.B., Inger, S. & Hassani, H., 2003. Structural styles in the Zagros simple folded zone, *Iran, J. Struct. Geol.*, **160**, 401–412.
- Bodin, T., Sambridge, M., Tkalčić, H., Arroucau, P., Gallagher, K. & Rawlinson, N., 2012. Transdimensional inversion of receiver functions and surface wave dispersion. *J. Geophys. Res.*, **117**, B02301. doi:10.1029/2011JB008560.
- Bock, G., 1991. Long-period S to P converted waves and the onset of partial melting beneath Oahu, Hawaii, *Geophys. Res. Lett.*, **18**, 869–872.
- Cakir, O. & Erduran, M., 2004. Constraining crustal and uppermost mantle structure beneath station TBZ (Trabzon, Turkey) by receiver function and dispersion analyses, *Geophys. J. Int.*, **158**, 955-971.
- Cermak, V. & Rybach, L., 1987. *Terrestrial Heat Flow and the Lithosphere*, Springer-Verlag, New York.
- Chang, S.-J., Baag, C.-E. & Langston, C., 2004. Joint analysis of teleseismic receiver functions and surface wave dispersion using the genetic algorithm, *Bull. Seism. Soc. Am.*, **94**, 691-704.
- Clayton, R.W. & Wiggins, R.A., 1976. Source shape estimation and deconvolution of teleseismic body waves, *Geophys. J. Royal Astro. Soc.*, **47**, 151-177.
- Cochran, J. R., 1983. A model for development of Red Sea, *Am. Assoc. Pet. Geol.*, **67**, 41-69.
- Courtillot, V., 1980. Opening of the Gulf of Aden and Afar by progressive tearing, *Phys. Earth Planet. Int.*, **21**, 343–350.
- Davis, T. E. & Principe, J. C., 1991. A simulated annealing like convergence theory for the simple genetic algorithm, in *Proc. of the Fourth International Conference on Genetic Algorithms*, Morgan Kaufmann, San Mateo, California.
- Dewey, J. F. & Sengor, A.M.C., 1979. Aegean and surrounding regions: Complex multiplate and continuum tectonics in a convergent zone, *Geol. Soc. Am. Bull.*, **90**, 84-92.

- Dewey, J.F., Hempton, M.R., Kidd, W.S., SarogClu, F. & Sengor, A.M.C., 1986. Shortening of continental lithosphere: the neotectonics of Eastern Anatolia--a young collision zone, *Geol. Soc. Spec. Publ., London*, **19**, pp. 3–36.
- Dotduyev, S.I., 1986. The nappe structure of the Great Caucasus (in Russian), *Geotektonika*, **5**, 94-105.
- Dugda, M. & Nyblade, A.A., 2006. New constraints on crustal structure in eastern Afar from the analysis of receiver functions and surface wave dispersion in Djibouti, *Geol. Soc. Spec. Publ., London*, **259**, 239-251.
- Dziewonski, A., Bloch, S. & Landisman, M., 1969. Surface wave ray tracing azimuthal anisotropy: a generalized spherical harmonic approach technique for the analysis of transient seismic signals, *Bull. Seism. Soc. Am.*, **59**, 427-444.
- Faber, S. & Muller, G., 1980. Sp phases from the transition zone between the upper and lower mantle, *Bull. Seism. Soc. Am.*, **70**, 487-508.
- Farra, V. & Vinnik, L., 2000. Upper mantle stratification by P and S receiver functions, *Geophys. J. Int.*, **141**, 699-712.
- Forrest, S., 1993. Genetic algorithms: Principles of natural selection applied to computation, *Science*, **261**, 872-878.
- Gangopadhyay, A., Pulliam, J. & Sen, M.K., 2007. Waveform Modeling of Teleseismic S, SP, SsPmP, and Shear-Coupled PL Waves for Crust and Upper Mantle Velocity Structure Beneath Africa, *Geophys. J. Int.*, **170**: 1210–1226.
- Geman, S. & Geman, D., 1984. Stochastic relaxation, Gibbs distributions, and the Bayesian restoration of images, *IEEE Trans. Patt. Anan. Mac. Int.*, **6**, pp. 721–741.
- Gök, R., Sandvol, E., Türkelli, N., Seber, D. & Barazangi, M., 2003. Sn attenuation in the Anatolian and Iranian plateau and surrounding regions, *Geophys. Res. Lett.*, **30**, 8042, doi:10.1029/2003GL018020.
- Gök, R., Mellors, R.J, Sandvol, E., Pasyanos, M.E., Hauk, T., Takedatsu, R., Yetirmishli, G., Teoman, U., Turkelli, N., Godoladze, T. & Javakishvirli, Z., 2011. Lithospheric velocity structure of the Anatolian plateau–Caucasus–Caspian region, *J. Geophys. Res.*, **116**, p. B05303, doi: 10.1029/2009JB000837.
- Gök R., Pasyanos, M. & Zor, E., 2006. Lithospheric Structure of the Continent-Continent Collision Zone: Eastern Turkey, *Geophys. J. Int.*, **169**, 1079-1088.
- Gök, R., Mahdi, H., Al-Shukri, H. & Rodgers, A.J., 2007. Crustal structure of Iraq from receiver functions and surface wave dispersion: Implications for understanding the deformation history of the Arabian–Eurasian collision, *Geophys J. Int.* **172**, 1179–1187.

- Gök, R., Turkelli, N., Sandvol, E., Seber, D. & Barazangi, M., 2000. Regional wave propagation in Turkey and surrounding regions, *Geophys. Res. Lett.*, **27**, 429–432, doi:10.1029/1999GL008375.
- Green, P.J., 1995. Reversible jump Markov chain Monte Carlo computation and Bayesian model determination, *Biometrika*, **82(4)**, 711–732.
- Gurrola, H., Baker, E. & Minster, B., 1996. Resolution of Receiver Function waveforms and resulting limitations in the modeling of Earth structure, *Eos Trans. AGU*, **77**, 460.
- Hammersley, J.M. & Handscomb, D.C., 1964. *Monte Carlo Methods*, Chapman & Hall, London.
- Hauser, J., Dyer, K.M., Pasyanos, M.E., Bungum, H., Faleide, J.I., Clark, S.A. & Schweitzer, J., 2011. A probabilistic seismic model for the European Arctic, *J. Geophys. Res.*, **116**, B01303.
- Herrmann, R.B., 1973. Some aspects of band-pass filtering of surface waves, *Bull. Seism. Soc. Am.* **63**, 663-671.
- Herrmann, R.B., Ammon, C.J. & Julia, J., 2001. Application of joint receiver-function surface-wave dispersion for local structure in Eurasia, *Proceedings of the 23rd Seismic Research Review: Worldwide Monitoring of Nuclear Explosions*, Jackson, WY, pp. 46-54.
- Hofstetter, R. & Bock, G., 2004. Shear-wave velocity structure of the Sinai sub-plate from receiver function analysis, *Geophys. J. Int.*, **158**, 67 – 84.
- Holland, J. H., 1975. *Adaptation in Natural and Artificial Systems*, Univ. of Michigan Press, Ann Arbor, Michigan.
- Ingber, L., 1989. Very fast simulated reannealing, *Math. Comput. Modeling*, **12**, 967–993.
- Ingber, L., 1993. Simulated annealing: practice versus theory, *Math. Computer Modeling*, **18**, pp. 29–57.
- Julia, J., Ammon, C.J., Herrmann, R.B. & Correig, A.M., 2000. Joint inversions of receiver function and surface wave dispersion observations, *Geophys. J. Int.*, **143**, 99-112.
- Julia, J., Ammon, C.J. & Nyblade, A.A., 2005. Evidence for mafic lower crust in Tanzania, East Africa, from joint inversion of receiver functions and Rayleigh wave dispersion velocities, *Geophys. J. Int.*, **162**, 555-569.

- Kennett, B.L.N, Engdahl, E.R. & Buland, R., 1995. Constraints on seismic velocities in the Earth from traveltimes, *Geophys. J. Int.*, **122**, 108-124.
- Khain, V. E., & Lobkovskiy, L.I., 1994. Relict seismicity in the Alpine belt of Eurasia mode of occurrence, *Geotectonics, Engl. Transl.*, **28**, 192–198.
- Kikuchi, M. & Kanamori, H., 1982. Inversion of complex body waves, *Bull. Seism. Soc. Amer.*, **72**, 491-506.
- Kirkpatrick, S., Gelatt, C.D. & Vecch, M.P., 1983. *Optimization by Simulated Annealing*, Science, New Series, **220**, pp. 671-680.
- Korst, J. & Aarts, E.H.L., 1989. *Simulated annealing and Boltzmann machines: A stochastic approach to combinatorial optimization and neural computing*, Wiley, New York.
- Koulakov, I. & Sobolev, S.V., 2006. Moho depth and three-dimensional P and S structure of the crust and uppermost mantle in the Eastern Mediterranean and Middle East derived from tomographic inversion of local ISC data, *Geophys. J. Int.*, **164**, 218-235, doi:10.1111/j.1365-246X.2005.02791.x.
- Kumar, P., Yuan, X., Kind, R. & Kosarev, G., 2005a. The lithosphere-asthenosphere boundary in the Tien Shan-Karakoram region from S receiver functions: Evidence for continental subduction, *Geophys. Res. Lett.*, **32**.
- Kumar, P., Kind, R., Hanka, W., Wylegalla, K., Reigber, Ch., Yuan, X., Woelbern, I., Schwintzer, P., Fleming, K., Dahl-Jensen, T., Larsen, T.B., Schweitzer, J., Priestley, K., Gudmundsson, O. & Wolf, D., 2005b. The lithosphere asthenosphere boundary in the North-West Atlantic region, *Earth Planet. Sci. Lett.*, **236**, 249–257, doi:10.1016/j.epsl.2005.05.029.
- Lawrence, J.F. & Wiens, D.A., 2004. Combined Receiver-Function and Surface Wave Phase-Velocity Inversion Using a Niching Genetic Algorithm: Application to Patagonia, *Bull. Seism. Soc. Am.*, **94**: 977-987.
- Le Pichon, X. & Francheteau, J., 1978. A plate-tectonic analysis of the Red Sea - Gulf of Aden area, *Tectonophysics*, **46**, 369-406.
- Levin, V. & Park, J., 2000. Shear zones in the Proterozoic lithosphere of the Arabian shield and the nature of the Hales discontinuity, *Tectonophysics*, **323** , 131-148.
- Li, X., Kind, R., Yuan, X., Wolbern, I. & Hanka, W., 2004. Rejuvenation of the lithosphere by the Hawaiian plume, *Nature*, **427**, 827– 829.
- Ligorria, J.P. & Ammon, C., 1999. Iterative deconvolution and receiver function estimation, *Bull. Seism. Soc. Am.*, **89**, 1395-1400.

- Maggi, A. & Priestley, K., 2005. Surface waveform tomography of the Turkish-Iranian Plateau, *Geophys. J. Int.*, **160**, 1068–1080, doi:10.1111/j.1365-246X.2005.02505.x.
- Makris, J. & Wang, J., 1995. Geophysical study and geodynamics of the Eastern Mediterranean Sea, *Rep. 719/48–1, Inst. Geophys.*, Univ. of Hamburg, Hamburg.
- McQuarrie, N., Stock, J.M., Verdel, C. & Wernicke, B.P., 2004. Cenozoic evolution of Neotethys and implications for the causes of plate motions, *Geophys. Res. Lett.*, **30**, 2036, doi: 10.1029/2003GL017992
- Metropolis, N. & Ulam, S.M., 1949. The Monte Carlo method, *J. Am. Stat. Assoc.*, **44**, 335–341.
- Metropolis, N., Rosenbluth, A.W., Rosenbluth, M.N., Teller, A.H. & Teller, E., 1953. Equation of state calculations by fast computing machines, *J. Chem. Phys.*, **21**, 1087–1092.
- Mosegaard, K. & Tarantola, A., 1995. Monte Carlo sampling of solutions to inverse problems, *J. geophys. Res.*, **100**, 12 431–12 447.
- Ozacar, A.A., 2007. *Complex rupture processes of large strike slip earthquakes and receiver function analysis of crust and upper mantle in active tectonic settings*, PhD Thesis, University of Arizona, Arizona, USA.
- Ozacar, A. A., Gilbert, H. & Zandt, G., 2008. Upper mantle discontinuity structure beneath East Anatolian Plateau (Turkey) from receiver functions, *Earth Planet. Sci. Lett.*, **269**, 427–435, doi:10.1016/j.epsl.2008.02.036.
- Ozalaybey, S., Savage, M.K., Sheehan, A.F., Louie, J.N. & Brune, J.N., 1997. Shear-wave velocity structure in the northern Basin and Range province from the combined analysis of receiver functions and surface waves, *Bull. Seism. Soc. Am.*, **87**, 183-199.
- Pareto, V., 1906. *Manual of Political Economy* (1971 translation from 1927 edition). Augustus M.Kelley, New York, USA.
- Paul, A., Kaviani, A., Hatzfeld, D., Vergne, J. & Mokhtari, M., 2006. Seismological evidence for crustal-scale thrusting in the Zagros mountain belt (Iran), *Geophys. J. Int.*, **166**, 227-237, doi:10.1111/j.1365-246X.2006.02920.x.
- Paul, A., Kaviani, A., Hatzfeld, D., Mohammad, T. & Catherine, P., 2010. Seismic imaging of the lithospheric structure of the Zagros mountain belt (Iran), *Geol. Soc. London, Spec. Pub.*, Feb. 2012.

Pasyanos, M.E., Franz, G.A. & Ramirez, A.L., 2006. Reconciling a geophysical model to data using a Markov chain Monte Carlo algorithm: An application to the Yellow Sea-Korean Peninsula region, *J. Geophys. Res.*, **111**, B03313.

Pasyanos, M.E., 2005. A variable resolution surface wave dispersion study of Eurasia, North Africa, and surrounding regions, *J. Geophys. Res.*, **110**, B12301, doi:10.1029/2005JB003749.

Press, F., 1968. Earth models obtained by Monte Carlo inversion, *J. Geophys. Res.*, **73**, 5223–5234.

Press, W.H., Teukolsky, S.A., Vetterling, W.T., & Flannery, B.P., 2007. "Section 10.12. Simulated Annealing Methods". *Numerical Recipes: The Art of Scientific Computing* (3rd ed.). New York: Cambridge University Press.

Pulliam, J., Sen, M.K., Frohlich, C. & Grand, S., 2002. Waveform modeling of the crust and upper mantle using S, Sp, SsPmP and shear-coupled PL waves, *Proc. 24th Seis. Res. Rev. – Nuclear Explosion Monitoring: Innovation and Integration*, pp. 144–153.

Pulliam, J. & Sen, M.K., 2005. Assessing Uncertainties in Waveform Modeling of the Crust and Upper Mantle, *Proceedings of the 27th Seismic Research Review: Ground-Based Nuclear Explosion Monitoring Technologies*, Palm Springs, CA, pp. 152 – 160.

Pulliam, J., Sen, M.K. & Gangopadhyay, A., 2006. Determination of Crust and Upper Mantle Structure beneath Africa Using a Global Optimization-Based Waveform Modeling Technique, *Proceedings of the 28th Seismic Research Review: Ground-Based Nuclear Explosion Monitoring Technologies*, Orlando, FL, pp. 196-208.

Reilinger, R. & McClusky, S., 2011. Nubia–Arabia–Eurasia plate motions and the dynamics of Mediterranean and Middle East tectonics, *Geophys. J. Int.*, **186**, 971-979, DOI: 10.1111/j.1365-246X.2011.05133.x.

Robertson, A.H.F., 2000. Mesozoic-Tertiary tectonic-sedimentary evolution of a South Tethyan oceanic basin and its margins in Southern Turkey, *Geol. Soc. London, Spec. Pub.*, **173**, 97-138.

Ruegg, J.C., 1975. Main results about the crustal and upper mantle structure of the Djibouti region (T.F.A.I.), In: A. Pilger and A. Rosler (Editors). *Afar Depression of Ethiopia*, E. Schweizer. Verlagsbuchhandl. (Naegle u. Obermiller), Stuttgart, Federal Republic of Germany (DEU), 120–134.

Sambridge, M., 1998. Geophysical inversion with a neighborhood algorithm - II, Appraising the ensemble, *Geophys. J. Int.*, **138**, 727-746.

Sambridge, M., 1999. Geophysical inversion with a neighborhood algorithm - I, Searching a parameter space, *Geophys. J. Int.*, **138**, 479-494.

Sandvol, E., Seber, D., Calvert, A. & Barazangi, M., 1998. Grid search modeling of receiver functions: Implications for crustal structure in the Middle East and North Africa, *J. Geophys. Res.*, **103**, 26,899-26,917.

Sandvol, E., Turkelli, N., Zor, E., Gök, R., Bekler, T., Gurbuz, C., Seber, D. & Barazangi, M., 2003. Shear wave splitting in a young continent-continent collision: An example from Eastern Turkey, *Geophys. Res. Lett.*, **30**, 8041, doi:10.1029/2003GL017390.

Seber, D., Vallve, M., Sandvol, E., Steer, D. & M. Barazangi, 1997. Middle East Tectonics: Applications of Geographic Information Systems, GSA Today.

Sen, M.K. and Stoffa, P.L., 1996. Bayesian inference, Gibbs' sampler and uncertainty estimation in geophysical inversion, *Geophysical Prospecting*, **44**, 313-350.

Sen, M.K & Stoffa, P.L., 1995. *Global optimization methods in geophysical inversion*, Elsevier science publishing company, The Netherlands, 281pp.

Sengor, A. M. C. & Kidd, W. S. F., 1979. Post-collisional tectonics of the Turkish-Iranian plateau and a comparison with Tibet, *Tectonophysics*, **55**, 361-376.

Sheehan, A., Abers, G., Jones, C.H. & Lerner-Lam, A., 1995. Crustal thickness variations across the Rocky Mountain front from teleseismic receiver functions, *J. Geophys. Res.*, **100**, 20391-20404.

Shelton, A.W., 1990. The Interpretation of gravity data in Oman: constraints on the ophiolite emplacement mechanism, *The Geology and Tectonics of the Oman Region*, pp. 459-471, eds A.H.F. Robertson, M.P. Searle and A.C. Ries, Geol. Soc. Lond. Spec. Publ.No. 49.

Sherkati, S. & Letouzey, J., 2004. Variation of structural style and basin evolution in the central Zagros (Izeh zone and Dezful Embayment), Iran, *Marine and Petroleum Geology*, **21**, 535-554.

Szu, H. & Hartley, R., 1987. Fast simulated annealing, *Phys. Lett.*, **122A**, 157-62.

Tarantola, A., 1994. *Inverse Problem Theory: Methods for Data Fitting and Model Parameter Estimation*, Elsevier, Amsterdam, The Netherlands, 600 pp.

Tiberi, C., Leroy, S., D'Acremont, E., Bellahsen, N., Ebinger, C., Al-Lazki, A. & Pointu, A., 2006. Crustal geometry of the northeastern Gulf of Aden passive margin: localization of the deformation inferred from receiver function analysis, *Geophys. J. Int.* **168**, 1247-1260.

Tkalcic, H., Pasyanos, M.E., Rodgers, A.J., Gök, R., Walter, W.R. & Al-Amri, A., 2006. A multistep approach for joint modeling of surface wave dispersion and teleseismic

receiver functions: Implications for lithospheric structure of the Arabian Peninsula, *J. Geophys. Res.*, **111**(B11311): 10.1029/2005JB004130.

Türkoğlu, E., Unsworth, M., Çağlar, Ý. Tuncer, V. & Avşar, Ü. 2008. Lithospheric structure of the Arabia-Eurasia collision zone in eastern Anatolia: Magnetotelluric evidence for widespread weakening by fluids?, *Geology*, **36**, 619–622, doi:10.1130/G24683A.1.

Vanacore, E., Taymaz, T. & Saygin, E., 2013. Moho structure of the Anatolian plate from receiver function analysis, *Geophys. J. Int.*, **193**,329-337.

Vernant, P. & Chery, J., 2006. Low fault friction in Iran implies localized deformation for the Arabia-Eurasia collision zone, *Earth Planet. Sci. Lett.*, **246**, 197–206, doi:10.1016/j.epsl.2006.04.021.

Wiggins, R. A., 1969. Monte Carlo inversion of body wave observations, *J. Geophys. Res.*, **74**, 3171–3181.

Yuan, X., Kind, R., Li, X. & Wang, R., 2006. The S receiver functions: synthetics and data example, *Geophys. J. Int.*, **165**: 555-564.

Zhao, L.S., Sen, M.K., Stoffa, P. & Frohlich, C., 1996. Application of very fast simulated annealing to the determination of the crustal structure beneath Tibet, *Geophys. J. Int.*, **125**, 355-370.

Zor, E., Gürbüz, C., Türkelli, N., Sandvol, E., Seber, D. & Barazangi, M., 2003. The crustal structure of the East Anatolian Plateau from receiver functions, *Geophys. Res. Lett.*, **30**, 8044, doi: 10.1029/2003GL018192.

### Supporting Information

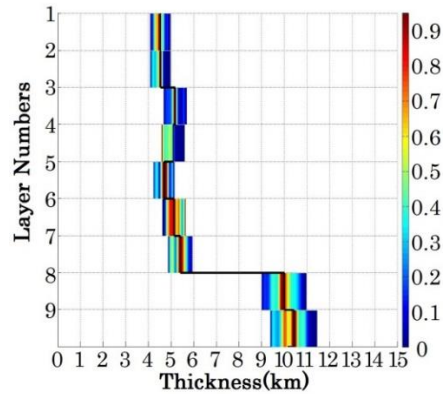


Figure S2.1 Represents thickness PPD computed from joint modeling of PRF, SRF and SW via MOOS for station S02, located in Oman. Thickness PPDs are not immediately interpretable in terms of depth. Y-axis represents layer numbers and does not signify anything about depths or thicknesses. Individual PPD block indicates thickness uncertainty on X-axis, and, associated layer number on Y-axis. Width of colored portion represents search bounds for thickness of  $\pm 10\%$  of best-fit thickness model (solid black line); hotter (yellow and red) colors indicate a higher probability that the true thickness will be found at that value. Narrow and single peak PPD values for almost all layers point toward fairly strong constraints imposed by our data functionals, though broad peak PPD values of 6<sup>th</sup> and 9<sup>th</sup> layers indicate that adding more data functionals can still be beneficial.

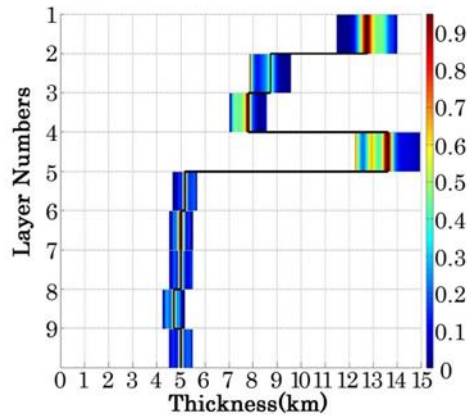


Figure S2.2 Shows thickness PPD for station KIV. All colors and symbols are same as in Figure S1. We use starting model from Sandvol et al. (1998) for finding best-fit thickness model (solid black line). There are greater uncertainties in top layers as compared to deeper layers, and, peak PPD value is almost absent for 2<sup>nd</sup> layer.

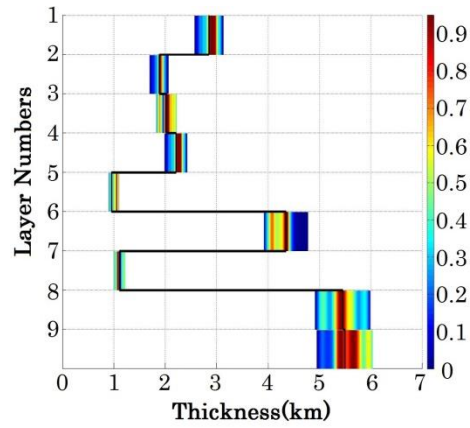


Figure S2.3 Shows thickness PPD for station ATD. All symbols and colors are same as in Figure S1. Initial model from Sandvol et al. (1998) was consulted for finding best-fit thickness model (solid black line). Except top two layers, there are higher uncertainties in thicknesses for all layers, indicating a high level of non-uniqueness.

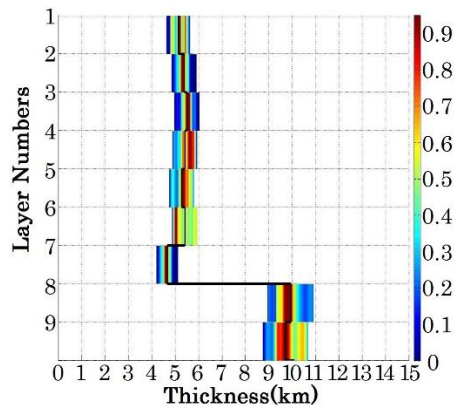


Figure S2.4 Represents thickness PPD obtained from joint analysis for station KYPR, located in Eastern Turkey. All symbols and colours are same as in Fig. S1. Thickness values are poorly constrained for 1st, 4th, 5th, 6th and 9th layers, as indicated by multiple/broad peaks in PPDs.

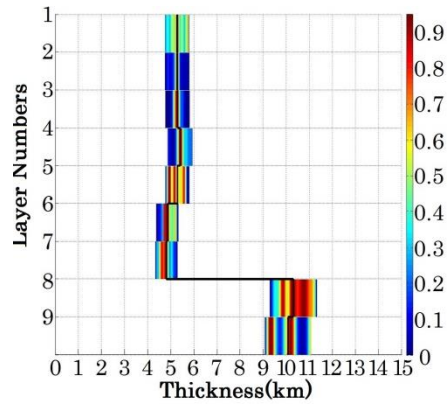


Figure S2.5 Represents thickness PPD for station DYBR located in Eastern Turkey. All symbols and colors are same as in Figure S1. Top four layers show fairly narrow PPD values, which indicate that the non-uniqueness of thickness model is fairly small. Thicknesses for 5<sup>th</sup>, 8<sup>th</sup> and 9<sup>th</sup> layers are less well-constrained, because multiple and/or broad peaks appear for these layers.

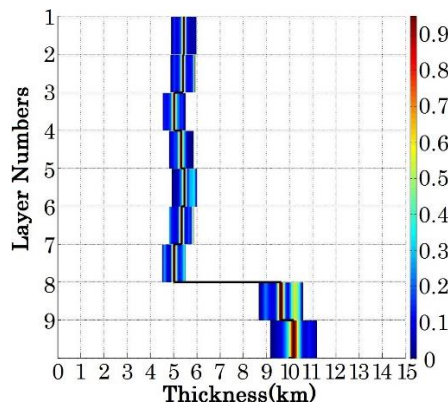


Figure 2.6 Thickness PPD for station AGIN situated in Eastern Turkey. All symbols and colours are same as in Fig. S1. PPDs for this station indicate that thickness model is subject to strong constraints imposed by PRF, SRF and SW.

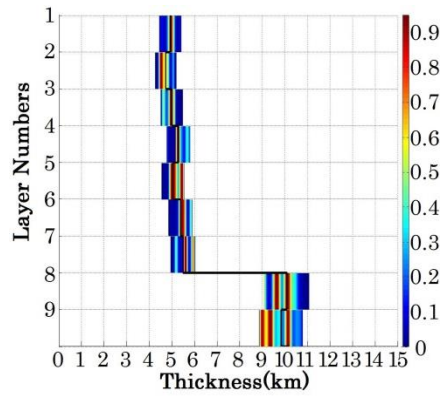


Figure S.2.7. Represents thickness PPD for station BTLS located in Eastern Turkey. All symbols and colors are same as in Figure S1. PPD values are constrained enough for almost all layers, except deepest layers where multiple peak values indicate towards non-uniqueness of the thickness model.

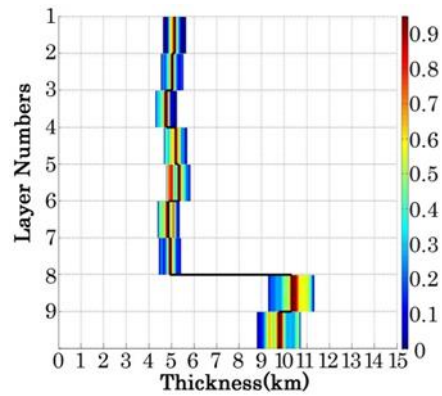


Figure S.2.8. Shows thickness PPD for station CSS located in Cyprus. All symbols and colors are same as in Figure S1. PPD values indicate that 7<sup>th</sup> and top three layers have well constrained thickness values i.e. higher amount of uniqueness, while other layers either show multiple and/or broad peaks i.e. lower uniqueness.

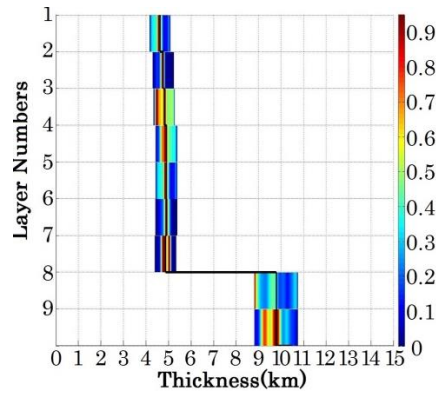


Figure S.2.9. This figure shows thickness PPD values for station S04 located in Oman. All symbols and colors are same as in Figure S1. PPD values indicate that data functionals appear to put enough constraints on most of the layers, except 3<sup>rd</sup>, 8<sup>th</sup> and 9<sup>th</sup> layers where our joint modelling scheme either found broad peak values or no value of thickness PPDs modeling scheme either found broad peak values or no value of thickness PPDs.

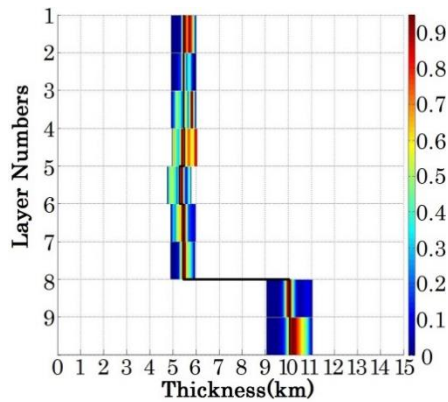


Figure S.2.10. Represents thickness PPD for station D2 located in Iran. All symbols and colors are same as in Figure S1. Broad and/or multiple peaks in almost all layers indicate towards higher degree of non-uniqueness in our best-fit thickness model.

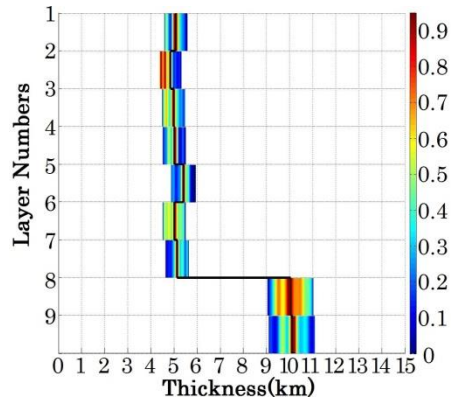


Figure S.2.11. Thickness PPD for station RAYN, located in Saudi Arabia. All symbols and colors are same as in Figure S1. Most of layers show well constrained values of thickness, except for 2<sup>nd</sup> and 8<sup>th</sup> layers where broad peak PPD values indicate that non-uniqueness of the model is fairly high for these layers.

## CHAPTER THREE

Lithospheric structure of the Texas-Gulf of Mexico passive margin from surface wave dispersion and migrated Ps receiver functions

This chapter published as: Agrawal, M., J. Pulliam, M. K. Sen, and H. Gurrola (2015), Lithospheric structure of the Texas-Gulf of Mexico passive margin from surface wave dispersion and migrated Ps receiver functions, *Geochem. Geophys. Geosyst.* 16, doi:10.1002/2015GC005803.

### *Abstract*

The seismic velocity structure beneath Texas Gulf Coastal Plain (GCP) is imaged by migrating Ps receiver functions with a seismic velocity model found by fitting surface wave dispersion. We use seismic data from a linear array of 22 broadband stations, spaced 16-20 km apart. A Common Conversion Point (CCP) stacking technique is applied to earthquake data to improve the S/N ratios of receiver functions.

Using an incorrect velocity model for depth migration of a stacked CCP image may produce an inaccurate image of the subsurface. To find sufficiently accurate P- and S-velocity models, we first apply a nonlinear modeling technique to fit Rayleigh wave group velocity dispersion via Very Fast Simulated Annealing.  $V_s$  ranges from 1.5 km/s in shallow layers of the GCP in to 4.5 km/s beneath the Llano uplift and just outboard of the Balcones Fault Zone (BFZ). The BFZ is characterized by slow velocities that persist to nearly 100 km depth.

In the stacked image, the largest-amplitude positive-polarity event ranges from the surface, at the Llano uplift, to a maximum depth of ~ 16 km beneath Matagorda Island. We attribute this event to the sediment-basement contact, which is expected

to produce a large impedance contrast. Another large-amplitude and positive-polarity event at ~35 km depth, which likely marks the Moho, disappears outboard of the Luling Fault Zone. The disappearance of the Moho beneath the GCP may be due to serpentinization of the upper mantle, which would reduce the impedance contrast between the lower crust and upper mantle dramatically.

## Introduction

The Gulf of Mexico (GOM) is a relatively small oceanic basin that formed as a result of rifting between the continental blocks of North America and Yucatan in the Middle to Late Jurassic (165 Ma) [e.g., *Menard, 1967; Bird et al., 2005; Stern et al., 2011; Mickus et al., 2009; Pindell and Dewey, 1982; Marton and Buffler, 1994; Molina-Garza et al., 1992; Burke, 1988; Pindell, 1994; Ross and Scotese, 1988; among others*]. The extent to which the continental crust was stretched and thinned prior to breakup is currently unknown [*Dickinson, 2009; Dunbar and Sawyer, 1987; Merle, 2011*]. After the breakup, seafloor spreading formed volcanic crust in at least part of the central Gulf of Mexico [*Menzies et al., 2002; Mickus et al., 2009; Hall and Najmuddin, 1994*]. However, in the early Cretaceous (140 Ma), opening between North America and Yucatan stopped [*Pindell, 2009; Bird et al., 2005*]. Since then, subsidence and sedimentation have largely shaped the Gulf margin [*Keller and Hatcher, 1999; Harry and Londono, 2004; Dickinson, 2009*]. Several hypotheses have been proposed to explain the region's lithospheric evolution, including rifting, continental collision, delamination, magmatic under-plating, and deformation [*Mosher et al., 2008; White and McKenzie, 1989; Mutter et al., 1984; Menzies et al., 2002; Mickus et al., 2009; Evanzia et al., 2014; Walker, 1992; Huerta and Harry, 2012; Ainsworth et al., 2014; etc*]. To assess the viability of these processes, better knowledge of lithospheric structure is needed which, in turn, requires additional data. Although Earthscope's Transportable Array (TA) has acquired broadband, three-component seismic data on scale-lengths that were unprecedented in this region, its 70 km station spacing is not optimal for producing images of crustal or lithospheric structure. In particular, the TA's resolution will not

allow us to address many key geoscientific issues for the Gulf of Mexico's passive margin, whose crust we expect to be thinner than much of the rest of North America.

A linear, 330-km-long temporary deployment of broadband seismic stations was conducted recently across the Texas Gulf Coastal Plain, from Matagorda Island, a barrier island in the Gulf of Mexico, onto the Llano uplift of Central Texas (Fig. 3.1). This array offers the potential to construct a relatively high-resolution, 2D image of the crust and upper mantle, using teleseismic P-to-S (Ps) converted waves and Rayleigh wave group velocity dispersion curves, along a transect from relatively undisturbed Proterozoic crust across a large portion of the passive margin to the Gulf of Mexico. The location and configuration of the array were chosen to span the shortest distance through a number of geological provinces, including the Gulf Coastal Plain (GCP), Balcones Fault Zone (BFZ), Luling Fault Zone, Llano Uplift (LU), and Stuart City Reef Trend (Fig. 3.1). Hence, this short aperture array allows for dense station spacing with relatively few instruments. The array's ~16 km station spacing produces an approximately fourfold increase in data sampling density with respect to the TA, with corresponding improvements in signal-to-noise ratio and/or spatial resolution. The resulting stacked, migrated Ps image thus offers an opportunity to address unresolved issues concerning the origin and evolution of this continent-ocean transition.

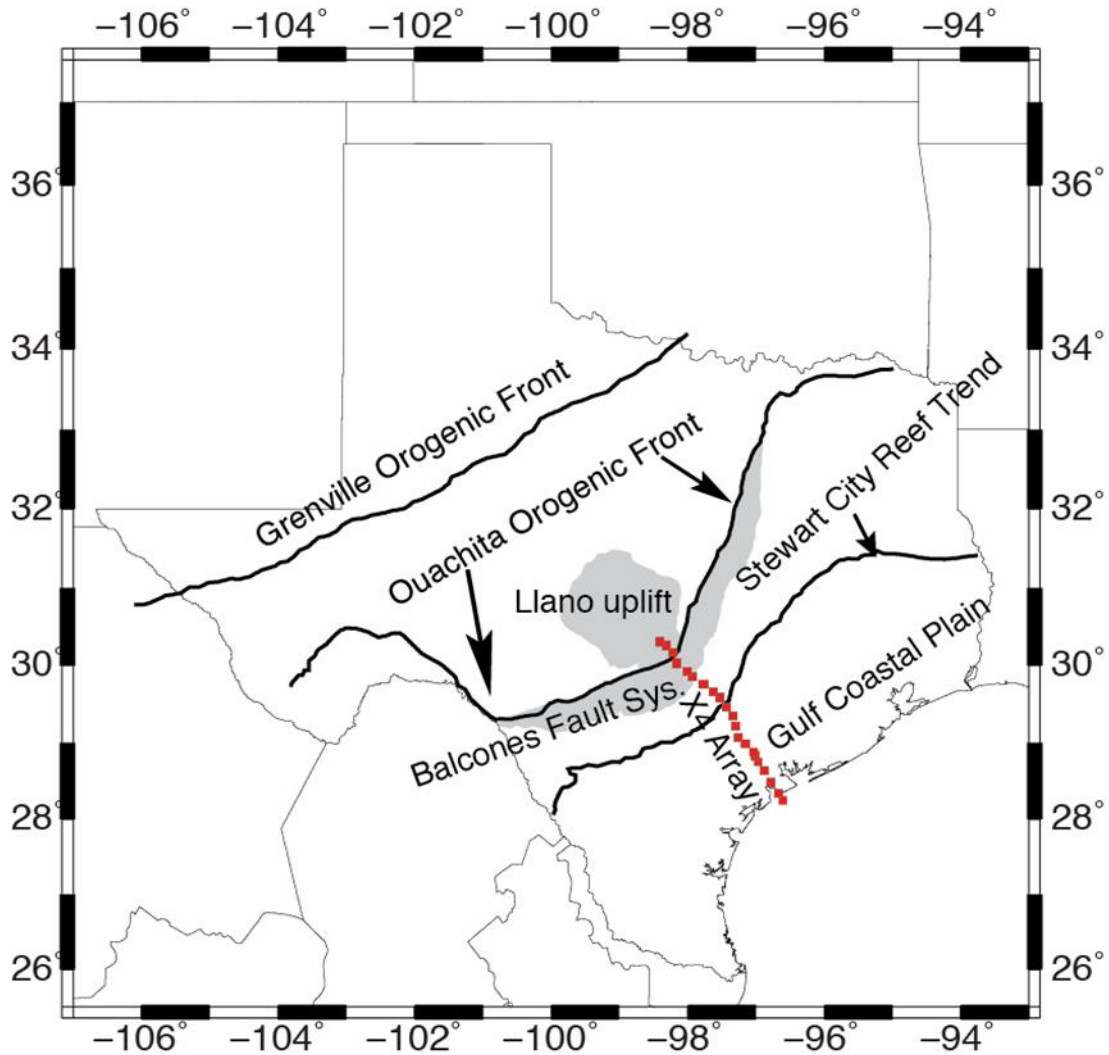


Figure 3.1 Map of tectonic features responsible for the formation of the Texas Gulf Coastal Plain and Central Texas. The location of the X4 Array is marked by red squares.

Since the pioneering work of *Langston [1979]*, seismologists have used “receiver functions” to identify impedance contrasts in the Earth’s crust and upper mantle. The method uses teleseismic earthquake data to estimate the response beneath seismic stations to depths of several tens or hundreds of kilometers. Common Conversion Point (CCP) stacking techniques average many closely-spaced receiver functions to improve signal-to-noise ratios and to depth migrate the images [*Zhu, 2000; Dueker and Sheehan, 1997; Li et al., 2000; Owens et al., 2000*]. Using an incorrect velocity model for time-to-depth

migration of a stacked CCP image will produce an inaccurate image of the subsurface, especially in the presence of substantial lateral velocity variations; yet reliable velocity models are not always available. One common approach to estimating velocities is to perform travel time tomography, using teleseismic earthquakes (because they are usually plentiful at distances greater than 1000 km) augmented by regional earthquakes, if they are available. However, in areas with few regional or local events, such as the Texas Gulf Coast, travel time tomography relies heavily on teleseismic events. Rays from teleseismic events arrive at seismic stations with steep angles of incidence and sub-parallel trajectories that generally do not intersect in the 0-100-km depth range. Teleseismic tomography with station spacing greater than 15 km, therefore, produces relatively poor constraints on the Earth's crust and uppermost mantle, which is the portion of the model for which accuracy is most critical to receiver function imaging. In regions with extremely low velocities, such as the Gulf Coast, teleseismic raypaths are particularly steep through the crust. This shortcoming is often more severe for shear wave tomography because picking S wave arrivals is more difficult than picking the first-arriving P wave, so datasets used for S-wave tomography tend to be smaller, and to represent sparser coverage, than those used for P-wave tomography. Both P- and S-velocity models are needed to migrate images produced with P-to-S or S-to-P converted waves.

Surface wave modeling, which is most sensitive to shallow shear wave velocities of the crust and upper mantle, offers an alternative strategy for finding sufficiently accurate velocity models for receiver function migration. In our study, we apply a nonlinear optimization technique to fit 1D models beneath each station to Rayleigh wave

group velocity dispersion curves via Very Fast Simulated Annealing (VFSA), a global optimization method [Sen & Stoffa, 1995; Gangopadhyay et al., 2007; Agrawal et al., 2014]. We use ambient noise cross-correlation to compute Rayleigh wave group velocity dispersion curves [Bensen et al., 2007]. We then interpolate between 1D models to form a smooth, 2D S-velocity model, construct a corresponding P-velocity model using assumed  $V_p/V_s$  ratios, and migrate the receiver functions using the new models. Surface waves and receiver functions offer complementary constraints on crustal parameters [Ammon et al., 2005]. Ps receiver functions are primarily sensitive to shear wave velocity contrasts in layered structures while dispersion curves are sensitive to volumetric shear wave velocities. By applying this sequential imaging technique to teleseismic and ambient noise data from 22 stations, we construct a subsurface structural image of the transect. The image provides an opportunity to evaluate hypotheses concerning the evolution of the Texas Gulf Coast's lithosphere.

### *Geological Background*

The Texas Gulf Coast underwent a series of tectonic processes leading to rifting and continental breakup. It has experienced at least two separate cycles of rifting and orogeny; once during the formation and breakup of Laurentia, and again during the formation and separation of Pangea [Thomas, 1991]. Laurentia left behind its main craton, which was exposed in the Llano uplift of central Texas approximately 1.4 Ga [Thomas, 1991]. At 1.1 Ga, the crust was partially deformed during the Grenville orogeny, caused by a partial subduction of Laurentia and the formation of Rodinia [Thomas, 2005]. Rodinia remained fairly stable and unchanged until rifting began at approximately 530 Ma, leading to the continent's breakup and the formation of the

Iapetus Ocean [Thomas, 1991]. The Ouachita orogenic belt was formed around 300 Ma when Gondwana and Laurentia collided, forming Pangaea [Thomas, 1991; Bird et al., 2005; Stern et al., 2011]. The formation of Pangaea was a soft collision (compared to the Alleghenian orogeny, for example) in which micro-continents and island arcs in the Iapetus Ocean were accreted to the supercontinent.

The present-day ocean-continent transition developed during the opening of the Gulf of Mexico, when Pangea began to break up along the western edge of the modern Gulf of Mexico. This led to the separation of North America from South America and the Yucatan Block [Stern et al., 2011; Mickus et al., 2009; Bird et al., 2005; Marton and Buffler, 1994; Pindell, 1994; Ross and Scotese, 1988; Molina-Garza et al., 1992; Burke, 1988; Dunbar and Sawyer, 1987; Pindell and Dewey, 1982; Menard, 1967; etc]. The Balcones Igneous Province (BIP) lies at the boundary between Texas's Mesoproterozoic craton and the buried transitional crust of the Jurassic-age passive margin and nearly coincides with the Ouachita fold belt. The nature of this buried transitional crust is difficult to determine due to the presence of thick sediments beneath the Gulf Coastal Plain (GCP) [Dickinson, 2009; Harry and Londono, 2004]. There is no consensus with respect to the processes that initiated rifting and formed the GCP. Some workers attribute the GCP to an active rifting process, the result of upwelling asthenosphere associated with a thermal anomaly in the mantle [e.g., Mickus et al., 2009; Menzies et al., 2002] while others argue in favor of a passive rifting process, driven by far field stresses and distinguished mainly by ductile deformation and ongoing faulting of the crust and mantle [Marton and Buffler, 1993]. Continental margins that result from passive rifting are characterized by relatively little magma, high stretching factors, rotated fault blocks and

low seismic velocities beneath ocean-continent transition interpreted as serpentinized mantle [Mjelde *et al.*, 2007]. In contrast, margins that result from active rifting form by quick and voluminous emplacement of magma, including sills, dikes and magmatic underplating [Mutter *et al.*, 1984]. Cross-sections based on seismic profiles acquired by COCORP (Consortium for Continental Reflection Profiling) suggest that the Luling uplift is located at the updip limit of the Cenozoic sediment wedge, which is cut by steeply dipping normal faults that sole into the top of the uplift [Culotta *et al.*, 1992].

*Sequential Modeling of Rayleigh Wave Group Velocity Dispersion and Ps Receiver Functions*

This study employs a sequential modeling process in which each type of data is treated separately, in alternating steps, so that results of one modeling step are used as inputs to the next step. Geophysical data rarely allow a structural model to be determined uniquely; more than one solution usually explains the data equally well. Non-uniqueness becomes apparent when values of parameters of an earth's physical model can be changed without degrading the fit to observed data. Numerous workers have shown that the number of models that fit the data to acceptable levels can be decreased and the variability between those models can be diminished by using complementary datasets [e.g., Julia *et al.*, 2000,2003 & 2005; Agrawal *et al.*, 2014; Ammon *et al.*, 2005, 2006; Cakir and Erduran, 2004; Chang *et al.*, 2004; Dugda & Nyblade, 2006; Herrmann *et al.*, 2001; Lawrence and Wiens, 2004; Ozalaybey *et al.*, 1997; Pasyanos, 2005; Tkalcic *et al.*, 2006]. The results shown here use Ps receiver functions and Rayleigh wave group velocity dispersion curves to obtain a 2D model beneath the X4 array that is consistent with both datasets.

## *Method*

A schematic representation of the methodology employed here is shown in Figure 3.2.

*Step 1: Compute Rayleigh wave group velocity dispersion curves using an ambient noise processing technique.* Green's functions of subsurface structure between two seismic stations (or locations) can be extracted with a simple field-to-field correlation computed over a sufficiently long time period [Weaver and Lobkis, 2001, 2004; Derode et al., 2003; Snieder, 2004; Wapenaar, 2004; Shapiro et al., 2004; Larose et al., 2005; Bensen et al., 2007]. We employ a three-phase ambient noise data processing procedure for computing the Green's response between pairs of stations. In the first phase, single-day waveforms are prepared for each seismic station by removing instrument response, de-meaning, de-trending and bandpass filtering the seismogram, followed by temporal normalization and spectral whitening. Temporal normalization is performed by applying "running-absolute-mean normalization" to remove the effects of earthquakes, instrument irregularities and non-stationary noise sources [Bensen et al., 2007; Shapiro et al., 2004]. Processing steps for the computation of dispersion curves are shown schematically in Figure 3.3.

In the second phase, daily time series are cross-correlated and stacked. For each station pair, frequency domain cross-correlation is carried out on daily seismograms. These correlated seismograms are then returned to the time domain and stacked to improve SNR ratio and to obtain an estimate of the station pair's Green's function. An example of correlation and reverse correlation (for day 245 of year 2012) of station GC06 with GC14 is shown in Figures 3.4a and 3.4b, respectively; their corresponding one-year stack (year 2012) is shown in Figure 3.4c.

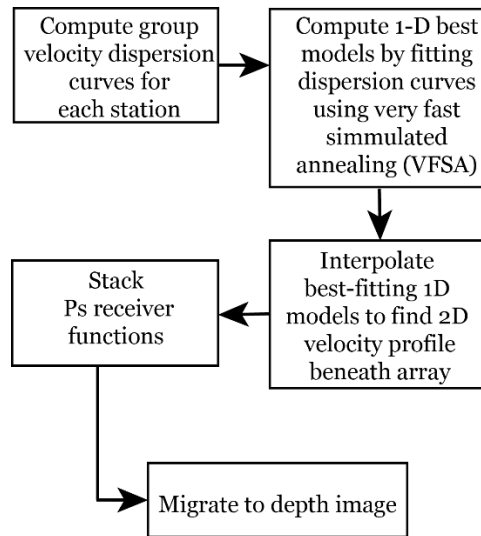


Figure 3.2 Block diagram of the methodology employed to construct 2D seismic image beneath the X4 array from Rayleigh wave group velocity dispersion curves and CCP stacking of Ps receiver functions.

In phase three, Rayleigh wave group velocity dispersion curves are computed from Green’s functions using frequency-time analysis (FTAN) [e.g. *Dziewonski et al., 1969; Herrin and Goforth, 1977; Russell et al., 1988; Ritzwoller and Levshin, 1998; Levshin and Ritzwoller, 2001*]. Figure 3.4d shows a Rayleigh wave group velocity dispersion curve from FTAN analysis of the Green’s function shown in Figure 3.4c. We use these dispersion curves to infer shear wave velocity as a function of depth, thereby producing constraints on lithospheric structure.

The 16-18-km station spacing of the X4 array was designed to admit receiver functions studies, body wave tomography, and shear wave splitting measurements. For long-period surface waves, the wavefield is oversampled. We therefore employ a moving bin technique to include a maximum number of seismic stations in our group velocity calculations. The upper limit of lateral resolution is determined by the number of seismic stations involved in a bin. For 10-40 s periods, a bin size of five stations provides

consistent group velocities, while a bin of seven stations is appropriate to find group velocities of longer period waves.

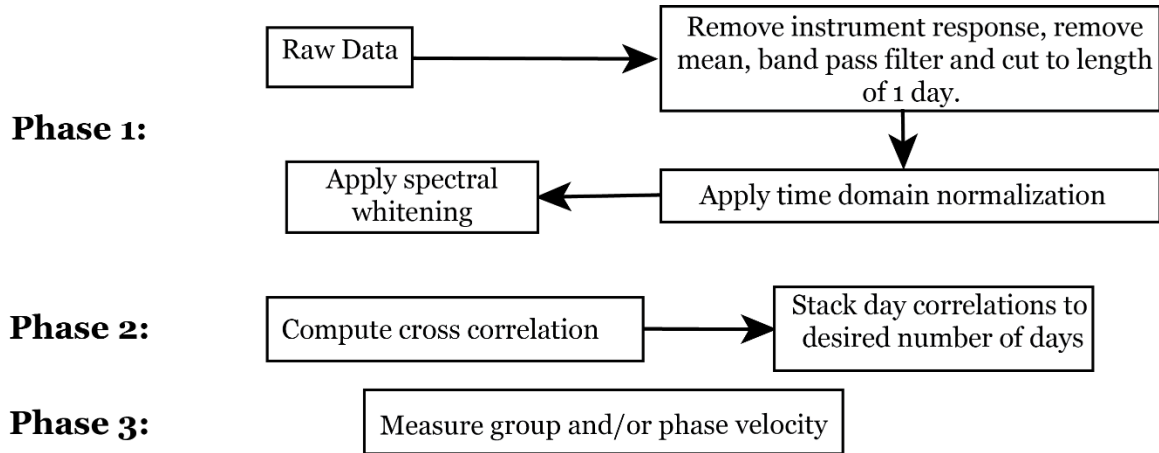


Figure 3.3 Schematic diagram of processing steps for the computation of dispersion curves via ambient noise cross correlation.

*Step 2: Obtain 1D models by fitting Rayleigh wave group velocity dispersion curves.*

Identifying a model that best explains observed data, usually by finding the minimum value of an objective function, is a primary aim of seismic modeling. Geophysical inverse problems are nonlinear in nature but, for reasons of tractability and simplicity, are often solved using linear methods. Linear methods, such as least-squares methods, are best suited to finding models that are quite similar to the starting model, rather than the single, best-fitting model within a given model space. Therefore, in this analysis we employ a stochastic, nonlinear, global optimization technique known as Very Fast Simulated Annealing (VFSA), which is weakly dependent on the choice of initial model [Sen and Stoffa, 1995; Gangopadhyay et al., 2007; Agrawal et al., 2014; Zhao et al., 1996; Ingber, 1989]. VFSA is a variant of Simulated Annealing (SA) that is aimed at making computations more efficient [Ingber, 1989; Sen and Stoffa, 1995]. Simulated Annealing

is a quantitative algorithm that mimics the process of crystal annealing of a physical system [Kirkpatrick *et al.*, 1983]. During an annealing process in, for example, metallurgy, a solid at higher temperature ( $T_0$ ) is allowed to cool slowly from a disorderly state (or elevated energy) to an orderly (“ground”) state of minimum energy. “Simulated annealing” draws an analogy between this physical concept of annealing and numerical optimization problems in seismology. The energy of a system is associated with the misfit ( $E(\mathbf{m}_0)$ ) between synthetic and observed data. The higher energy state of a physical system is identified with a starting model ( $\mathbf{m}_0$ ) of seismic modeling process. The temperature ( $\mathbf{T}$ ) is a free parameter that controls the search process [Sen and Stoffa, 1995]. The ground state of a physical system is equivalent to the global minimum of its associated objective function. At each iteration ( $\mathbf{k}$ ) the temperature ( $\mathbf{T}(\mathbf{k})$ ) is lowered an amount specified by a cooling schedule ( $\mathbf{T}(\mathbf{k}) = T_0/k$ ) and an updated model is randomly drawn from a specified distribution within predefined limits of model parameter space. The original, and still popular, version of SA draws new models from a uniform distribution [Metropolis *et al.*, 1953]; VFSA differs in that it draws new models from a Cauchy distribution [Ingber, 1989]. A “fitness” value associated with each updated model ( $\mathbf{m}_k$ ) is computed using the following objective function:

$$\text{Error (E)} = 1 - \frac{2 \sum |d_{obs}^i - d_{syn}^i|^\alpha}{\sum |d_{obs}^i + d_{syn}^i|^\alpha + \sum |d_{obs}^i - d_{syn}^i|^\alpha}, \quad (1)$$

where  $\mathbf{d}^{obs}$  and  $\mathbf{d}^{syn}$  denote observed and synthetic data, respectively, and the parameter  $\alpha$  ( $=0.5$  in the modeling presented below) represents the norm of the objective function. If the error at trial  $k$ ,  $E(\mathbf{m}_k)$ , is less than or equal to the error associated with the previous

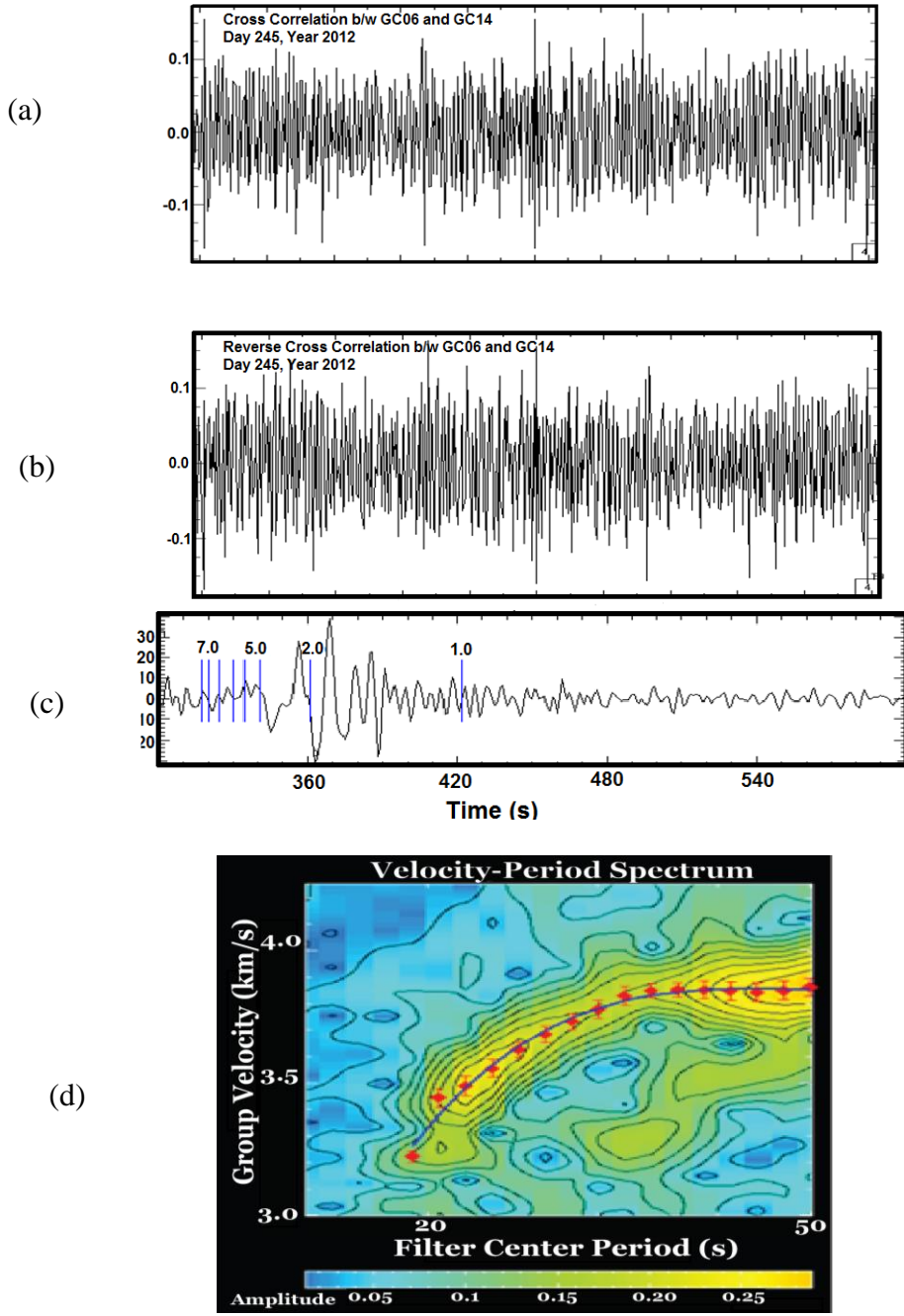


Figure 3.4. Example of the ambient noise cross correlation technique for finding dispersion curves via (a) correlation and (b) reverse correlation for day 245 of year 2012 of station GC06 with GC14. The corresponding one-year stack (2012) is shown in (c). Figure (d) shows the resulting Rayleigh wave group velocity dispersion curve produced via FTAN analysis (see text for further details).

model,  $E(m_{k-1})$ , the new model ( $m_k$ ) is accepted and replaces the previous model ( $m_{k-1}$ ). However, if this condition is not satisfied then the new model may still be accepted, according to a probability function specified by the user. The probabilistic acceptance of VFSA allows the algorithm to escape local minima and continue to search the model space for a global minimum of the objective function. This process is repeated, with the temperature slowly cooling according to a predefined schedule, until the procedure converges. Further details of SA and VFSA can be found in *Sen and Stoffa [1995]*. We run the modeling scheme described above to produce a set of 1D shear wave velocity model for the subsurface beneath each seismic station of the X4 array (Fig. 3.5).

To construct search bounds for the upper crust between stations GC04 (Bloomington, Texas) to GC12 (Gonzalez, TX) we consulted a crustal refraction survey conducted on the Texas Gulf Coast by Cram [1962] (blue dashed lines in Fig. 3.5). For the lower crust and upper mantle, starting velocities were based on ak135 [Kennett *et al.* 1995]. For other stations, we use ak135 for all layers (black dashed lines in Fig. 3.5). During each modeling run, we allowed shear velocities to vary within  $\pm 15\%$  of initial values. The thickness of each layer was permitted to vary from 2-8 km. We set the initial temperature at  $10^{-4}$  dimensionless units and allowed it to cool to  $10^{-14}$  units for each VFSA run. We discovered, after a set of trials, that the misfit error changed very little after  $\sim 1500$  iterations, so we set the maximum number of iterations to 2000 to provide an adequate margin for error. The resulting best-fit models are shown, as examples for some stations, by the solid red line in Figure 3.5.

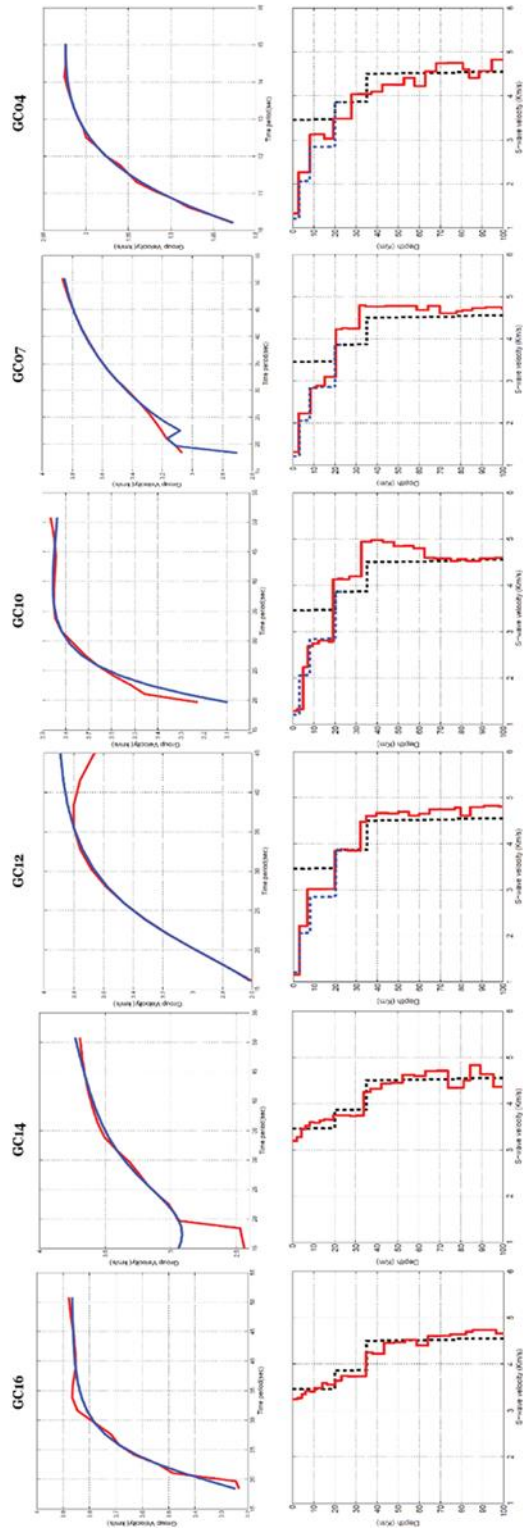


Figure 3.5. Fitting of dispersion curves for stations GC04, GC07, GC10, GC12, GC14 and GC16 via Very Fast Simulated Annealing. Solid red lines show the best-fitting models; broken black and blue lines represent ak135 and the model obtained from a refraction survey in South Texas (Cram, 1962).

*Step 3: Compute 1D depth profiles of P-velocities.* For this purpose we use Poisson's ratios equal to that of a Poisson solid (1.76) and shear wave velocities found by modeling dispersion curves, as discussed above. These 1D models are interpolated to create the 2D shear and compressional wave velocity models beneath the X4 transect (Fig. 3.6). These 2D models were used to migrate the CCP-stacked Ps receiver function image from the time domain to the depth domain.

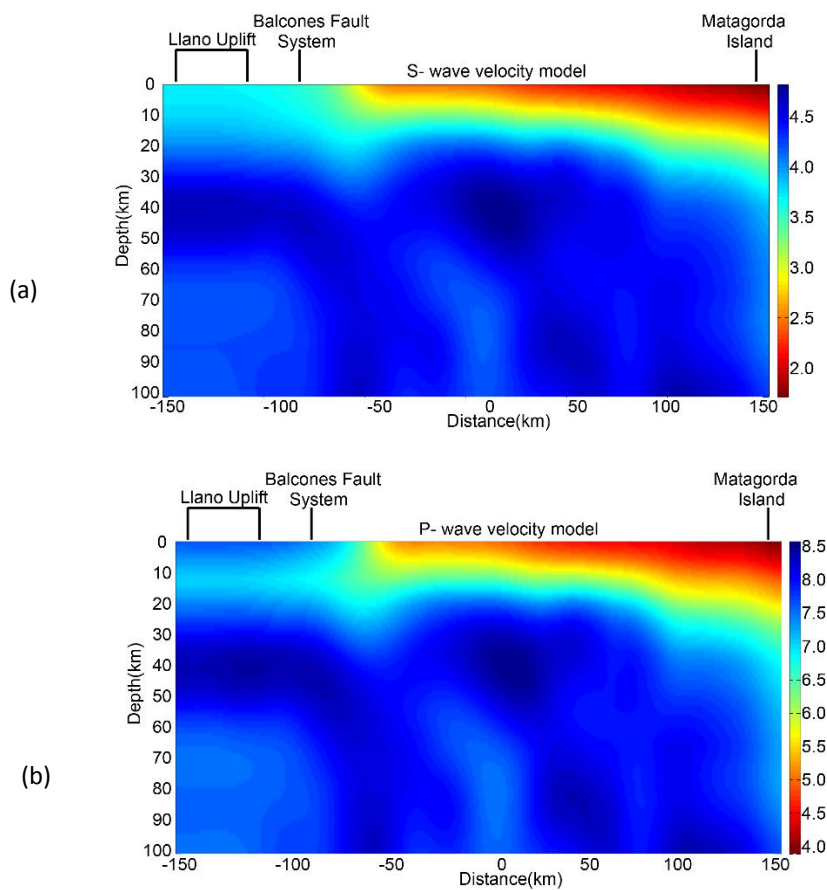


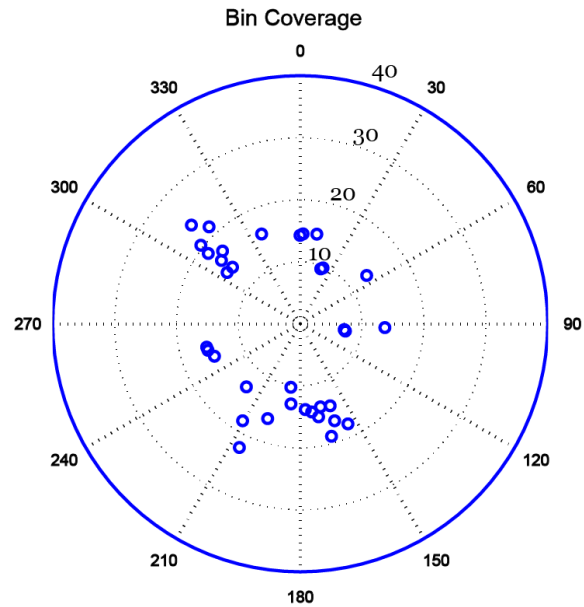
Figure 3.6 (a) 2D  $V_s$  model interpolated from 1D  $V_s$  models computed for each station. 1D models were found by fitting Rayleigh wave group velocity dispersion curves using VFSA;  $V_s$  ranges from 1.5 km/s to 4.5 km/s. (b)  $V_p$  values were computed using the  $V_p/V_s$  ratio of a Poisson solid (i.e., 1.76); the  $V_p$  range is 4.0-8.5 km/s.

*Step 4: Compute Ps receiver functions using a multichannel deconvolution algorithm.*

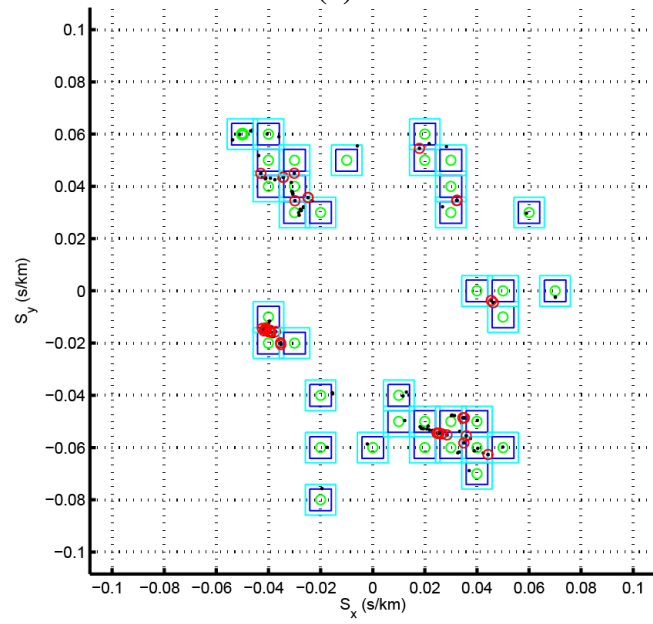
Receiver functions were computed using a Matlab<sup>TM</sup> program developed by S. Hansen and K. Dueker [*Hansen et al., 2013*]. This algorithm is based upon a new technique that explicitly includes pure-mode scattering of direct arrival components, i.e. P-P scattering on the P-component and S-S scattering on the SV-component. This methodology computes a three-component receiver function (P-SV-SH) for each event bin by utilizing the quasi minimum-phase nature of the direct component receiver function [*Hansen and Dueker, 2009; Baig et al., 2005; Bostock, 2004; Mercier et al., 2006*].

The multichannel deconvolution algorithm uses a three-step process: First, the amplitude of the source time function for each event is estimated by a rough-smooth spectral separation algorithm [*Hansen and Dueker, 2009*]. Second, the amplitude spectrum of the three-component receiver function (P-SV-SH) is computed through inversion using a least-squares method. Finally, the minimum phase of the direct component trace is used to reconstruct the spectral phase of the receiver function. In an effort to avoid site-specific effects and pure mode scattering, the algorithm estimates a single source time function from all station's recordings of a particular event, instead of using individual trace components [*e.g., Ligorria and Ammon, 1999; Helffrich, 2006*].

The events were binned by back-azimuth and ray parameter, producing a variable number of event bins for each station. For example, the polar plot shown in Figure 3.7(a) represents event bins used in receiver function processing for station GC01, located on Matagorda Island. The radial distance is the estimated angle of incidence of the direct arrival, computed using average Vp and Vs velocities at the surface as rotation velocities. Then, all events are binned in slowness space using square, non-overlapping bins with a



(a)



(b)

Figure 3.7 (a) Polar plots of event bins used in receiver function processing for station GC01. Blue circles denote event bins. The radial distance is the estimated angle of incidence of the direct arrival at the surface. (b) Slowness bins with a width of 0.01 sec/km used for station GC01.

width of 0.01 sec/km (see Fig. 3.7(b) for station GC01). One Ps receiver function is estimated per bin per station, resulting in a total of 5060 receiver functions from 230 earthquakes recorded by 22 stations in the array.

Three-component traces for all station-event pairs are windowed and tapered to extract time series starting 30 s before and ending 110 s after the arrival of the direct P phase. A 4-pole band pass filter with corner frequencies at 0.08 Hz and 1.0 Hz is then applied to improve the signal-to-noise ratio. Next, converted Ps phases are isolated from direct P phases after rotating seismograms from Z-N-E coordinates to P-SV-SH coordinates by finding the incident angle that minimizes S energy associated with P arrivals (Vinnik, 1977). Each earthquake and corresponding spectrogram is inspected visually after aligning the P phase branch for each event trace. Recordings with clear P and SV components are manually ranked based on signal-to-noise ratio and a correlation window is picked.

Receiver functions extracted from three-component waveforms, using the methodology described above, are shown in Figure 3.8 for two bedrock stations, GC18 and GC19, which are located on the Llano uplift. In principle, the physical parameters and lithospheric structure sampled by each receiver function trace should be similar, since the stations are only 18 km apart. In practice, however, converted phases are weak, due to the influence of a dipping basement-sediment interface and complex geology, and are sometimes obscured by noise. An event with positive polarity corresponds to a velocity increase with depth and a negative polarity event corresponds to a velocity decrease with depth. One of the major problems in receiver functions produced by

stacking traces using a relatively small number of events is to distinguish individual peaks that may be

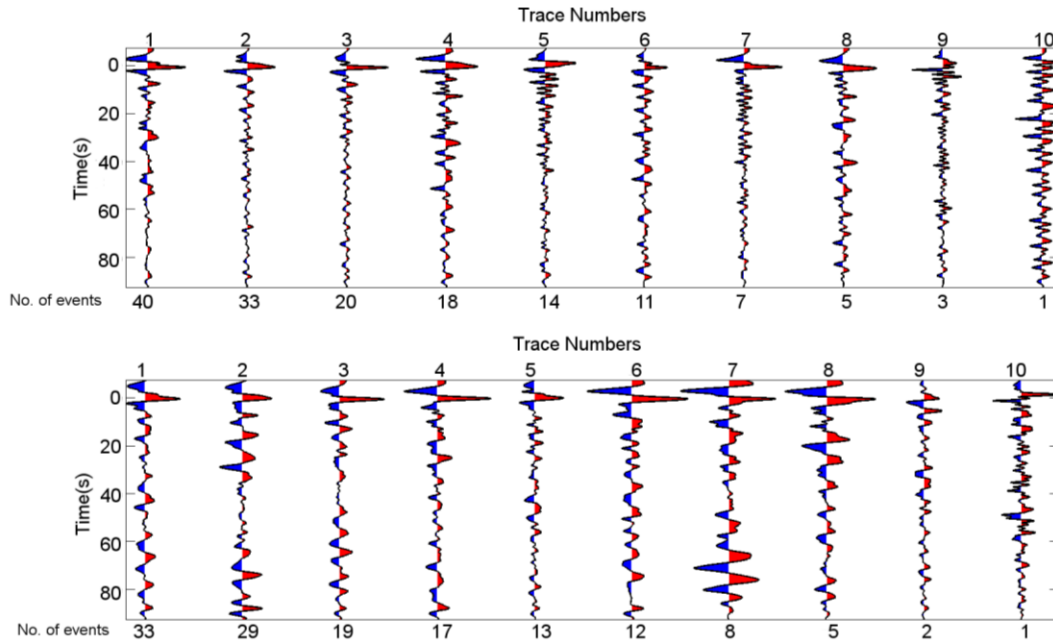


Figure 3.8. Ps receiver functions computed for stations GC18 (top panel) and GC19 (bottom panel) via the multichannel deconvolution method (see text for details) and bandpass filtered from 0.08 to 1.0 Hz. The numbers of traces used in receiver functions computation from multiple events are listed at the bottom of each receiver function trace. For example, for GC18 and GC19, the first traces were computed using 40 events and 33 events per cluster, respectively.

obscured by neighboring larger peaks or their side lobes. Most of these must be considered noise.

We stack Ps receiver functions using a Common Conversion Point (CCP) stacking method to increase signal-to-noise ratios [Dueker and Sheehan, 1997; Eagar et al., 2010, 2011]. The technique we use is a back-projection method in which receiver functions are raytraced through 2D P- and S-wave velocity models (generated in step 3) to place their amplitudes at appropriate positions laterally and in depth. Subsurface image points (or bin size) are spaced 10 km apart laterally for Ps receiver functions. Error

bounds of the CCP stack are found via bootstrapping; data are restacked 20 times, using a random number generator to resample events recorded by each station. The CCP stack errors in Figure 11(b) are based on two standard deviations about the mean, which corresponds to the 95% confidence level.

### *Data*

The 330-km-long X4 seismic array consisted of 22 three-component broadband seismometers deployed from July 2010 until March 2013. The configuration of the array was chosen to cross four distinct geological provinces: the Texas Gulf Coastal Plain, the Balcones Fault System, the Ouachita front, and the Llano uplift (Fig. 3.1). Instrumentation at each site included a Reftek 130 digitizer/recorder and a Guralp 3T, Guralp 3ESP, or Nanometrics Trillium Compact seismometer powered by a marine deep-cycle battery charged by a solar panel. Data were recorded continuously at 40 samples/s and stations were visited every three months, on average, to recover data.

Ps receiver function data: Antelope<sup>TM</sup> and PASSCAL software were used to reformat, inspect, and preprocess the Ps receiver function data. Events with magnitudes greater than 5.5 at epicentral distances of  $30^{\circ}$ - $95^{\circ}$  and all backazimuths (Fig. 3.10) were used to compute receiver functions.

Ambient noise data: Green's function were extracted from seismic ambient noise recorded for year 2012, during which relatively few high magnitude earthquakes ( $M \geq 7.0$ ) occurred. We downloaded and computed cross-correlations for continuous vertical component records from each day of year 2012.

## *Results and Discussion*

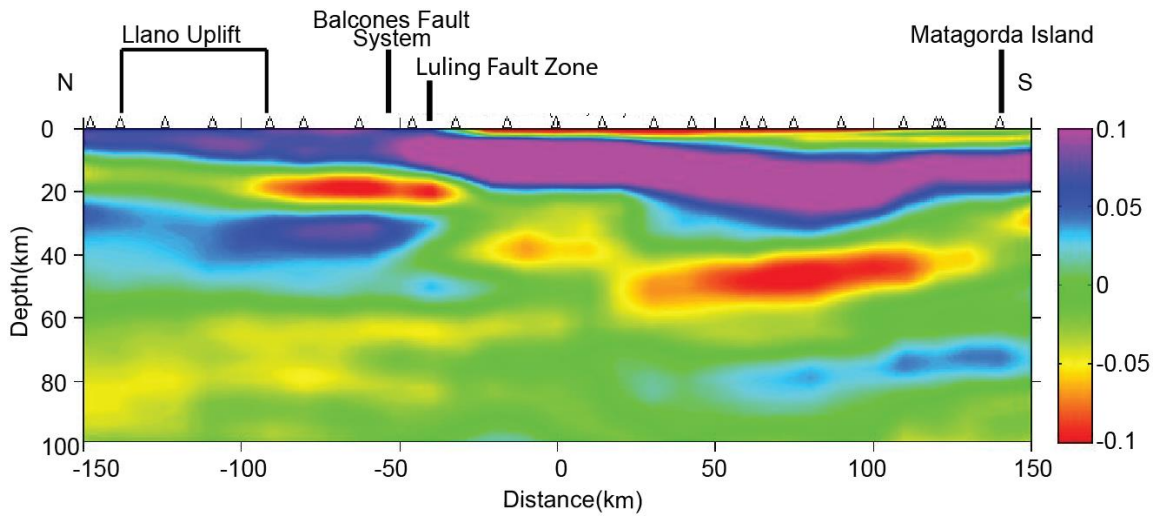
### *Shear wave velocity model from dispersion curves*

The 2D shear wave velocity ( $V_s$ ) model is a result of interpolation between 1D  $V_s$  profiles that were constrained by fitting Rayleigh wave group velocity dispersion curves using VFSA (Fig. 3.6). The depth to which surface waves are sensitive increases with period; e.g., 8-s period Rayleigh group waves are sensitive to a depth of about 10 km whereas the 50-s period waves are sensitive to depths of about 80 km. We attempt to match our dispersion curves between 10-s and 50-s periods. A discontinuity that we interpret to be the Moho appears in the northwestern portion of the array (beneath the Llano uplift at 30-40 km depth) but disappears to the southeast, outboard of the Balcones Fault Zone beneath the Coastal Plain. The Moho's disappearance may be due to widespread serpentinization in the region (discussed in more detail below), which would be expected to decrease the impedance contrast across the Moho dramatically. The low velocity region in the shallow subsurface between -50 km to 150 km distance in Fig. 3.6 marks the deep sediment package that characterizes the Coastal Plain, from the Balcones Fault Zone to Matagorda Island. Lastly, a high velocity anomaly appears at Moho depth (30-40 km) between the 0 and -50 km distance range but low velocities prevail the Balcones zone itself (in the 25-100 km distance range), which may imply that the Balcones Fault Zone serves as a conduit from the mantle to the surface.

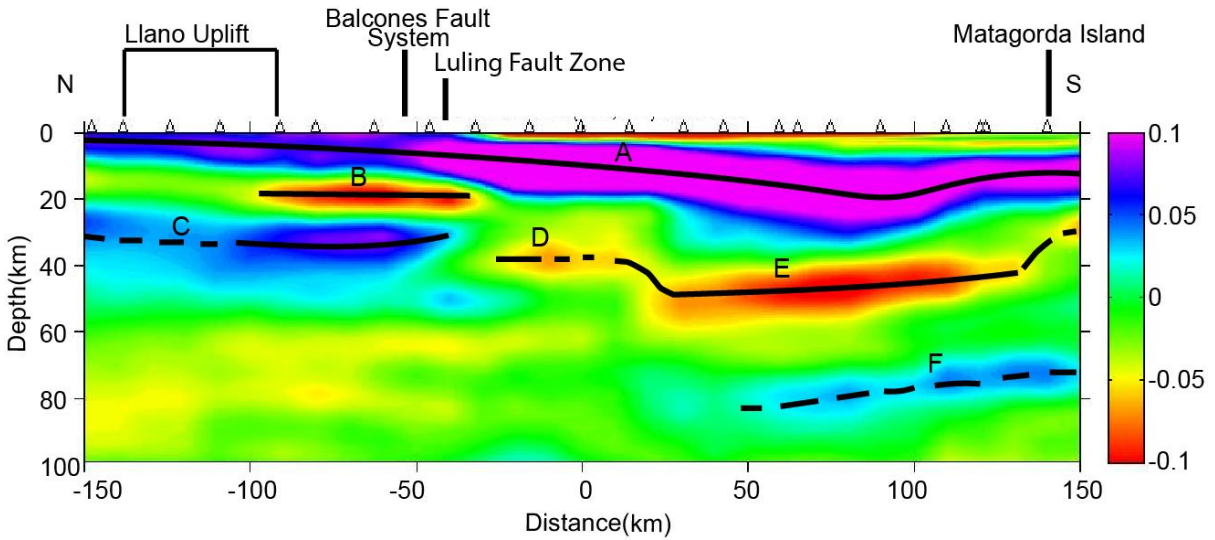
*Sediment-basement contact and Moho*

Figure 3.9a shows the CCP-stacked and migrated Ps receiver function image for the X4 transect. The image does not include direct “P” arrivals because we isolate converted Ps waves from direct P waves by rotating Z-R-T components to P-SV-SH components. SV and SH components contain mainly energy converted from P- to S-waves. Events

(a)



(b)



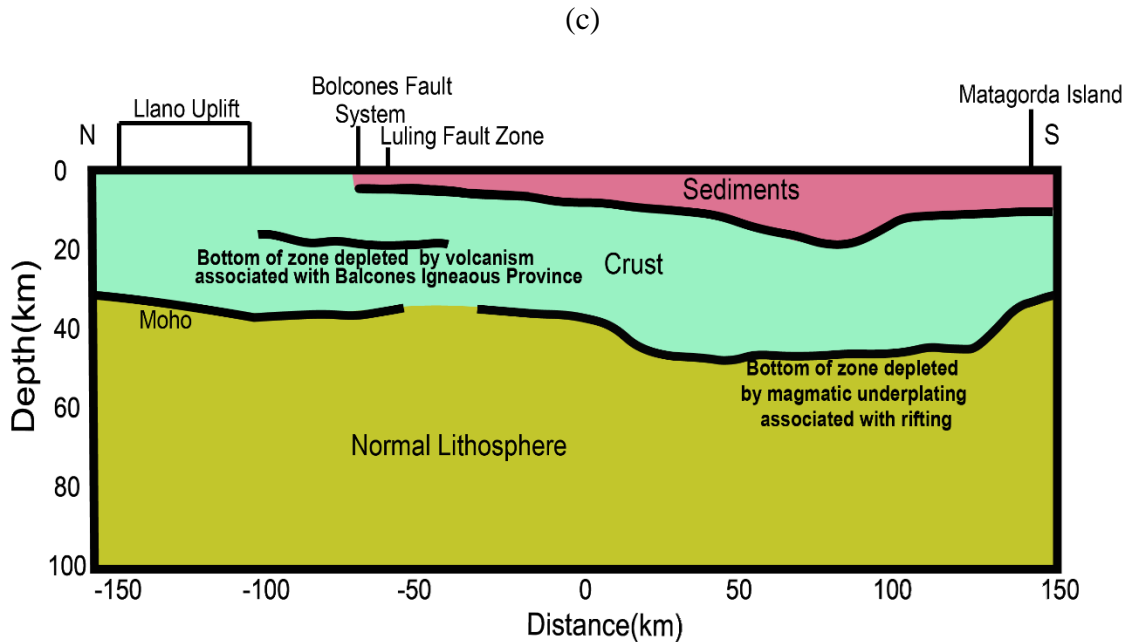


Figure 3.9 (a) Ps receiver function CCP-stacked image. Positive amplitudes indicate increases in velocity with depth while negative amplitudes indicate decreases in velocity with depth. Figure (b) shows the same image as in (a) but with major discontinuities marked by broken lines (indicated weaker amplitudes) or solid black lines (indicating strong arrivals). A large positive polarity event “A” represents sediment-basement contact. Negative polarity event “B” may be due to volcanism that formed Balcones Igneous Province (BIP), or, may posit a through-going Balcones fault. Label “C” can be interpreted as Moho while labels “D” and “E” could be attributed to melt extraction during rifting (see text for further detail). Positive event labeled by “F” may be a free-surface reverberation of event “A” (see text). (c) A cartoon cross-section of the X4 profile across the Texas Gulf Coastal Plain that shows important features interpreted in this study.

with positive polarities (blue/purple) mark depths at which seismic velocity increases abruptly with increasing depth; events with negative polarities (red/yellow) mark velocity decreases abruptly as a function of depth.

A large positive polarity event appears at the surface on the Llano uplift and dips to a maximum depth of ~16 km under the Gulf Coastal Plain (labeled “A” in Figure 3.9b). This event is likely due to the large impedance contrast at the sediment-basement contact between crystalline facies in the crust, which have a shear wave velocity of

approximately 3.5 km/s, and the less consolidated sediments above, which have shear wave velocities as low as 1-2 km/s, as suggested by shear wave velocity model from surface wave modeling (Fig. 6a). Galloway [2009] estimated a maximum depth to basement of ~14 km on the Texas Gulf Coast, which is consistent with our estimate of ~16 km. Previous geophysical studies, including modeling of potential field data [Mickus *et al.*, 2009; Mickus and Keller, 1992; Harry *et al.*, 2004], seismic refraction profiles [Cram, 1962; Hales *et al.*, 1970; Dorman *et al.*, 1972; Duncan and Gurrola, 2009], and seismic reflection data [Culotta *et al.*, 1992], have estimated depths to basement of 10-15 km beneath the GCP. Keller and Shurbet (1975) modeled Rayleigh wave group velocity dispersion curves and suggested the presence of Mesozoic and Cenozoic sedimentary layers (P velocity  $\leq 5.2$  km/sec) above Paleozoic sedimentary rocks at the base of the GCP. A study by Ainsworth *et al.* [2014] using Sp receiver functions could not image this sediment-basement contact due to the longer wavelengths, with respect to Ps receiver functions, that is intrinsic to Sp converted waves from earthquakes.

Beneath the northwest half of the array, the CCP-stacked image shows a positive-polarity event (labeled “C” in Fig. 3.9b) at ~33 km depth in the extreme north of the array beneath Llano uplift that dips slightly upward to ~28 km beneath the Balcones and Luling fault zones. We interpret this event to be the Moho, although it is shallower than the Moho depth of ~38-40 km found previously by Mickus *et al.* [2009] from integrated geophysical modeling and by Ainsworth *et al.* [2014] from Sp receiver functions. Recently, seismic crustal models within the USGS crustal structure database were used to create a 3D crystalline crustal model of North American continent. This model suggests an average crustal thickness of ~34 km in the coastal plain adjacent to the Gulf of Mexico

[Tesauro *et al.*, 2014]. Their study also suggests an average crustal P-wave velocity range of 5.95 – 7.30 km/s in this region, which is in good agreement with the P-wave velocity estimates of 6.1 – 7.5 km/s we found by fitting Rayleigh wave group velocity dispersion curves (see Figure 3.6b).

The Moho event weakens beneath the Llano uplift, which may be due to less dense ray coverage, as indicated in Figure 3.11a. The Moho is missing outboard of the Luling fault zone; its disappearance is the subject of a detailed discussion in section 6.2.

A negative-polarity event (labeled “E” in Fig. 3.9b) extends across the coastal plain starting at a depth of ~50 km (at a distance of ~25 km) and dips upward to ~40 km depth near the coast. Another negative-polarity event (“D”) is adjacent to event “E”, albeit at a shallower depth (~38 km). Although “D” is a much weaker event than “E”, the simplest explanation is that they are due to the same mechanism (discussed below). The region in which “D” appears has lower data density than the rest of the image (Fig. 3.11a) so the difference in amplitude could be related to differences in data density and resulting signal-to-noise ratio. Rather than invoke two processes, we will treat “D” and “E” as a single event in our further discussion.

This negative-polarity represents a negative impedance contrast, which usually implies a decrease in seismic velocity with increasing depth. Previous studies found a similar low velocity zone in the upper mantle beneath this transect from seismic Sp receiver functions [Ainsworth *et al.*, 2014], *potential field modeling* [Mickus *et al.*, 2009], and *seismic tomography* [Evanzia *et al.*, 2014] and Duncan and Gurrola [2009] discovered a similar discontinuity in their reinterpretation of the Hales *et al.* [1970] refraction profile, which transects the Texas Gulf Coast further to the east. Event “E”

could be attributed to melt extraction during rifting, which would deplete the layer below of iron, thus raising its velocity. Note that the observation and modeling of a high-amplitude magnetic anomaly in the lower crust by Mickus et al. [2009] led to their suggestion that the GCP is a volcanic rifted margin and that the magnetic anomaly is due to a large mafic igneous complex that was produced during rifting. The interpretation of events “D” and “E”, which extend for more than 100 km, as the upper boundary of an iron-depleted layer supports the case for voluminous magmatism and active rifting. However, the magnetic anomaly modeled by Mickus et al. [2009] reaches its maximum at the coast (Matagorda Island, in Fig. 3.9) and extends roughly 50 km inland, so it is not clear why the lower boundary of the depleted layer would fail to conform to those limits. Also, Speckien [2012] demonstrated that the anomaly could be explained equally well by a coincidence of two anomalies: one that is associated with Gulf of Mexico rifting and another that is associated with the Ouachita deformational event. Speckien [2012] concludes that the magnetic anomaly associated with rifting represents a much smaller volume of magma than would be expected to result from active rifting.

A weak blue feature (labeled “F” in Fig. 3.9b) appears in the CCP-stacked image at a depth of ~75 km, dipping to the northwest. This feature may be a free-surface reverberation (“multiple”) of event “A” because it has the same dip and same polarity (as would be expected of PPs multiples; PSs multiple would have the opposite polarity) and because the Sp CCP-stacked image of *Ainsworth et al.* [2014] does not show this feature. (Sp images do not include free surface multiples because Sp phases are precursors to the S phase.) A multiple is a processing artifact, so if “F” were indeed a multiple it would not be the result of a conversion of waves by a discontinuity at 75 km depth and would not

require a geological interpretation. However, another explanation for this feature is possible. As a result of a joint analysis of seismic, gravity, and mineral physics data, *Mooney and Kaban [2010] and Kaban et al. [2014]* report the presence of a compositional anomaly in the uppermost mantle that they hypothesize may be caused by a high-density eclogite body. These authors note that such a body might also explain the subsidence of the Gulf Coast. Further, *Nettles and Dziewonski [2008]* report a positive S-velocity anomaly in the uppermost mantle that coincides with this high-density, compositional anomaly. The polarity of event “F” is consistent with the top of a high-density, fast S-wave anomaly.

Event “B”, located at ~20 km depth, has negative polarity but appears to be distinct from the other negative-polarity events, “D” and “E”, because it is located above the Moho and at the boundary between cratonic and transitional crust. This event may be associated with volcanism that formed the Balcones Igneous Province (BIP). The BIP extends ~400 km along the juncture between Mesoproterozoic cratonic lithosphere and Jurassic transitional lithosphere (the Gulf Coastal Plain) from near Austin, north of the X4 profile, to southwest of San Antonio. Recent dating identifies two distinct periods of activity in the Balcones Igneous Province: mafic volcanism between 81.5 and 84.1 Ma and felsic volcanism between 76.2 and 78.8 Ma [*Griffin et al., 2010*]. The compositional differences and age distribution of the volcanic centers makes it unlikely that the BIP was produced by a mantle plume and the briefness of its activity suggests it was cut off from a fertile mantle that might have replenished its budgets of alkali and volatile elements [*Griffin et al., 2010*]. Event “B” would then represent a low-velocity zone produced by the depletion of volatile elements through volcanism.

Another possible explanation for event “B” posits a through-going Balcones fault (perhaps as a result of crustal embrittlement, as discussed further below). Rather than magma ascending and depleting a zone to produce a velocity contrast, however, surface water might have been funneled to the mantle below, resulting in widespread serpentinization of mantle peridotites. Event “B” would then represent a low-velocity zone that is associated with water filtration through the crust. Unfortunately, neither of these scenarios can be confirmed from the seismic results described here.

A cartoon cross-section showing the structure of the GCP’s crust and uppermost mantle inferred from Ps receiver function CCP stacking is shown in Figure 3.9c.

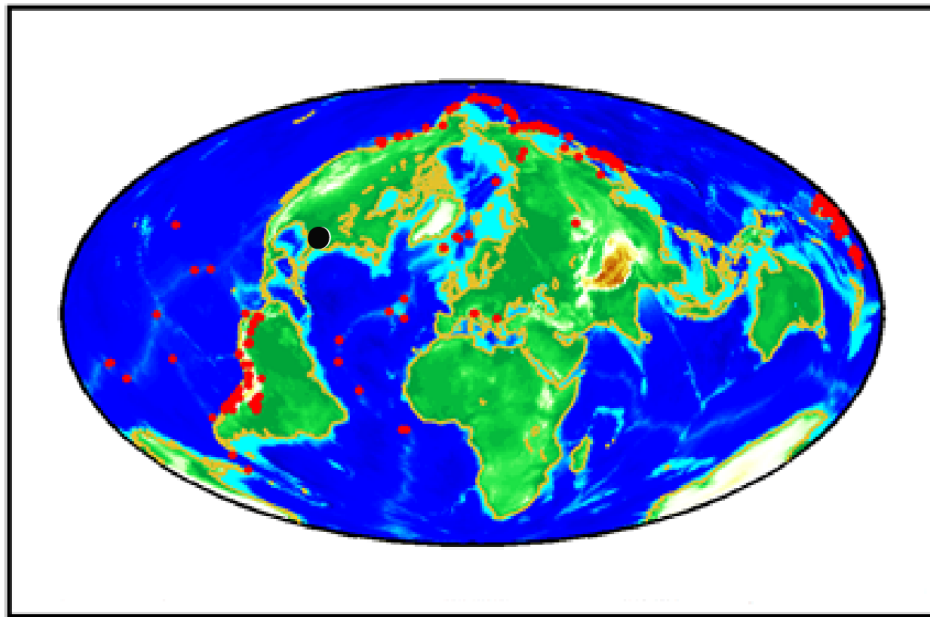


Figure 3.10 Earthquake locations used in Ps receiver functions (~230 events from July 2010 – May 2013). A black dot marks the location of the X4 array.

*Moho missing due to serpentinized upper mantle*

Event “C” in Figure 3.9a is the most likely candidate to represent the Moho, due to its depth (28-33 km) and positive polarity, which indicates that seismic velocity

increases downward across the event. Yet event “C” ends abruptly just outboard of the Balcones Fault System and no other feature in the CCP-stacked image could reasonably be interpreted to be the Moho. Also, a corresponding “Moho feature” appears in the northwestern part of the shear wave velocity model (between 30 km to 40 km) found from ambient noise but is absent in the southeastern portion of the transect (Fig. 3.6). This suggests that a mechanism acted to decrease dramatically the impedance contrast that usually marks the Moho. One such mechanism could be serpentinization of the upper mantle.

Serpentinization is a process in which a (usually ultramafic) rock undergoes hydration and metamorphic transformation. The most common example is the serpentinization of peridotite (or dunite) into serpentinite, its metamorphic equivalent. Serpentinization alters the physical and chemical properties of the affected rock. Among its important effects are a dramatic reduction in density of the affected rocks and a significant, although less dramatic, reduction in seismic P and S velocities. Together these effects serve to produce a strong reduction in impedance (the product of density and seismic velocity), which could erase the contrast between a silicate lower crust and a serpentinized mantle.

Serpentinization is consistent with other observations, as well. Complete serpentinization of a peridotite results in a water uptake of 13-15% by weight and a volume increase of ~40% [*e.g. Schroeder et al., 2002; Shervais et al., 2005*]. These changes also influence the rheology of the rock and thus play an important role in the formation of detachment faults and strain localization along serpentinized fault planes [*Escartin et al., 1997a, b*]. A COCORP reflection seismic transect across the Texas Gulf

Coastal Plain, near our passive seismic profile, identified possible detachment faults [Culotta et al., 1992].

An important condition for serpentinization of mantle rocks is embrittlement of the entire crust [Gussinyé and Reston, 2001; O' Reilly et al., 1996] which, during the progressive crustal thinning that occurs before rifting, produces a network of faults and fractures that serve as conduits for potentially large volumes of water to pass through the crust. Gussinyé and Reston [2001] performed numerical modeling experiments to provide insight into the thermal evolution of lithosphere during extension at different strain rates. They identified a range of stretching factors for which the entire crust moves into the brittle regime and compared their modeling results to observations made of the non-volcanic continental-ocean transition zone of West Iberia. In other studies, several continental-ocean transition regions have been identified as sites of serpentinized peridotites (e.g., Southwest Greenland margin [Gussinyé et al., 2014]; West Iberia margin [Gussinyé et al., 2014; Boillet and Winterer, 1988; Pickup et al., 1996; Whitemarsh and Sawyer, 1996]; Labrador Sea [Chian et al., 1995]; Porcupine Basin in southwest Ireland [Reston et al., 2001]; north and northeast Atlantic margins [Lundin and Doře, 2011], which continued landward under the thinned continental crust [Boillet et al., 1989; Chian et al., 1999]).

At magma-poor margins, partial serpentinization of the upper mantle may have been a result of severe extension which, in turn, may cause the embrittlement of both the upper and lower crust, allowing growth faults (such as the Wilcox, Corsair Fault Zones, Balcones and Luling Fault Zones) to cut through the entire crust and provide pathways for water to reach the mantle. This results in an increase in volume and decrease in

density of mantle rock which could cause regional uplift of the overlying crust. Uplift around the rim of the northern Gulf of Mexico has been noted by numerous authors but, to our knowledge, its mechanism has not been explained adequately. Widespread serpentinization, and consequent density reduction, of the upper mantle could explain the observed uplift.

Next, teleseismic travel time tomography of the Texas region shows unusually slow shear wave velocities (-5-10% with respect to the average model ak135) in the upper mantle beneath the Texas Gulf Coastal Plain [Evanzia *et al.*, 2014]. While tomography that relies on distant (i.e., teleseismic) earthquakes typically has poor depth control in the crust and uppermost mantle and, in this case, slow velocities of coastal sediments could be mapped downward, efforts to project as a large a portion of the travel time anomaly as possible into the sedimentary basin and crust confirms that the result of slow shear wave velocities in the uppermost mantle to be a robust feature. Widespread serpentinization of the upper mantle would explain anomalies of this magnitude.

Lastly, the reactions that lead to serpentinization are highly exothermic. Previous studies have shown that the Gulf Coastal Plain is distinguished by high heat flow [Blackwell *et al.*, 2010; Ewing and Caran, 1982]. Borehole geothermal data integrated with COCORP seismic profiles has determined that two areas of high heat flow, at least, occur along growth faults that parallel the coast [Culotta *et al.*, 1992; Nagihara *et al.*, 2012; Blackwell and Richards, 2004]. The Corsair and Wilcox fault zones are located 60-80 km and 80-100 km NW from the southernmost station (GC01) of our profile. Fluids circulating within these systems of growth faults may be produce the high levels of

heat flow at the surface, particularly if the faults themselves penetrate to the mantle, as a result of crustal embrittlement.

### *Ray Coverage*

Ray coverage is quite good along most of the X4 transect. However, distances between -90 to 0 km are not as well-sampled as other portions of the array, with hit counts of less than 100, compared to hit counts of more than 150 elsewhere (Fig. 3.11a). Poor ray coverage in this interval can be attributed to instrument malfunctions following a widespread flood that occurred in 2010, at the outset of the deployment. All the instruments were ultimately repaired or replaced but those sites have shorter recording times than other sites. Ray coverage is highest in the distance range 50-100 km, as shown by the dark blue color in Figure 3.11a.

### *Bootstrapping Errors*

Figure 3.11b presents bootstrapping error estimates. These show relatively uniform, low errors for the majority of the image although, as expected, error values are higher in in the -50 to 0 km range, where ray coverage is sparser than elsewhere. Stacking errors range from ~0.005 to ~0.04, but most of the area has rather low stacking errors of <0.01. The maximum amplitude in the CCP image is 0.1, so error estimates constitute 5-30% of the phase amplitudes.

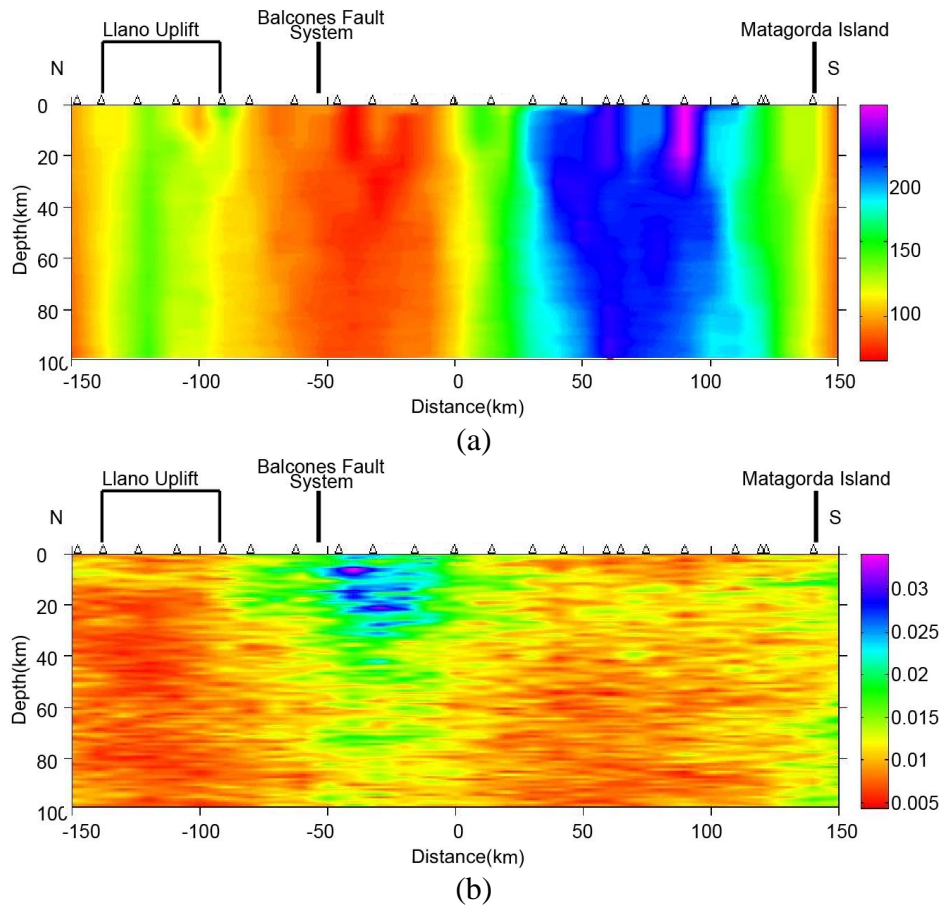


Figure 3.11 The (a) “hit count” and (b) stack error associated with the Ps receiver function CCP stack. The “hit count” represents ray coverage beneath the X4 array. Lower hit counts in the northern part of the profile is due to instrument malfunctions (resulting from flooding); stations in those locations did not record as many as earthquakes as other stations. Errors in the CCP stack were estimated by a bootstrapping method. In spite of the variations, Figure (b) indicates that errors associated with the CCP stack are fairly small across the array.

### *Conclusions*

Common conversion points (CCP) stacking of Ps receiver functions and modeling of Rayleigh wave group velocity of dispersion curves using Very Fast Simulating Annealing (VFSA) reveal significant discontinuities beneath the Texas Gulf Coastal Plain (Fig. 9b) and the equally significant absence of a discontinuity that can be identified as the Moho outboard of the Luling fault zone. We use ambient noise cross correlation

technique to calculate Rayleigh wave group velocity dispersion curves. Modeling of dispersion curves produces 2D shear and compressional wave velocity models for the 0-100 km depth range for use in migrating Ps receiver functions.

A large event with positive polarity, attributed to the sediment-basement contact, extends distinctly from the Balcones Fault Zone to Matagorda Island and reaches a maximum depth of ~16 km approximately 60 km from the coast. A second positive-polarity event appears at ~28-33 km depth from the Llano uplift to the Luling Fault zone but then disappears. The depth and polarity of this event suggest that it represents the Moho, so its disappearance requires an explanation. We propose widespread serpentinization of the upper mantle, possibly as a result of crustal embrittlement during pre-rift extension that produced through-going faults that serve as conduits for surface water to the uppermost mantle. Total crustal embrittlement is consistent with the existence of detachment faults that were discovered during a COCORP seismic reflection survey [Culotta *et al.*, 1992]. Serpentinization of mantle peridotites is consistent with other observations, including unusually slow shear wave velocities in the uppermost mantle [Evanzia *et al.*, 2014], high levels of heat flow, and widespread uplift around the northern rim of the Gulf of Mexico. Two negative-polarity events may indirectly support the case for the GCP being a volcanic margin.

#### *Acknowledgements*

We thank S. Hansen and K. Dueker for the use of their receiver function imaging software and S.P. Grand for the use of broadband instruments. High school science teachers David Boyd, Michael Arratia, and Craig Weart and students from Southwestern University, Deep Springs College, Texas Lutheran University, and Cornell College, as

well as Baylor and Texas Tech universities, contributed extensively to fieldwork and we gratefully acknowledge their efforts. We are also grateful to Randy Keller and to two anonymous reviewers for their constructive comments and criticism. This research was supported by funding from the National Science Foundation (EAR 0746321, EAR 0750711), the Norman Hackerman Advanced Research Program of the Texas Higher Education Coordinating Board (NHARP #003658-0034-2009), the Gulf Coast Association of Geological Societies, and the W.M. Keck Foundation.

## References

- Agrawal, M., J. Pulliam, M.K. Sen, U. Dutta, M. Pasyanos, and R. Mellors (2014), Crustal and uppermost mantle structure in the Middle East: Assessing constraints provided by jointly modeling Ps and Sp receiver functions and Rayleigh wave group velocity dispersion curves, in press, *Geophys. J. Int.*, February 2015.
- Ainsworth, R., J. Pulliam, H. Gurrola, and D. Evanzia (2014), Sp receiver function imaging of a passive margin: transect across Texas's Gulf Coastal Plain, *Earth Planet. Sci. Lett.*, 402, 138-147.
- Ammon, C. J., M. Kosarian, and R. B. Hermann (2006), Simultaneous Inversion of Receiver Functions, Multi-mode Dispersion, and Travel-time Tomography for Lithospheric Structure Beneath the Middle East and North Africa. *Defense Technical Information Center*.
- Ammon, C. J., M. Kosarian, R. B. Herrmann, M. E. Pasyanos, W. R. Walter, and W. Sevilla (2005), Simultaneous Inversion of Receiver Functions and Surface-Wave Dispersion Measurements for Lithospheric Structure Beneath Asia and North Africa, *Proceedings of the 27th Seismic Research Review: Ground-Based Nuclear Explosion Monitoring Technologies*, 3-12.
- Baig, A., M. Bostock, and J. P. Mercier (2005), Spectral reconstruction of teleseismic P Greens functions, *J. Geophys. Res. : Solid Earth (1978-2012)*, 110.
- Bensen, G., M. Ritzwoller, M. Barmin, A. Levshin, F. Lin, and M. Moschetti (2007), Processing seismic ambient noise data to obtain reliable broad-band surface wave dispersion measurements, *Geophys. J. Int.*, 169, 1239-1260.
- Bird, D. E., K. Burke, S. A. Hall, and J. F. Casey (2005), Gulf of Mexico tectonic history: Hotspot tracks, crustal boundaries, and early salt distribution, *Am. Assoc. Pet. Geol. Bull.*, 89, 311-328.
- Blackwell, D., and M. Richards (2004), Geothermal map of North America, *AAPG Map*, scale 1:6,500,000, Product Code 423.
- Blackwell, D., M. Richards, and Z. Frone (2010), Texas Geothermal Assessment for the I35 Corridor East for Texas State Energy Conservation Office Contract CM709, *Southern Methodist University*.
- Boillot, G., G. Feraud, M. Recq, and J. Girardeau (1989), "Undercrusting" by serpentinite beneath rifted margins: The examples of the west Galicia margin (Spain), *Nature*, 341, 523-525.
- Bostock, M. (2004), Greens functions, source signatures, and the normalization of teleseismic wave fields, *J. Geophys. Res.: Solid Earth (1978-2012)*, 109.

- Burke, K. (1988), Tectonic evolution of the Caribbean, *Annual Review of Earth Planet. Sci.*, 16, 201-230.
- Cakir, A., and M. Erduran (2004), Constraining crustal and uppermost mantle structure beneath station TBZ (Trabzon, Turkey) by receiver function and dispersion analyses, *Geophys. J. Int.*, 158, 955-971.
- Chang, S.-J., C. -E. Baag, and C. A. Langston (2004), Joint analysis of teleseismic receiver functions and surface wave dispersion using the genetic algorithm, *Bull. Seismol. Soc. Am.*, 94, 691-704.
- Chian, C., C. Keen, I. Reid, and K. Loudon (1995), Evolution of nonvolcanic rifted margins of the Labrador Sea, *Geology*, 23, 589-592.
- Chian, C., K. E. Loudon, T. A. Minshull, and R. B. Whitmarsh (1999), Deep structure of the ocean-continent transition in the southern Iberia Abyssal Plain from seismic refraction profiles: Ocean Drilling Program (Legs 149 and 173) transect, *J. Geophys. Res.*, 104, 7443-7462.
- Cram Jr, I. H. (1962), Crustal structure of Texas coastal plain region, *Am. Assoc. Pet. Geol. Bull.*, 46, 1721-1727.
- Culotta, R., T. Latham, M. Sydow, J. Oliver, L. Brown, and S. Kaufman (1992), Deep structure of the Texas Gulf passive margin and its Ouachita-Precambrian basement: Results of the COCORP San Marcos Arch Survey, *Am. Assoc. Pet. Geol. Bull.*, 76, 270-283.
- Derode, A., E. Larose, M. Tanter, J. De Rosny, A. Tourin, and M. Campillo (2003), Recovering the Green's function from field-field correlations in an open scattering medium (L), *J. Acoust. Soc. Am.*, 113, 2973-2976.
- Dickinson, W. R. (2009), The Gulf of Mexico and the southern margin of Laurentia, *Geology*, 37, 479-480.
- Dorman, J., J. L. Worzel, R. Leyden, T. N. Crook, and M. Hatzimmanuel (1972), Crustal section from seismic refraction measurements near Victoria, Texas, *Geophys.*, 37, 325-336.
- Dueker, K. G., and A. F. Sheehan (1997), Mantle discontinuity structure from midpoint stacks of converted P to S waves across the Yellowstone hotspot track, *J. Geophys. Res: Solid Earth*, 102, 8313-8327.
- Dunbar, J. A., and D. S. Sawyer (1987), Implications of continental crust extension for plate reconstruction: An example from the Gulf of Mexico, *Tectonics*, 6, 739-755.

Dugda, M. T., and A. A. Nyblade (2006), New constraints on crustal structure in eastern Afar from the analysis of receiver functions and surface wave dispersion in Djibouti, *Geol. Soc. London Spec.*, 259, 239-251.

Duncan, G., and H. Gurrola (2009), An updated interpretation of the Hales 1969 onshore–offshore refraction experiment: an investigation of the rifted margin of the Northern Gulf of Mexico and Gulf Coastal Plain, *In: Fall Meeting 2009. Am. Geo-phys. Union. Abstract #t53D-1620*.

Dziewonski, A., S. Bloch, and M. Landisman (1969), A technique for the analysis of transient seismic signals, *Bull. Seismol. Soc. Am.*, 59, 427-444.

Eagar, K. C., M. J. Fouch, and D. E. James (2010), Receiver function imaging of upper mantle complexity beneath the Pacific Northwest, United States, *Earth Planet. Sci. Lett.*, 297, 141--153.

Eagar, K. C., M. J. Fouch, D. E. James, and R. W. Carlson (2011), Crustal structure beneath the High Lava Plains of eastern Oregon and surrounding regions from receiver function analysis *J. Geophys. Res.: Solid Earth (1978--2012)*, 116.

Escartín, J., G. Hirth, and B. Evans (1997a), Nondilatant brittle deformation of serpentinites: Implications for Mohr-Coulomb theory and the strength of faults, *J. Geophys. Res.*, 102, 2897-2913.

Escartín, J., G. Hirth, and B. Evans (1997b), Effects of serpentinization on the lithospheric strength and the style of normal faulting at slow-spreading ridges, *Earth Planet. Sci. Lett.*, 151, 181-189.

Evanzia, E., J. Pulliam, R. Ainsworth, H. Gurrola, and K. Pratt (2014), Seismic Vp & Vs tomography of Texas & Oklahoma with a focus on the Gulf Coast margin, *Earth Planet. Sci. Lett.*, <http://dx.doi.org/10.1016/j.epsl.2013.12.027>.

Ewing, T.E., and S. C. Caran (1982), Late Cretaceous volcanism in South and Central Texas—stratigraphic, structural, and seismic models, *Gulf Coast Assoc. Geol. Soc. Trans.*32, 137-145.

Gangopadhyay, A., J. Pulliam, and M. K. Sen (2007), Waveform modelling of teleseismic S, Sp, SsPmP, and shear-coupled PL waves for crust-and upper-mantle velocity structure beneath Africa, *Geophys. J. Int.*, 170, 1210-1226.

Hales, A.L., J. B. Nations and C. E. Helsley (1970), Crustal structure study on the Gulf coast of Texas, *Am. Assoc. Pet. Geol. Bull.*, 54, 2040-3057.

Hall, S. A., and I. J. Najmuddin (1994), Constraints on the tectonic development of the eastern Gulf of Mexico provided by magnetic anomaly data, *J. Geophys. Res.*, 99, 7161-7175.

Hansen, S. M., K. G. Dueker, J. C. Stachnik, R. C. Aster, and K. E. Karlstrom (2013), A rootless rockies-Support and lithospheric structure of the Colorado Rocky Mountains inferred from CREST and TA seismic data, *Geochem. Geophys. Geosyst.*, *14*, 2670-2695.

Hansen, S., and K. Dueker (2009), P-and S-wave receiver function images of crustal imbrication beneath the Cheyenne Belt in southeast Wyoming, *Bull. Seismol. Soc. Am.*, *99*, 1953-1961.

Harry, D., and J. Londono (2004), Structure and evolution of the central Gulf of Mexico continental margin and coastal plain, southeast United States, *Geol. Soc. Am. Bull.*, *116*, 188-199.

Helfrich, G. (2006), Extended-time multitaper frequency domain cross-correlation receiver-function estimation, *Bull. Seismol. Soc. Am.*, *96*, 344-347.

Herrin, E., and T. Goforth (1977), Phase-matched filters: application to the study of Rayleigh waves, *Bull. Seismol. Soc. Am.*, *67*, 1259-1275.

Herrmann, R. B., C. J. Ammon, and J. Julia (2001), Application of joint receiver-function surface-wave dispersion for local structure in Eurasia, *techreport*.

Huerta A.D., and D. L. Harry (2012), Wilson cycles, tectonic inheritance, and rifting of the North American Gulf of Mexico continental margin, *Geosphere*, *8*, 374-385.

Gussinye, M.P., and T. J. Reston (2001), Rheological evolution during extension at nonvolcanic rifted margins: Onset of serpentinization and development of detachments leading to continental breakup, *J. Geophys. Res.*, *106*, 3961-3975.

Gussinye, M.P., T. J. Reston, and J. P. Morgan (2001), Serpentinization and magmatism during extension at non-volcanic margins: the effect of initial lithospheric structure, *Geol. Soc. London Spec. Publ.*, *187*, 551-576.

Ingber, L. (1989). Very fast simulated re-annealing, *Math. Comp. Model.* , *12*, 967-973.

Julia , J., C. J. Ammon, and R. B. Herrmann (2003), Lithospheric structure of the Arabian Shield from the joint inversion of receiver functions and surface-wave group velocities, *Tectonophysics*, *371*, 1-21.

Julia , J., C. J. Ammon, and A. A. Nyblade (2005), Evidence for mafic lower crust in Tanzania, East Africa, from joint inversion of receiver functions and Rayleigh wave dispersion velocities, *Geophys. J. Int.*, *162*, 555-569.

Julia, J., C. Ammon, R. Herrmann, and A. M. Correig (2000), Joint inversion of receiver function and surface wave dispersion observations, *Geophys. J. Int.*, *143*, 99-112.

Kaban, M. K., M. Tesauro, and S. Cloetingh (2010), An integrated gravity model for Europe's crust and upper mantle, *Earth Planet. Sci. Lett.*, *296*, 195-209.

Keller, G.R., and D.H. Shurbet (1975), Crustal structure of the Texas Gulf Coastal Plain, *Geol. Soc. Am. Bull.*, 86, 807-810.

Keller, G.R., and Jr. R. D. Hatcher (1999), Some comparisons of the structure and evolution of the southern Appalachian-Ouachita orogen and problems of the trans-European suture zone region, *Tectonophysics*, 314, 43-68.

Kennett, B., E. Engdahl, and R. Buland (1995), Constraints on seismic velocities in the Earth from traveltimes, *Geophys. J. Int.*, 122, 108-124.

Kirkpatrick, S., C. D. Gelatt, and M.P. Vecchi (1983), Optimization by simulated annealing, *science*, 220, 671-680.

Langston, C. A. (1979), Structure under Mount Rainier, Washington, inferred from teleseismic body waves, *J. Geophys. Res.: Solid Earth*, 84, 4749-4762.

Larose, E., A. Khan, Y. Nakamura, and M. Campillo (2005), Lunar subsurface investigated from correlation of seismic noise, *Geophys. Res. Lett.*, 32.

Lawrence, J. F., and D. A. Wiens (2004), Combined receiver-function and surface wave phase-velocity inversion using a niching genetic algorithm: application to Patagonia, *Bull. Seismol. Soc. Am.*, 94, 977-987.

Levshin, A., M. Ritzwoller, M. Barmin, and J. Stevens (2001), Short period group velocity measurements and maps in central Asia, *techreport*.

Li, X., S. Sobolev, R. Kind, X. Yuan, and C. Estabrook (2000), A detailed receiver function image of the upper mantle discontinuities in the Japan subduction zone, *Earth Planet. Sci. Lett.*, 183, 527 - 541.

Ligorria, J. P., and C. J. Ammon (1999), Iterative deconvolution and receiver-function estimation, *Bull. Seismol. Soc. Am.*, 89, 1395-1400.

Lines, L. R., A. K. Schultz, and S. Treitel (1988), Cooperative inversion of geophysical data, *Geophysics*, 53, 8--20.

Lundin, E.R., and G. Dore (2011), Hyperextension, serpentization, and weakening: A new paradigm for rifted margin compressional deformation, *Geol. Soc. Am.*, 39, 347-350.

Marton, G., and R. T. Buffler (1994), Jurassic reconstruction of the Gulf of Mexico basin, *Int. Geol. Rev.*, 36, 545-586.

Menard, H.W. (1967), Transitional types of crust under small ocean basins, *J. Geophys. Res.*, 72, 3061-3073.

- Mercier, J.-P., M. G. Bostock, and A. M. Baig (2006), Improved Green's functions for passive-source structural studies, *Geophysics*, *71*, SI95--SI102.
- Merle, O. (2011), A Simple Continental Rift Classification, *Tectonophysics*, *513*, 88-95.
- Menzies, M.A., S. L. Klemperer, C. J. Ebinger, and J. Baker (2002), Characteristics of volcanic rifted margins, *Geol. Soc. Spec. Pap.*, *362*, 1-14.
- Metropolis, N., A. W. Rosenbluth, M. N. Rosenbluth, A. H. Teller, and E. Teller (1953), Equation of state calculations by fast computing machines, *J. Chem. Phys.*, *21*, 1087–1092.
- Mickus, K.L., and G. R. Keller (1992), Lithospheric structure of the south-central United States, *Geology*, *20*, 335-338.
- Mickus, K., R. J. Stern, G. Keller, and E. Y. Anthony (2009), Potential field evidence for a volcanic rifted margin along the Texas Gulf Coast, *Geology*, *37*, 387--390.
- Mjelde, R., T. Raum, Y. Murai, and T. Takanamic (2007), Continent-ocean transitions: Review, and a new tectono-magmatic model of the Voring Plateau, NE Atlantic: *J. Geodyn.*, v. 43, p. 374-392, doi: 10.1016/j.jog2006.09.013.
- Molina-Garza, R.S., R. Van der Voo, and J. Urrutia- Fucuguachi (1992), Paleomagnetism of the Chiapas massif, southern Mexico: Evidence for rotation of the Maya block and implications for the opening of the Gulf of Mexico, *Geol. Soc. Am. Bull.*, *104*, 1156-1168.
- Mosher, S., J. S. F. Levine, and W. D. Carlson (2008), Mesoproterozoic plate tectonics: A collisional model for the Grenville-aged orogenic belt in the Llano uplift, central Texas, *Geology*, *36*, 55-58.
- Mutter, J.C., M. Talwani, and P. L. Stoffia (1984), Evidence for a thick oceanic crust adjacent to the Norwegian margin, *J. Geophys. Res.*, *89*, 483- 502.
- Nagihara, S., C. Christie, N. Ogiyamien, R. Oladokun, O. Ajiboye, and S. Ojeda (2012), Gulf of Mexico borehole geothermal data integration into the national geothermal data systems, part 1: Texas continental shelf, Gulf Coast Assoc. Geol. Soc. Trans., *62*, 589–591.
- Nettles, M., and A. Dziewonski (2008), Radially anisotropic shear velocity structure of the upper mantle globally and beneath North America, *J. Geophys. Res.*, *113*, B02303.
- O'Reilly, B.M., F. Hauser, A. W. B. Jacob, and P. M. Shannon (1996), The lithosphere below the Rockall Trough: Wide-angle seismic evidence for extensive serpentinization, *Tectonophysics*, *255*, 1-23.

Owens, T. J., A. A. Nyblade, H. Gurrola, and C. A. Langston (2000), Mantle transition zone structure beneath Tanzania, east Africa, *Geophys. Res. Lett.*, *27*, 827-830.

Ozalaybey, S., M. K. Savage, A. F. Sheehan, J. N. Louie, and J. N. Brune, (1997), Shear-wave velocity structure in the northern Basin and Range province from the combined analysis of receiver functions and surface waves, *Bull. Seismol. Soc. Am.*, *87*, 183-199.

Pasyanos, M. E. (2005), A variable resolution surface wave dispersion study of Eurasia, North Africa, and surrounding regions, *J. Geophys. Res.: Solid Earth (1978-2012)*, *110*.

Pindell, J. L., and L. Kennan (2009), Tectonic evolution of the Gulf of Mexico, Caribbean and northern South America in the mantle reference frame: an update, *Geol. Soc. London Spec. Publ.*, *328*, 1-55.

Pindell, J.L., and J. F. Dewey (1982), Permo-Triassic reconstruction of western Pangea and the evolution of the Gulf of Mexico/Caribbean region, *Tectonics*, *1*, 179-211.

Pindell, J. L. (1994), Evolution of the Gulf of Mexico and the Caribbean, in S. K. Donovan and T. A. Jackson, eds., Caribbean geology, *An introduction: Kingston, University of the West Indies Publishers Association*, 13-39.

Reston, T.J., J. Pennell, A. Stubenrauch, I. Walker, and M. P. Gussinye (2001), Detachment faulting, mantle serpentinization, and serpentinite-mud volcanism beneath Porcupine Basin, southwest of Ireland, *Geol. Soc. Am.*, *29*, 587-590.

Ritzwoller, M. H., & A. L. Levshin (1998), Eurasian surface wave tomography: Group velocities, *J. Geophys. Res.: Solid Earth (1978-2012)*, *103*, 4839-4878.

Ross, M. I., and C. R. Scotese (1988), A hierarchical tectonic model of the Gulf of Mexico and Caribbean region, *Tectonophysics*, *155*, 139-168.

Russell, D. R., R. B. Herrmann, and H. J. Hwang (1988), Application of frequency variable filters to surface-wave amplitude analysis, *Bull. Seismol. Soc. Am.*, *78*, 339-354.

Schroeder, T., B. John, and B. R. Frost (2002), Geologic implications of seawater circulation through peridotite exposed at slow-spreading ridges, *Geology*, *30*, 367-370.

Sen, M. K., and P. L. Stoffa (1995), Global optimization methods in geophysical inversion, Elsevier.

Shapiro, N. M., and M. Campillo (2004), Emergence of broadband Rayleigh waves from correlations of the ambient seismic noise, *Geophys. Res. Lett.*, *31*.

Shervais, J.W., P. Kolesar, and K. Andreasen (2005), A field and chemical study of serpentinization- Stonyford, California: chemical flux and mass balance, *Int. Geol. Rev.*, *47*, 1-23.

Snieder, R. (2004), Extracting the Green's function from the correlation of coda waves: A derivation based on stationary phase, *Physical Review E*, 69, 046610.

Stern, R. J., E. Y. Anthony, M. Ren, B. E. Lock, I. Norton, and J. I. Kimura (2011), Southern Louisiana salt dome xenoliths: First glimpse of Jurassic (ca. 160 Ma) Gulf of Mexico crust, *Geology*, 39, 315-318.

Tesauro, M., M.K. Kaban, W.D. Mooney, and S. Cloetingh (2014), NACr14: A 3D model for the crustal structure of the North American Continent, *Tectonophysics*, 631, 65-86.

Thomas, W.A. (1991), The Appalachian-Ouachita rifted margin of southeastern North America, *Geol. Soc. Am. Bull.*, 103, 415-431.

Thomas, W.A. (2005), Tectonic inheritance at a continental margin, *Geol. Soc. Am. Tod.*, 16, 2.

Tkalcic, H., M. Pasyanos, A. Rodgers, R. Cakir, W. Walter, and A. Al-Amri (2006), A multistep approach for joint modeling of surface wave dispersion and teleseismic receiver functions: Implications for lithospheric structure of the Arabian Peninsula, *J. Geophys. Res.: Solid Earth (1978-2012)*, 111.

Walker, N.W. (1992), Middle Proterozoic geologic evolution of Llano uplift, Texas: Evidence from U-Pb zircon geochronometry, *Geol. Soc. Am. Bull.*, 104, 494-504.

Walter, D. M., and M.K. Kaban (2010), The North American upper mantle: Density, composition, and evolution, *J. Geophys. Res.*, 115, B12424.

Wapenaar, K. (2004), Retrieving the elastodynamic Greens function of an arbitrary inhomogeneous medium by cross correlation, *Phys. Rev. Lett.*, 93, 254301.

Weaver, R. L., and O. I. Lobkis (2001), On the emergence of the Green's function in the correlations of a diffuse field, *J. Acous. Soc. Am.*, 110, 3011-3017.

Weaver, R. L., and O. I. Lobkis (2004), Diffuse fields in open systems and the emergence of the Green's function (L), *J. Acous. Soc. Am.*, 116, 2731--2734.

Whitmarsh, R. B., and D. S. Sawyer (1996), The ocean/continent transition beneath the Iberia Abyssal Plain and continental-rifting to seafloor spreading processes, *Proc. Ocean Drill. Program Sci. Results*, 149, 713-733, 1996.

Whitmeyer, S. J., and Karlstrom, K. E. (2007), Tectonic model for the Proterozoic growth of North America, *Geosphere*, 3, 220--259.

White, R., and D. P. McKenzie (1989), Magmatism at rift zones: The generation of volcanic continental margins and flood basalts, *J. Geophys. Res.*, 94, 7685-7729.

Young, H., and C. T. Lee (2009), Fluid-metasomatized mantle beneath the Ouachita belt of southern Laurentia: Fate of lithospheric mantle in a continental orogenic belt, *Lithosphere*, 1, 370--383.

Zhao, L.-S., M. K. Sen, P. Stoffa, and C. Frohlich (1996), Application of very fast simulated annealing to the determination of the crustal structure beneath Tibet, *Geophys. J. Int.*, 125, 355--370.

Zheng, T., L. Chen, L. Zhao, W. Xu, and R. Zhu (2006), Crust-mantle structure difference across the gravity gradient zone in North China Craton: Seismic image of the thinned continental crust, *Phys. Earth Planet. Int.*, 159, 43 - 58.

Zhu, L. (2000), Crustal structure across the San Andreas Fault, southern California from teleseismic converted waves, *Earth Planet. Sci. Lett.*, 179, 183 - 190.

## CHAPTER FOUR

Lithospheric removal beneath the eastern flank of the Rio Grande Rift from receiver function velocity analysis

This chapter submitted as: Agrawal, M., J. Pulliam, M.K. Sen and S.P. Grand (in review), Lithospheric structure of the eastern flank of the Rio Grande Rift via receiver function velocity analysis, *Journal of Geophysical Research*.

### *Abstract*

We develop and apply a technique for receiver function processing that is analogous to “velocity analysis” in seismic reflection processing, in which a velocity model that is sufficiently accurate for the purpose of migrating reflection events is found directly from the data. In the case of receiver functions, which represent waves converted from P- to S-type (Ps) or S- to P-type (Sp) rather than reflected waves, we jointly optimize the average correlation value for target features in common receiver gathers while perturbing shear wave velocities and Poisson’s ratio in a process driven by simulated annealing. The technique simultaneously finds depths to major discontinuities (in this case the Moho and seismically-determined Lithosphere-Asthenosphere Boundary (LAB)) and S velocity profiles beneath each seismic station. Estimates of Poisson’s ratio are used in conjunction with the S velocity model to produce a P velocity model and individual, 1D profiles are interpolated to form a 3D velocity models.

To investigate subsurface structure beneath the eastern flank of the Rio Grande Rift, we stacked and depth-migrated Ps and Sp receiver functions computed from data

recorded by broadband stations deployed by the SIEDCAR (Seismic Investigation of Edge Driven Convection

Association with Rio Grande Rift) project and the USArray Transportable Array (TA) in southeastern New Mexico and west Texas. Receiver function images computed with these data reveal an abrupt increase in lithospheric thickness from the Rio Grande Rift, in the west, to the Great Plains craton, in the east. Ps results show that the Moho ranges from 36 km to 54 km in the region, while Sp results show variations in the LAB of 75-112 km.

Previous tomography results revealed an elongated high velocity anomaly that extends to depths approaching 400 km in southeastern New Mexico and west Texas that is distinct from the Great Plains lithosphere. Our stacked 3D images indicate that thick crust and thick lithosphere overlie this anomaly. Areas of thickened crust and lithosphere are elongated in a northwest-southeast direction. We speculate that the thickened crust and lithosphere might be due to removal of the lower lithosphere by a process that is associated with east-west extension, and thus the northward propagation, of the Rio Grande Rift.

## *Introduction*

Bounded by the Basin and Range province and the Colorado Plateau, to the west, and the Great Plains, to the east, the Rio Grande Rift (RGR) extends at least 1000 km from central Colorado to Chihuahua, Mexico, where its boundaries become indistinct (Figure 1). The RGR exhibits recent volcanism, steep fault scarps, and active seismicity and is widening at a modest rate of  $\sim 0.5$  mm/yr or less [Berglund *et al.*, 2011; Kreemer *et al.*, 2010; Woodward, 1977]. Although many studies have focused on the rift system [Averill, 2007; Gao, 2004; Keller, 1999; Roy *et al.*, 2005; van Wijk *et al.*, 2008; Wilson, 2005a, 2005b] the eastern flank of the RGR and the nature of the transition from the RGR to the Great Plains “craton” remain poorly understood [Keller, 1999]. For example, few seismic studies have provided detailed information on the deeper structure of this region [Averill, 2007; Gao, 2004; Wilson, 2005b] and a great variety of possible Earth models and interpretations have been presented for the RGR [*e.g.*, Gao, 2004; Moucha *et al.*, 2008; van Wijk *et al.*, 2008].

Olsen *et al.* [2008] suggested three different mechanisms for rifting. In the first scenario, hot asthenosphere uplifts the lithosphere, producing volcanism in an “active rifting” process. The second scenario involves lateral forces at great distances pulling the lithosphere apart, a “passive rifting” process that produces extension and normal faulting, leading to subsidence and crustal thinning. The asthenosphere then rises to fill the void left by the thinned lithosphere. The third scenario involves a piece of the lithosphere delaminating (peeling away) from the crust, causing upwelling of hot asthenosphere. Each of these mechanisms has remained plausible in the absence of definitive seismic or geophysical data. Results from a previous study, called “La Ristra”, found a seismically

fast anomaly beneath the eastern flank of the RGR which has been interpreted to indicate a downwelling, possibly associated with lithospheric delamination or small-scale convection [Gao, 2004]. While these results suggest a possible connection between dynamic mantle downwelling and crustal and surface structure, the anomaly is located near the southeastern edge of the linear La Ristra seismic deployment so, based on the La Ristra deployment alone, its lateral extent is uncertain.

To better constrain the seismic structure of crust and upper mantle beneath the eastern flank of the RGR, a 2D array of broadband seismographs was deployed on the eastern flank of the rift for a period of two years, from 2008 through 2010 (Figure 1). The Seismic Investigation of Edge Driven Convection Associated with the Rio Grande Rift (SIEDCAR) installed a total of 71 broadband stations interspersed between EarthScope Transportable Array (TA) stations, with 18 km average spacing between adjacent stations. We analyze Ps and Sp conversions using a novel receiver function method to determine the depth of the Moho and seismically-defined LAB, as well as to estimate the impedance contrast across the major discontinuities beneath the eastern flank of the RGR. The relatively small station spacing allows for high-resolution 3D images of the crust and upper mantle to be constructed through the region.

Since the pioneering work of Langston [1979], seismologists have used receiver functions to identify impedance contrasts in the Earth's crust and upper mantle. The basic method uses teleseismic earthquake data to find depths at which waves are converted from P-type to S-type, or vice versa, beneath seismic stations. Common Conversion Point (CCP) stacking averages many closely-spaced receiver functions to improve signal-to-noise ratios; seismic "depth migration" transforms a stacked receiver function image

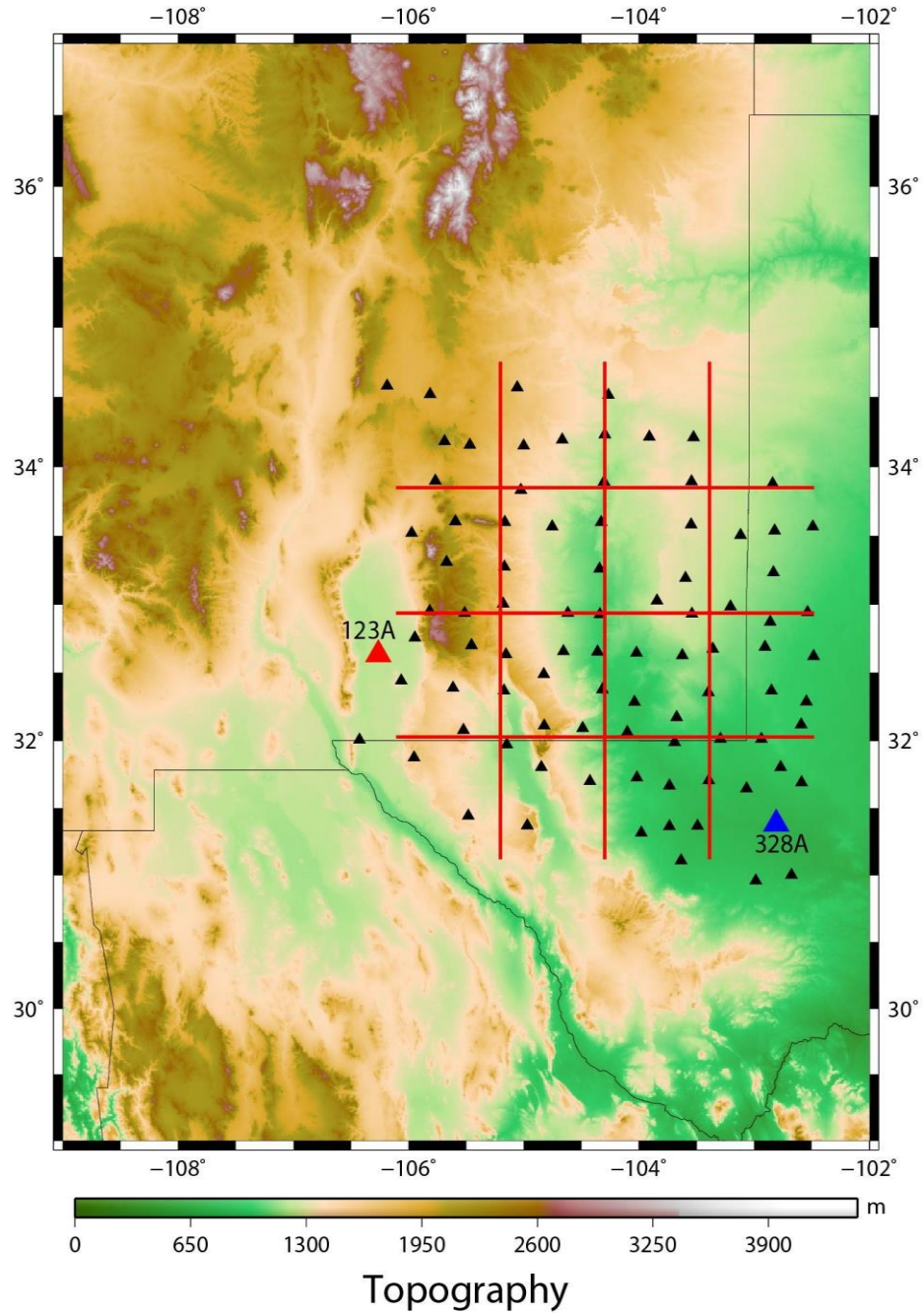


Figure 4.1. Regional topography of the southwestern United States centered on the Rio Grande Rift. The SIEDCAR deployment is located on the east flank of the Rift. Black triangles are SIEDCAR and USArray Transportable Array (TA) stations. Red lines represents the location of three west-east (DD', E-E' and F-F') and south-north (A-A', B-B' and C-C') profiles used for generating Ps and Sp CCP images. Stations 123A and 328A (for which example receiver functions are shown in later figures) are shown in red and blue colors, respectively.

from the time domain to the depth domain [*Dueker and Sheehan, 1997; Lekić and Fischer, 2014; Li et al., 2000; Owens et al., 2000; Zhu and Kanamori, 2000*]. Depth migration allows the image to be interpreted in terms of geological structure, removes wave diffractions, and corrects inaccurate locations and dips of features.

Using an incorrect velocity model for time-to-depth migration of a stacked CCP image will produce an inaccurate image of the subsurface, especially in the presence of substantial lateral velocity variations; yet reliable velocity models are not always available. One common approach to estimating velocities is to perform travel time tomography, using teleseismic earthquakes (because they are often plentiful) augmented by regional and local earthquakes (events with epicentral distances less than 1000 km), if they are available. However, the SIEDCAR study area offers relatively few regional or local events, particularly to the east, so travel time tomography relies heavily on teleseismic events. Rays from teleseismic events arrive at seismic stations with steep angles of incidence and subparallel trajectories that intersect only sparsely in the 0–200 km depth range. Teleseismic tomography with station spacing greater than 20 km, therefore, produces relatively poor constraints on the Earth’s crust and uppermost mantle, which is the portion of the model for which accuracy is most critical to receiver function imaging. In regions with extremely low velocities, such as the RGR, teleseismic raypaths are particularly steep through the crust. This shortcoming is often more severe for shear wave tomography because picking S wave arrivals is more difficult than picking the first-arriving P wave, so data sets used for S wave tomography tend to be smaller and to represent sparser coverage, than those used for P wave tomography. Both P and S-

velocity models are needed to migrate images produced with P-to-S or S-to-P converted waves.

We therefore find sufficiently accurate P- and S-velocity models for migration through a procedure that is analogous to “velocity analysis” in reflection seismology [Varela *et al.*, 1998]. We jointly optimize the average correlation value of common receiver gathers of Ps and Sp receiver functions for target features while perturbing the shear wave velocities in a process driven by simulated annealing. The technique, discussed in detail in a later section, simultaneously finds depths to major discontinuities (in this case the Moho and LAB) and S and P velocity profiles beneath each seismic station.

### *Geologic Setting and Previous Studies*

The southwestern United States is composed of several distinct tectonic blocks (Figure 2). The Great Plains, which form the western edge of the North American craton, have not undergone significant deformation since Precambrian time. The Colorado Plateau, to the west, has also been generally tectonically stable since Precambrian time but has an average elevation of about 1.8 km at present [Morgan and Swanberg, 1985]. Cretaceous marine sediments on top of the Plateau indicate the current elevation is relatively recent although the exact timing of the uplift is controversial [Chase *et al.*, 2002; Sahagian *et al.*, 2002]. Surrounding the Colorado Plateau to the south and west lies the Basin and Range province, which has undergone episodes of extension and deformation since the mid-Tertiary [Parsons, 1995]. Between the Plateau and the Great Plains lies the Rio Grande Rift (Figure 2). Extension within the rift has occurred during two episodes: from ~35 to ~20 Ma and again from ~10 Ma until ~3 Ma [Gao, 2004].

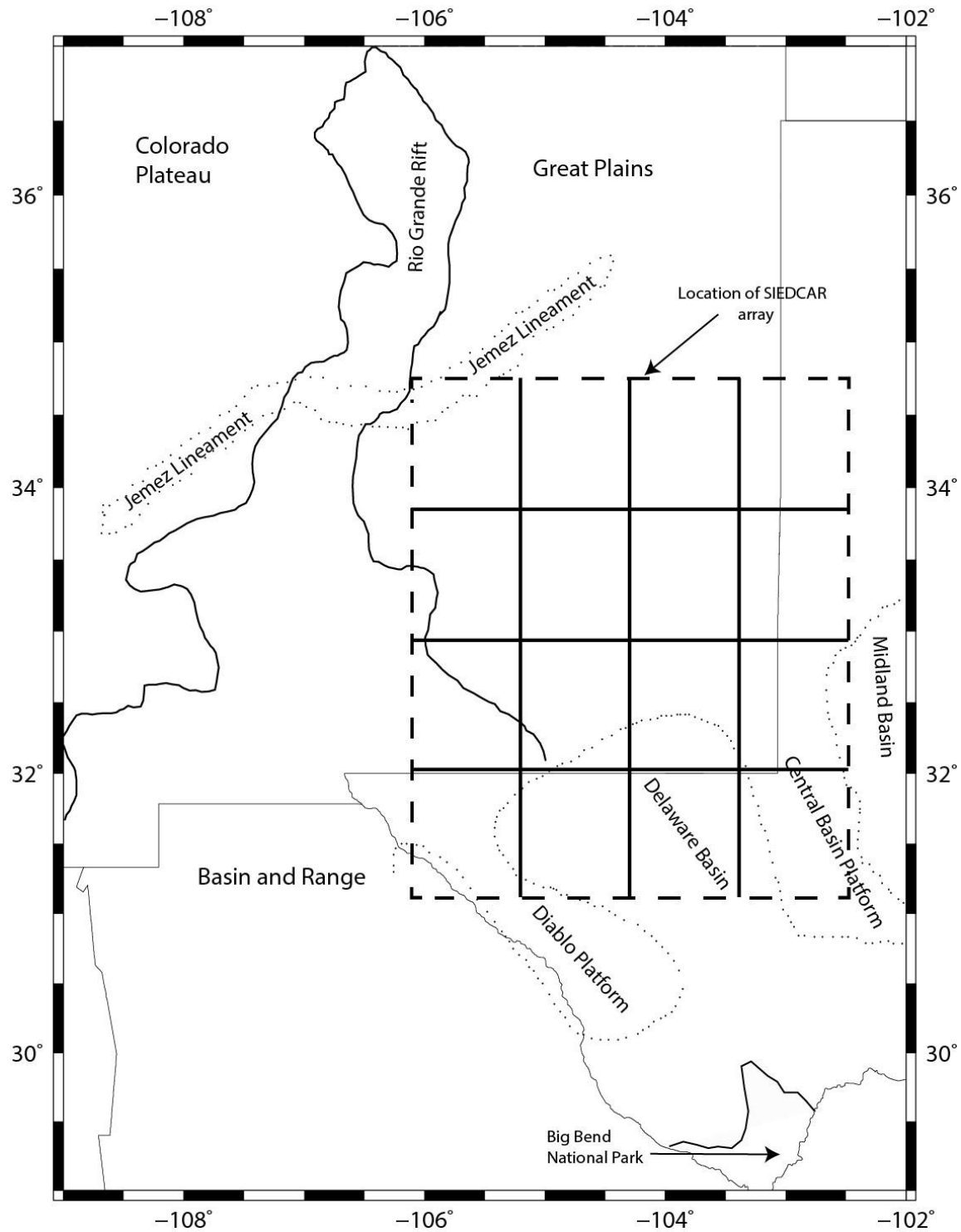


Figure 4.2. Geological map of major tectonic features in southeastern New Mexico and west Texas. Dashed and solid black lines show the location of our study area.

Magmatic activity accompanied both periods of rapid extension while the time between rapid extension events was accompanied by a lull in magmatism [*Baldrige et al.*, 1991; *Morgan et al.*, 1986]. At present, most active volcanism in the rift occurs along the Jemez lineament on the western side of the RGR [*Baldrige et al.*, 1991], although the Jemez lineament crosses the RGR with a southwest-northeast-oriented trend and there is minor volcanic activity along the eastern side of the rift as well.

The Central Basin Platform (CBP) is a northwest-southeast-trending uplifted basement block that separates the Midland Basin (to the east) from the Delaware basin (to the west) (Figure 2). The CBP was uplifted in mid-to-late Pennsylvanian time; until then the two basins and the CBP were relatively low-relief features. The western boundary of Midland Basin (MB) is delineated by complex folds and faults that have formed along the eastern margin of the CBP. The eastern basin boundary is somewhat indistinct and is designated the Eastern Shelf. The Eastern shelf represents a gradual rise from the western, deepest part of the basin. The Delaware and Midland Basins differ significantly; the Delaware Basin is deeper and more asymmetric than the Midland Basin and deepens to the east, whereas the Midland Basin deepens to the west. The western margin of the Delaware Basin is bounded by the Salt Flat Graben, a Tertiary-age system related to Basin and Range extensional tectonics. Further to the west lies the Diablo Platform, a paleogeographic high that has persisted since the Paleozoic (Figure 2).

Previous tomography showed a high velocity anomaly that extends to depths perhaps approaching 400 km just to the west of the Great Plains craton [*Gao*, 2004]. This anomaly was interpreted as downwelling cold lithosphere that is perhaps related to edge-driven convection [*Buck*, 1986; *van Wijk et al.*, 2008]. *Van Wijk et al.* [2008] suggested

that a strong lateral temperature gradient in the lithosphere is the cause of the downwelling [van Wijk *et al.*, 2008]. Some numerical modeling studies suggest that an abrupt change in lithospheric thickness may produce a gravitational instability that leads to thicker mantle lithosphere dripping off into the lower density asthenosphere [King, 2007; van Wijk *et al.*, 2010] with little or no impact on the overlying crust and surface topography. However, numerical modeling that produces delamination near the Moho includes significant surface uplift [Stern *et al.*, 2013].

### *Data*

Teleseismic earthquake data recorded by 89 broadband seismic stations were used to perform receiver function imaging (Figure 1). More than 500 teleseismic earthquakes of magnitude greater than 5.5 that occurred between July 2008 and July 2010 were selected to create receiver functions. Individual Ps and Sp receiver functions were computed using earthquakes at epicentral distances between 30°-90° and 60°-85°, respectively. Because of the ray trajectories specific to S-toP converted phases, earthquakes used to compute Sp receiver function are limited to a fairly narrow range of epicentral distances [Wilson *et al.*, 2006]. After removing poor quality receiver functions, we emerged with a total of 4,170 high quality Ps receiver functions and 1,736 high quality Sp receiver functions.

### *Methodology*

The methodology we employed is shown schematically in Figure 3 and is described in the following.

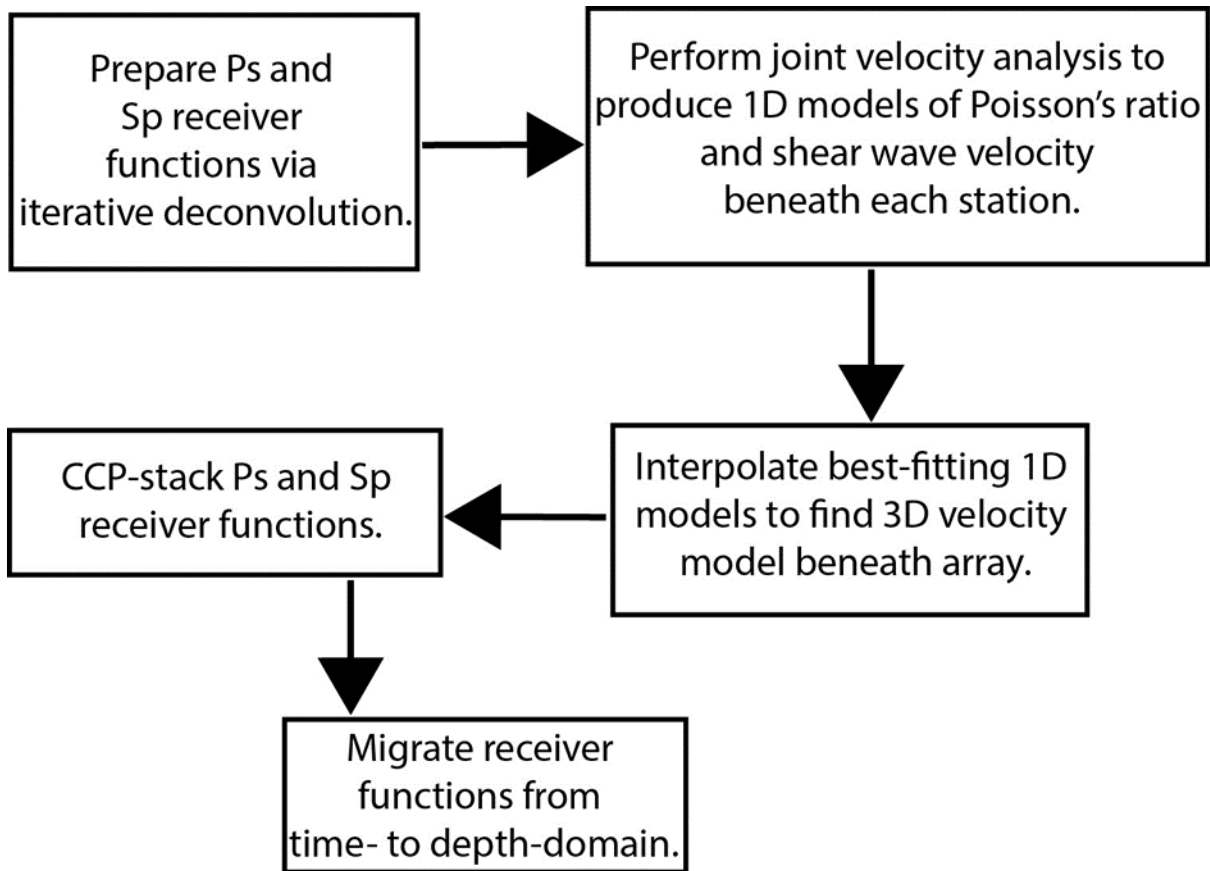


Figure 4.3. The methodology employed to construct 3D receiver function images beneath the SIEDCAR seismic array (Figure 1). The velocity analysis in step 2 consists of iteratively perturbing model parameters (Poisson's ratio,  $V_s$ , and layer thickness) in a process driven by simulated annealing. See text for further details.

*Step 1: Compute Ps and Sp receiver functions.* Receiver function calculation involves two main steps: rotation and deconvolution [Li *et al.*, 2004]. Waveforms were rotated from Z–N–E (vertical, north south, east–west) components to a Z–R–T (vertical, radial, transverse) reference frame using stationevent backazimuths and were manually inspected to pick the P-wave arrival and S-wave arrival for Ps and Sp receiver functions, respectively, using the Seismic Analysis Code (SAC) [Kind and Vinnik, 1988; Kumar, 2005]. We then windowed the seismograms to 10 s before and 40 s after the P-wave

arrival for Ps receiver functions and 40 s before and 10 s after the S-wave arrival for Sp receiver functions.

The polarity of an S-to-P conversion at a given interface is the opposite of the P-to-S conversion. Also, because P velocities are greater than S velocities, conversions at deeper boundaries arrive before conversions at shallower boundaries for Sp receiver functions, unlike Ps receiver functions. So, for ease of comparison in displays, the polarities and time axes were reversed for Sp receiver functions, as is common [Kumar, 2005]. We use an iterative time domain deconvolution approach for the computation of receiver functions [Kikuchi and Kanamori, 1982; Ligorría and Ammon, 1999]. We found that a Gaussian factor ( $\alpha$ ) of 2.0 attenuates most of the high frequency noise; a 0.04-2.0 Hz band-pass filter was applied on raw seismograms to compute receiver functions. Examples of Ps and Sp receiver function variations are shown vs. backazimuths for station 123A in Figure 4.

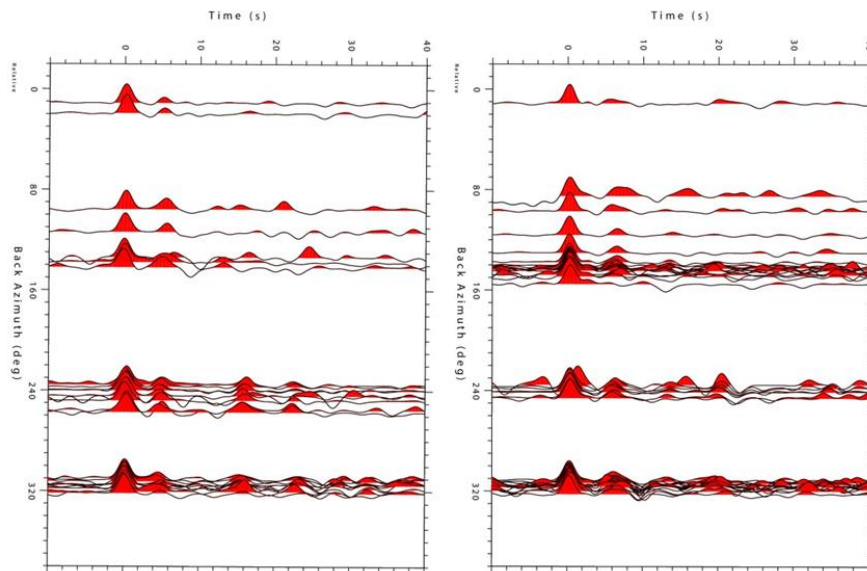


Figure 4.4. Left and right panels show Ps and Sp receiver functions as a function of backazimuth for station 123A.

*Step 2: Joint velocity analysis of Ps and Sp receiver functions using Very Fast Simulated Annealing (VFSA).* Ps and Sp receiver functions both constrain impedance contrasts across discontinuities and thicknesses of layers between discontinuities [Ammon *et al.*, 1990]. However, Ps receiver functions are more sensitive to average Vs in the lithosphere while Sp receiver functions are more sensitive to average Vp in the lithosphere [Yuan *et al.*, 2006]. Aside from constraints on Vp, Sp receiver functions offer additional benefits compared to Ps receiver functions. They are free from shallow layer multiples in the arrival window of the main converted Sp phases, because the converted Sp phase arrives earlier than the direct S phase [Faber and Muller, 1980; Farra and Vinnik, 2000; Kumar, 2005; Kumar *et al.*, 2005; Li *et al.*, 2004], and they sample a much greater distance laterally. Mutually satisfying constraints imposed by these two complementary datasets may constrain a larger portion of the model parameter space (thereby increasing “uniqueness”) than a single set alone [Agrawal *et al.*, 2015; Çakır and Erduran, 2004; Dugda and Nyblade, 2006; Julià *et al.*, 2005, 2000; Ozalaybey *et al.*, 1997; Pasyanos, 2005; Tkalčić *et al.*, 2006].

One goal of this study is to find a 3D seismic velocity model using the complementary datasets mentioned above. This model will allow us to migrate the CCP stacked Ps and Sp receiver functions and place major discontinuities (e.g., Moho, LAB) to their correct depths because it makes use of waves that sample Earth structure in different, but complementary, ways. This is an important feature because the impedance contrasts implied by observed Moho and LAB events can divert raypaths dramatically from their trajectories in a smooth structure, thereby degrading the quality and fidelity of the resulting images. These boundaries can be revealed by receiver function modeling (as

discussed above) and then introduced as a starting model used while migrating the CCP stacked Ps and Sp receiver functions.

We therefore find a 3D model by jointly optimizing the average correlation value of common receiver function gathers for Ps and Sp receiver functions while perturbing Poisson's ratio, shear wave velocities and the thickness of each layer in a process driven by Very Fast Simulated Annealing (VFSA) [Aarts and Korst, 1989; M. Agrawal et al., 2015; Geman and Geman, 1984; Kirkpatrick et al., 1983; Sen and Stoffa, 1995]. This technique simultaneously finds the depths to major discontinuities, S-velocity and Poisson's ratio for 1D profiles beneath each seismic station in a manner that is similar to velocity analysis in reflection seismology. Details of VFSA can be found in Sen and Stoffa (1995). For each station, an ak135 input 1D velocity model was varied within a predefined model parameter space to convert the time domain receiver function gather to the depth domain. At each iteration of VFSA we migrate time domain Ps receiver function gathers to the depth domain using the formula given in equation (1) and the current iteration's velocity model. Assuming the incident P-wave to be a plane wave (which is acceptable in receiver function studies when the epicentral distance is greater than 30<sup>0</sup>) and the Earth to consist of multiple, homogeneous, horizontally-stratified layers, the travel time delay between the direct P arrival and the Ps conversion can be found from the ray parameter,  $p$ :

$$\Delta t = t_{ps} - t_p = \sum_{i=1}^N Z_i \left( \sqrt{\frac{1}{\beta_i^2} - p^2} - \sqrt{\frac{1}{\alpha_i^2} - p^2} \right) \quad (1)$$

where the subscript ' $i$ ' denotes the number of the layer from the free surface to the bottom,  $Z$  represents the thickness of the  $i^{\text{th}}$  layer, and  $\alpha_i$  and  $\beta_i$  are P- and S-wave velocities of the  $i^{\text{th}}$  layer, respectively, and  $t_{ps}$  and  $t_p$  represent the travel times of the Ps

conversion and direct P-wave, respectively, from the discontinuity at which the Ps conversion occurred to the surface. Likewise, for migrating Sp receiver function gathers to the depth domain, we find the delay time between Sp conversions and direct S-arrivals using the following relation [Frederiksen and Bostock, 2000]:

$$\Delta t = t_{sp} - t_s = \sum_{i=1}^N Z_i \left( \sqrt{\frac{1}{\alpha_i^2} - p^2} - \sqrt{\frac{1}{\beta_i^2} - p^2} \right) \quad (2)$$

where  $t_{sp}$  and  $t_s$  represent the travel times of the Sp conversion and direct S wave from the discontinuity at which the Sp conversion occurred to the surface. Other variables are as described for equation (1).

For the model found at each iteration, depth receiver functions were stacked (both for Ps and Sp receiver functions) and an average correlation value was computed by correlating the stacked trace with individual receiver functions. This correlation value is compared with the previous iteration's correlation value and the current model is either accepted or rejected according to the set of rules defined by VFSA [Sen and Stoffa, 1995]. This process is repeated until the maximum correlation value is achieved (generally 500 iterations for each station). We use different model parameter spaces for the crust and mantle.

*Objective function:* We use the following objective function that outputs a single scalar value of cross-correlation for the  $j^{\text{th}}$  seismic station.

$$CC_j = \frac{\sum_i^N s \otimes t_i}{N_j} \quad (3)$$

The operator  $\otimes$  represents a cross-correlation function. For a particular station during the VFSA process, the model parameters are perturbed within user-defined ranges to convert a time domain receiver function gather to a depth domain receiver function gather. At

each iteration, depth domain receiver functions are stacked to form a single stacked receiver function trace  $\mathbf{S}$ . In equation (3),  $CC_j$  represents the average normalized cross correlation value (at zero lag) of  $\mathbf{S}$  with individual receiver function  $\mathbf{t}_i$  for seismic station  $j$ .  $\mathbf{t}_i$  is the  $i^{\text{th}}$  receiver function of a gather.  $N_j$  represents the total number receiver functions for station  $j$ . In generalized form, the objective function can be written as:

$$CC_k = \frac{\sum_{j=1}^{N_k} \frac{\sum_k \mathbf{t}_{rm}^k \cdot \mathbf{t}_r^{j,k}}{(\sum_k \mathbf{t}_{rm}^k \cdot \mathbf{t}_{rm}^k)^{1/2} (\sum_k \mathbf{t}_r^{j,k} \cdot \mathbf{t}_r^{j,k})^{1/2}}}{N^k}, \quad (4)$$

Where  $\mathbf{t}_{rm}^k$  and  $\mathbf{t}_r^{j,k}$  represent the stacked receiver function trace and the  $j^{\text{th}}$  receiver function of the gather for station  $k$ , respectively.  $N_k$  represents the total number of receiver functions for the  $k^{\text{th}}$  station. Equations (3) and (4) define the objective function for a single data functional. We optimize the joint error function for Ps and Sp receiver functions simultaneously to better constrain the model parameter space. Our joint error function for station  $k$  is

$$CC_k^{\text{joint}} = W_{ps} \left[ \frac{\sum_{ip}^{N_p} S^p \otimes \mathbf{t}_r^{ip}}{N_k^p} \right] + W_{sp} \left[ \frac{\sum_{is}^{N_s} S^s \otimes \mathbf{t}_r^{is}}{N_k^s} \right] \quad (5)$$

In equation (5),  $\mathbf{S}^p$  and  $\mathbf{S}^s$  represent the stacked trace of Ps and Sp depth domain receiver functions for station  $k$ , respectively.  $W_{ps}$  and  $W_{sp}$  represent weights assigned to Ps and Sp receiver functions; in this study we used equal weights for both types of receiver functions.  $N_k^p$  and  $N_k^s$  represent the total number of Ps and Sp receiver functions for the  $k^{\text{th}}$  seismic station while  $\mathbf{t}_r^{ip}$  and  $\mathbf{t}_r^{is}$  represent the  $i^{\text{th}}$  traces from Ps and Sp receiver functions from their respective depth domain receiver function gathers.

We cross-correlate stacked receiver function traces with individual receiver functions for a predefined depth range (e.g., 30-70 km for the Moho using Ps receiver

functions and 65-130 km for the LAB using Sp receiver functions). For those depth ranges, an average cross-correlation value is computed using equation (5). Then we optimize this value using VFSA as described above.

For Poisson's ratio and Vs, the crustal and mantle parameter space were  $\pm 5\%$  and  $\pm 3\%$ , respectively (Figure 5). Also, thicknesses of each layer were allowed to vary  $\pm 10\%$  and  $\pm 20\%$  for the crust and mantle, respectively. We set the initial temperature at  $10^{-4}$  dimensionless units and allowed it to cool to  $10^{-14}$  units for each VFSA run. We discovered, after a set of trials, that the misfit error changed very little after 400 iterations, so we set the maximum number of iterations to 500 to provide an adequate margin for error. Examples of resulting, optimum Moho and LAB depths are shown in Figures 6a and 6b, using Ps and Sp receiver functions gathers for stations 328A ( $32.63^{\circ}$ ,  $102.81^{\circ}$ ) and 123A ( $32.63^{\circ}$ ,  $-106.26^{\circ}$ ), respectively. Optimum joint correlation values for stations 328A and 123A are 0.82 and 0.78, respectively. Depths to the Moho beneath stations 328A and 123A are found to be 40 km and 60 km, respectively; depths to the LAB beneath these stations are 80 km and 100 km.

*Step 3. Interpolate optimized 1D profiles for each station to find a 3D velocity model.* For this step, we first use 1D Poisson's ratios and shear wave velocity profiles found in our previous step, to find 1D Vp profiles for each seismic station. These 1D models are interpolated to create the 3D shear and compressional wave velocity models beneath the 2D seismic array. Figure 7 shows horizontal crosssections through the interpolated Vp and Vs 3D perturbations. These 3D models were used to migrate the CCP-stacked Ps and Sp receiver functions from the time domain to the depth domain.

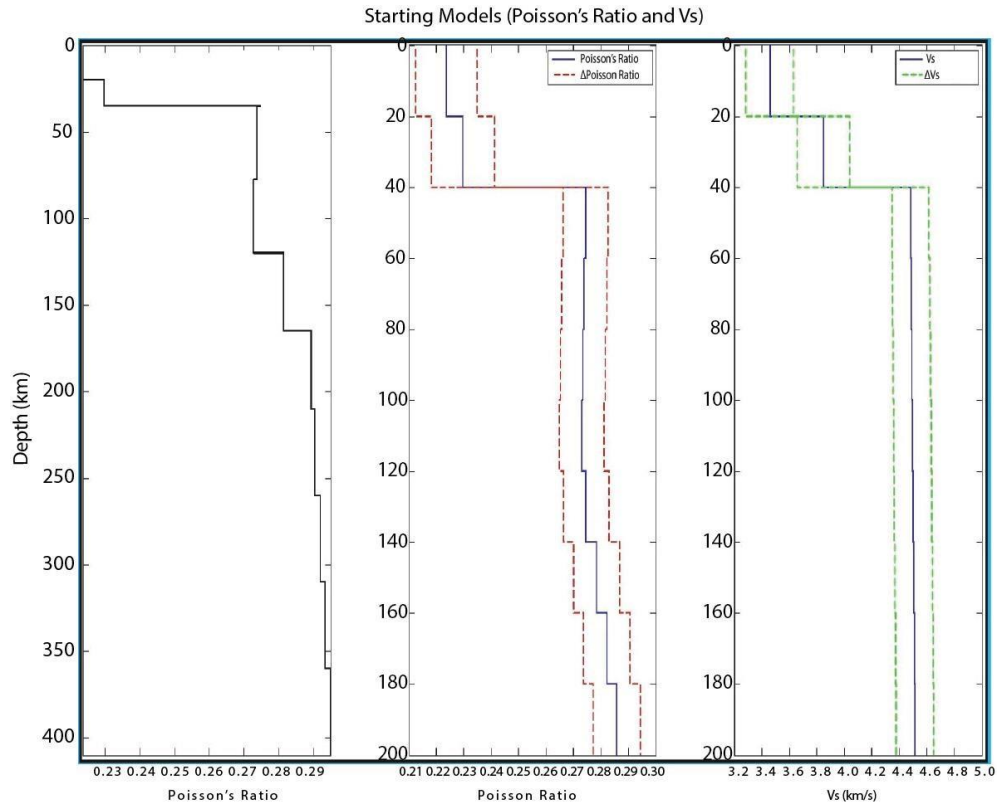


Figure 4.5. Starting models used for optimization via VFSA. The solid line in the leftmost figure shows model ak135, which was divided into 20-km depth bins from 0 to 200 km depth for Poisson's ratio and shear wave velocity ( $V_s$ ). Dashed lines in the middle figure show the model parameter search bounds for Poisson's ratio; dashed lines in the figure at right show the search space for  $V_s$ . Variations of crustal parameters were searched over a more extensive range ( $\pm 5\%$  of ak135) than mantle parameters ( $\pm 3\%$  of ak135). "Depth bins" (layer thicknesses) were allowed to vary  $\pm 10\%$  and  $\pm 20\%$  for the crust and mantle, respectively.

In the crust, a swath of moderately fast  $V_p$  and  $V_s$  velocities trends SW-NE in the southeastern portion of the study area. The southern lobe of the anomaly, beneath the Delaware Basin, extends into the upper mantle, where it is mirrored by another fast anomaly in the northwestern portion of the study area. A significantly smaller, slow anomaly appears in the uppermost mantle beneath the Central Basin Platform. The greatest lateral heterogeneity occurs in the depth range 40-60 km, in the uppermost mantle just below the crust.

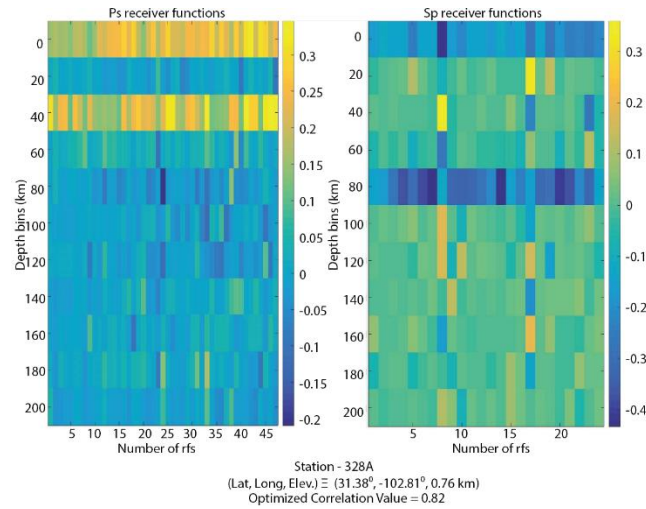


Figure 4.6a. Joint optimization results of Ps and Sp receiver function gathers for station 328A located at  $(31.38^{\circ}\text{N}, -102.81^{\circ}\text{W})$ ; amplitudes of receiver functions are indicated by colors. Optimum correlation values were found at depths of 40 km for Ps (yellow), which we interpret to be the Moho, and 80 km for Sp (blue), which we interpret to be the seismically-determined LAB. We optimize the average correlation value for target features (Moho and LAB) while perturbing the values of layer thicknesses, shear wave velocity and Poisson's ratio (see text for more details).

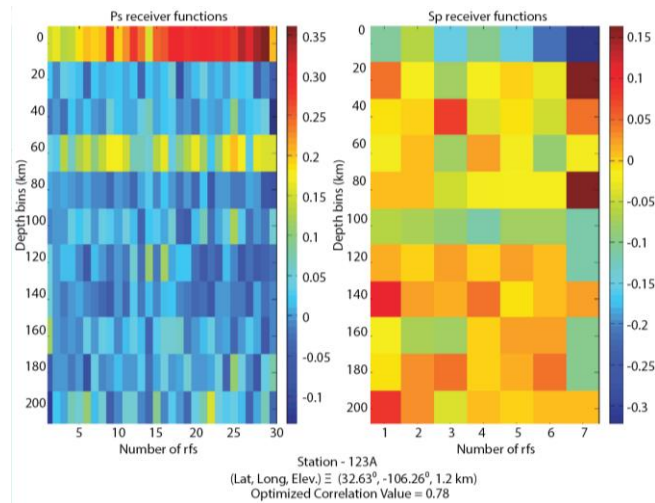


Figure 4.6b. Joint optimization results of Ps and Sp receiver function gathers for station 123A, located at  $(32.63^{\circ}\text{N}, -106.26^{\circ}\text{W})$ . Optimum correlation values were found at depths of 60 km for Ps (yellow), which we interpret to be the Moho, and 100 km for Sp (light green), which we interpret to be the seismically-determined LAB. Other details are as in Figure 6a.

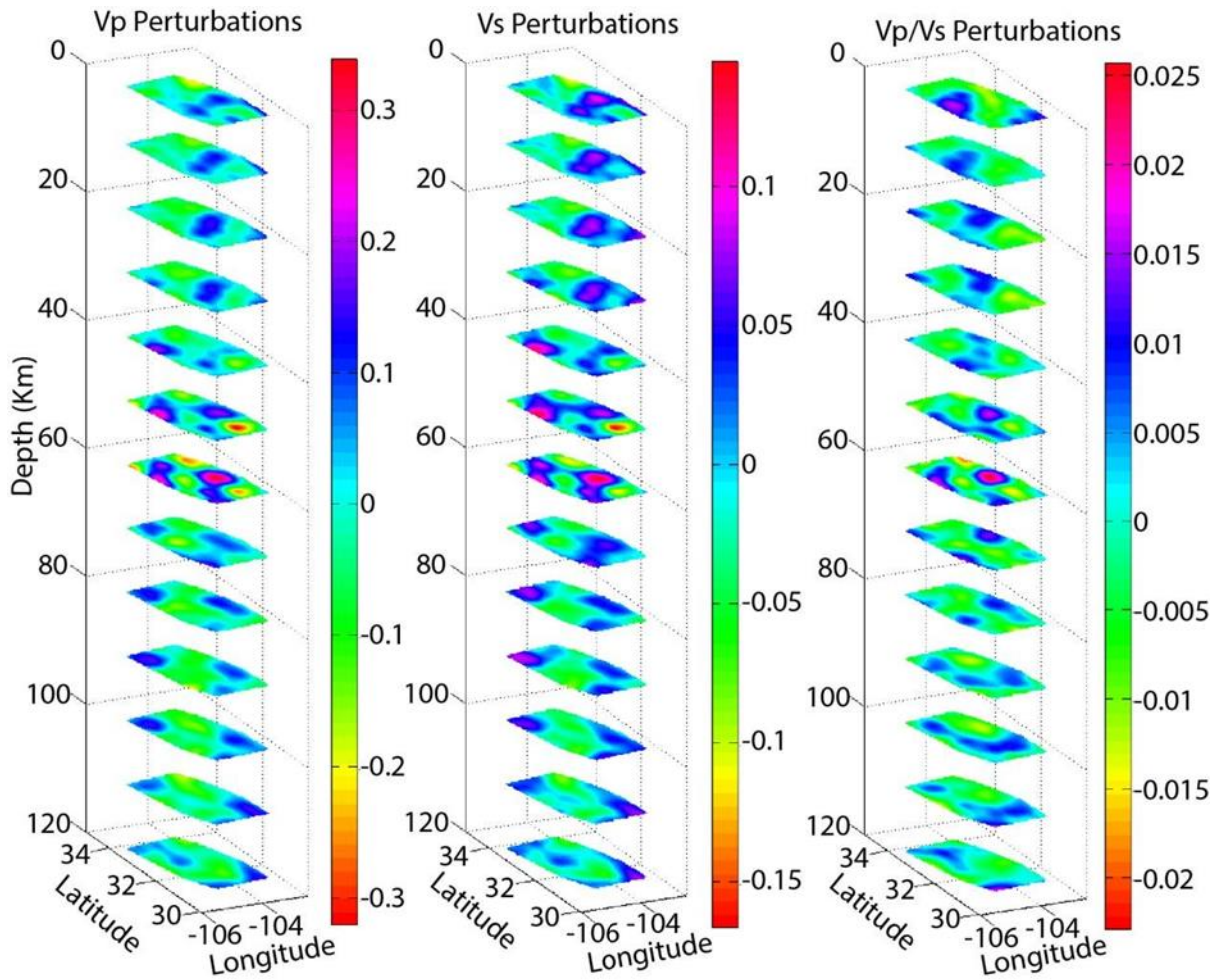


Figure 4.7. 3D Vp, Vs and Vp/Vs perturbations interpolated from 1D Vs and Vp (calculated from Poisson's ratio and shear wave velocity) models computed for each station. See text for further details.

*Step 4. CCP stack Ps and Sp receiver functions.* We stack Ps and Sp receiver functions using a Common Conversion Point (CCP) stacking method to increase signal-to-noise ratios [Dueker and Sheehan, 1997]. The technique we use is a back projection method in which receiver functions are raytraced through 3D P and S wave velocity models (generated in step 3) in order to place their conversions at correct positions laterally and in depth.

The common conversion point stacking method (CCP) uses the ideas of Common Mid-Point (CMP) stacking and migration in reflection seismology but instead of dealing with reflected waves, converted waves are stacked. First, time domain receiver functions are projected into the depth domain. It is assumed that every time point on the radial receiver function is produced by a primary conversion at a certain depth along the theoretical raypath. The depth is determined using the time delay of receiver function amplitudes with respect to the direct P (or direct S in case of Sp receiver functions), each receiver function's ray parameter, and the velocity models found in Step 2. After migration, the crustal volume is divided into bins of designated size and all amplitudes in the same bin are stacked to produce a structural image. The image delineates various interfaces, including the crust-mantle interface (Moho), which is usually marked by the largest impedance contrast. In our study, subsurface image points (or "bins") are spaced 10 km apart laterally for both Ps and Sp receiver functions.

Some of the energy in the radial receiver functions is produced by multiple P-to-S conversions (or multiple S-to-P conversions for Sp receiver functions); this energy will be mapped to deeper locations by the migration. But multiples tend to be less coherent than the primary conversion because of their extra reflections at the surface and longer paths in the heterogeneous shallow crust. When stacking many receiver functions from different events and receivers, multiples and noise are suppressed relative to primary conversions, which are enhanced. Therefore, a key to successful CCP stacking is having an array of densely-distributed stations and a good azimuthal distribution of earthquakes. The SIEDCAR/TA station distribution and the high data quality that characterize these stations meet these requirements.

## *Results*

We use Ps CCP images to examine the depths of major crustal discontinuities, and Sp CCP images to investigate major features in the mantle. Figures 8 and 9 show the CCP-stacked and migrated Ps (left vertical panel) and Sp (right vertical panel) receiver function images for the SIEDCAR region up to 200 km depth. Events with positive polarities (blue or purple on Ps and blue on Sp cross-sections) mark depths at which seismic velocity increases abruptly with increasing depth; events with negative polarities (red or yellow on Ps and red on Sp CCP images) mark abrupt velocity decreases as a function of depth. The largest positive-amplitude feature in Ps CCP images, indicating a velocity increase with depth, corresponds to the Moho, while the largest negative amplitude feature, indicating a velocity decrease with depth, we interpret to mark the LAB. The event interpreted to be the Moho in the Ps images is consistent with the Moho event found in Sp images (Figure 8 and 9). This suggests that our P- and S-velocity models are consistent with each other.

Figure 8 represents CCP results for N-S profiles A-A', B-B' and C-C'. On profile A-A', the depth of the positive (blue) event we believe to be the Moho ranges from ~40 km, in the south, to ~35 km, in the north, reaching a maximum depth of ~50 km at latitude 32.5°, roughly where the profile crosses the boundary of the Rio Grande Rift. The Moho is generally shallower in the northern part of the profile and deeper in the southern portion. The corresponding Sp CCP image indicates that the LAB ranges from ~80 km to ~98 km with very weak Sp signals in the latitude range 31.5° to 32.6°. The southern part of profile B-B' crosses the Delaware Basin, where strong Ps conversions show the Moho at ~50 km depth; the Moho shallows to ~40 km depth at the northern end

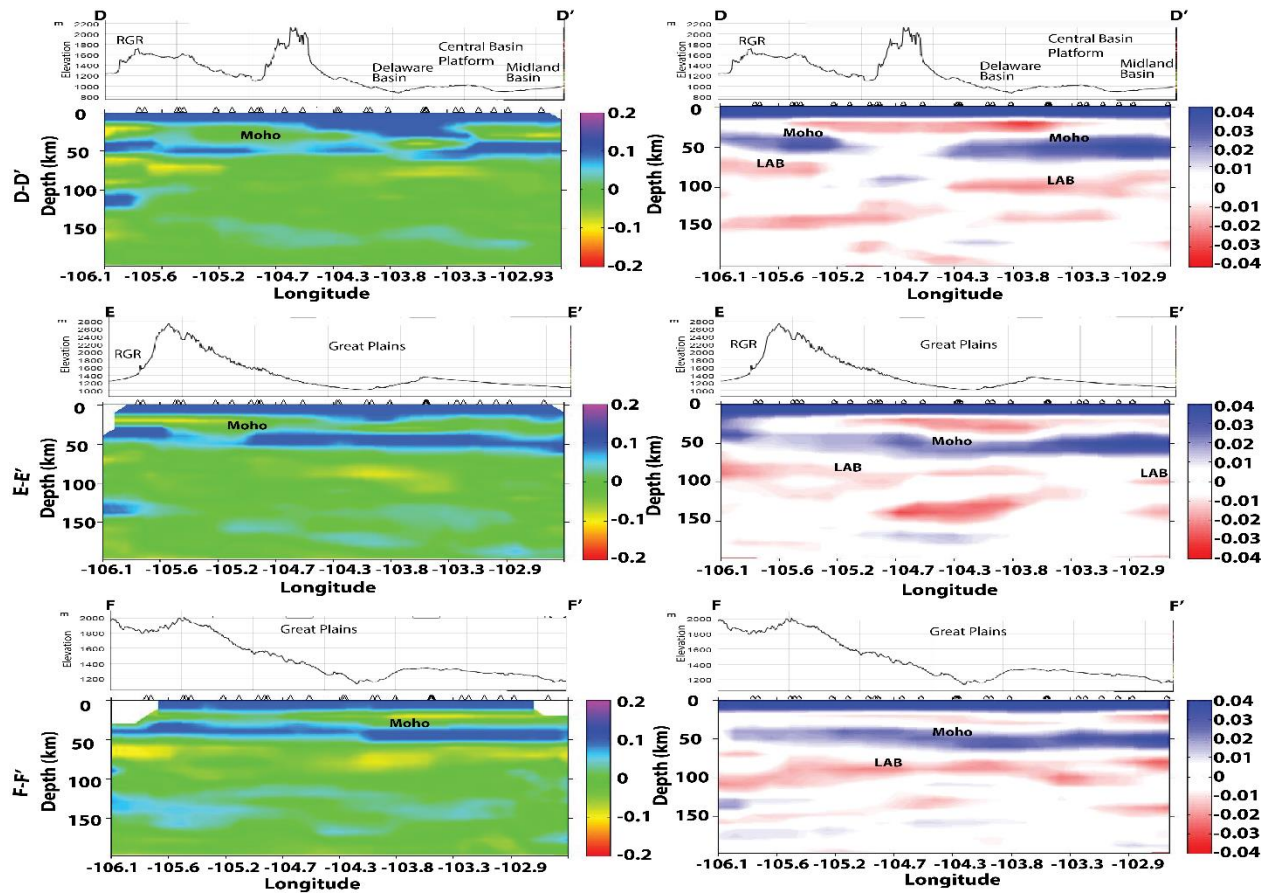


Figure 4.8. (left) Cross-sections of the  $P_s$  receiver function CCP image along south-north profiles (locations of profiles are shown in Figure 1). Purple and blue colors denote increases in velocity with depth; reds and yellows indicate velocity decreases with depth. Crustal thickness ranges from 38 km to 50 km from south to north. (right) Cross-sections of  $S_p$  receiver function CCP image along south-north profiles. Blue colors denote increases in velocity with depth; red colors indicate velocity decreases with depth. Depth to the LAB varies from  $\sim 80$  to  $\sim 110$  km beneath the study area and is either missing or displaced downward in the southern part of the area.

of the profile. The LAB mirrors the trend of the Moho:  $\sim 100$  km depth in the south and  $\sim 80$  km depth in the north, but it shows a significant gap between latitudes  $32.0^\circ$  and  $32.9^\circ$ . The southernmost portion of profile C-C' lies within the Delaware Basin, where the Moho event is muddled in the  $P_s$  image, crossing to the Central Basin Platform at  $\sim 32.0^\circ$ , where the Moho becomes clearer at  $\sim 55$  km depth. The Moho then shallows gradually to the north, reaching  $\sim 40$  km at latitude  $34.5^\circ$ .

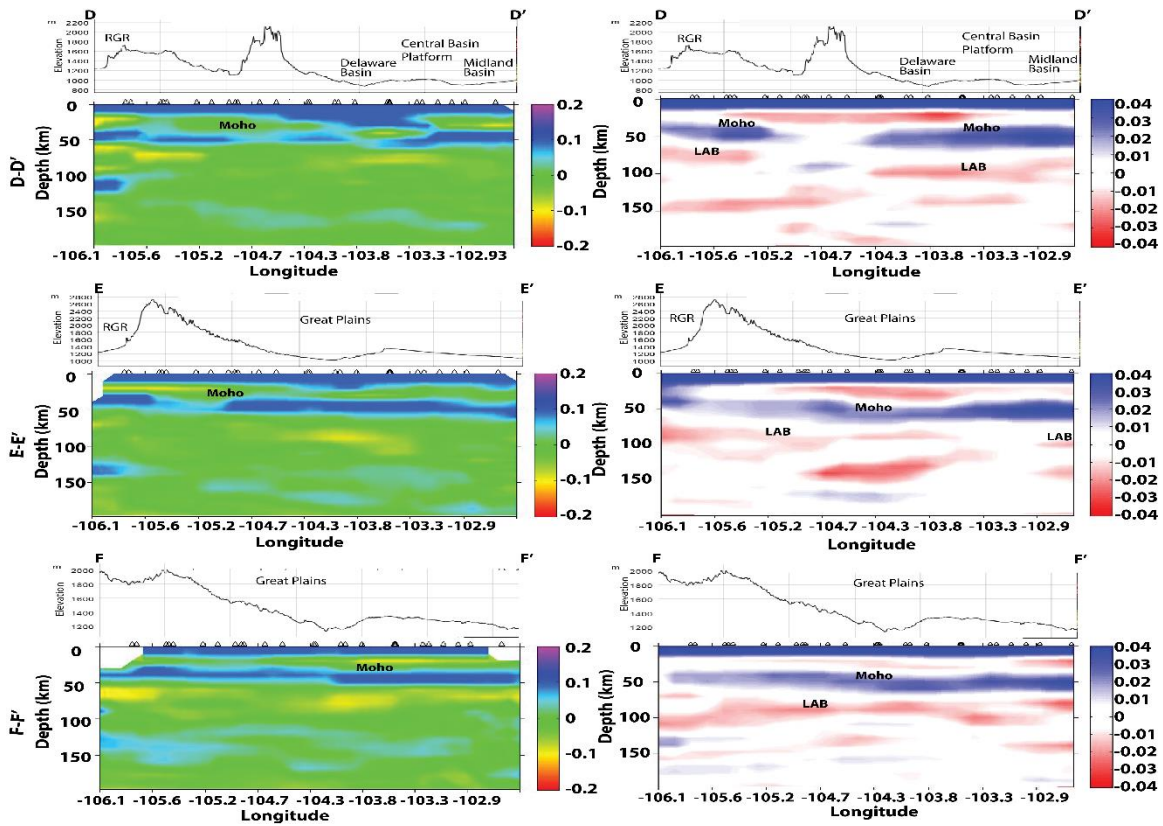


Figure 4.9. (left panel) Cross-sections of the Ps receiver function CCP image along west-east profiles (locations of profiles are shown in Figure 1). Purple and blue colors denote increases in velocity with depth; reds and yellows indicate velocity decreases with depth. Crustal thickness ranges from 42 km to 54 km from west to east. (right) Cross-sections of Sp receiver function CCP image along south-north profiles. Blue colors denote increases in velocity with depth; red colors indicate velocity decreases with depth. A gap in the LAB appears in the southernmost profile (D-D') between longitudes  $-105.4^{\circ}$  and  $104.3^{\circ}$ .

The Sp profile shows the LAB to be less distinct in the south,  $\sim 80$  km deep at latitude  $31.1^{\circ}$ , diving to a maximum of  $\sim 120$  km at latitude  $32.5^{\circ}$  before shallowing to  $\sim 100$  km depth at the profile's northern end.

In the west-east profile D-D' (Figure 9), the Ps CCP image shows that the Moho ranges from  $\sim 40$  km to  $\sim 45$  km. Moho conversions are weak from longitudes  $-105.2^{\circ}$  to  $-104.5^{\circ}$  (beneath the Delaware Basin) and the corresponding Sp CCP image confirms the weakness of the Moho feature there. LAB depths range from  $\sim 75$  km, in the west, to a

maximum depth of 100 km beneath the Central Basin Platform. There is once again a significant gap in the LAB beneath the Delaware Basin (longitudes  $-105.2^{\circ}$  to  $-104.3^{\circ}$ ) as in profile D-D' ( $-105.2^{\circ}$  to  $-104.5^{\circ}$ ) and the LAB also appears bifurcated and weak beneath the Midland Basin, to the east. The region in which the Moho and LAB are weak also has relatively higher topography compared to areas in which the Moho and LAB are intact (Figure 9, D-D'). We generated "hit count" plots for both Ps and Sp CCP stacked images of profile D-D' to evaluate the reliability of features (e.g., the LAB gap). "Hit counts" represent ray coverage of the subsurface by receiver functions (Figure 10). Ray coverage is quite good along most of the profile, including the area (hit counts of more than 150) where there a significant gap in the LAB appears between longitudes  $-105.2^{\circ}$  to  $-104.5^{\circ}$  at latitude  $32^{\circ}$ . It suggests that the observation of a gap in the LAB is reliable and that a process of lithospheric removal has occurred, or is perhaps underway.

Approximately 100 km north of profile D-D', on profile E-E', the Moho event appears at  $\sim 40$  km depth in the west and increases to  $\sim 50$  km depth in the east (Figure 9, profile E-E'), which matches the Moho depths on profile D-D'. The Moho event here is weak between longitudes  $-105.6^{\circ}$  to  $-105.1^{\circ}$ , further to the west (and closer to the rift) than in profile D-D' but it also occurs beneath a region of high surface topography, as in profile D-D'. On the corresponding Sp CCP image, LAB depth ranges from  $\sim 85$  km to  $\sim 100$  km and conversions are weak between longitudes  $-104.2^{\circ}$  and  $-102.9^{\circ}$ . In contrast to the Moho gap, the gap in the LAB has shifted from west to east (compare profiles D-D' and E-E'). The LAB gaps in profiles D-D' and E-E' occur above an elongated high-velocity anomaly found in travel time tomography that extends to  $\sim 400$  km depth just to the west of, and distinct from, the Great Plains [Pulliam *et al.*, *in prep.*, 2016]. Further to

the north, the Ps CCP image for profile F-F' indicates that the Moho varies only gradually, from ~38 km in the west to ~40 km in the east. The Sp CCP image for profile F-F' indicates that the LAB is intact across the profile and ranges from 110 km depth (in the west) to 90 km depth (in the east). This is the opposite of the trends for the LAB shown in profiles D-D' and E-E' but those profiles both included portions of the RGR while FF' samples only the Great Plains.

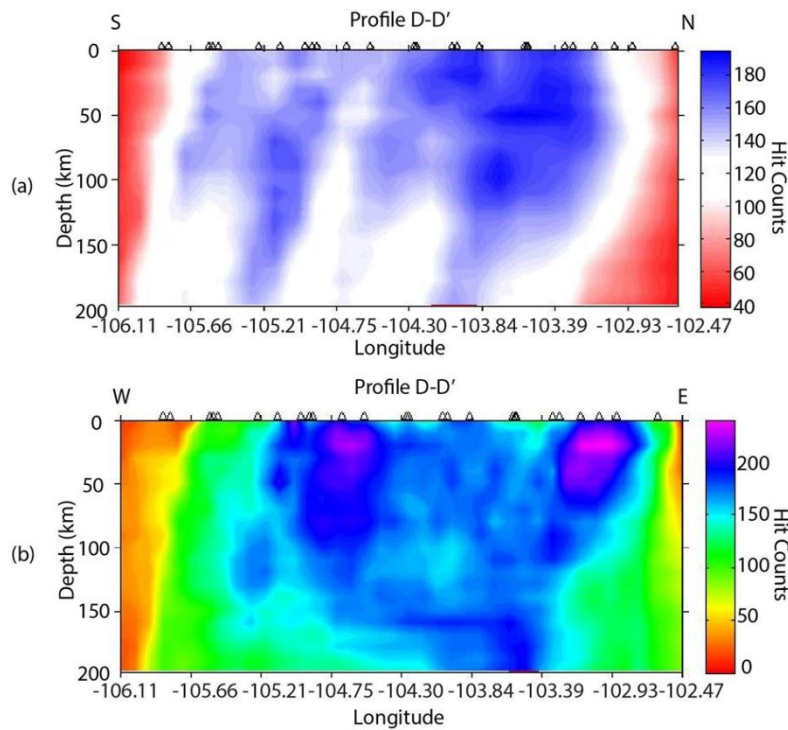


Figure 4.10. The “hit count” associated with the Ps receiver function’s (Figure 10a) and Sp receiver function’s (Figure 10b) CCP stack. The “hit count” represents P- and S-wave ray coverage beneath the profile D-D’ for Ps and Sp receiver functions, respectively (Figure 10a and 10b). The correlation of gap in LAB (Figure 9, profile D-D’) in an area of high hit count (or ray coverage), both in Ps and Sp receiver functions, which implies a reliable result, with a large fast anomaly in the upper mantle suggests that a more dramatic process of lithospheric removal has occurred, or is perhaps underway.

Figure 11 displays the interpolated Moho and LAB depths in the study region from Ps and Sp receiver functions, respectively. The Moho is relatively deeper in the

eastern region (50-54 km beneath the Great Plains) than in the western region (36-42 km beneath the RGR). Our CCP images (Figure 8 and 9) show strong Sp conversions, at depths of 102 -112 km, in the east whereas in the west Sp conversions are detected at depths of 75-100 km. We interpret this event to be the seismically-defined LAB. Its depths follow the general pattern of Moho depths, although LAB topography is more complex. A shallower LAB in the RGR than the Great Plains agrees well with the results of *Lekic and Fischer* [2014] using Sp receiver functions.

*Levander et al.* [2011] determined discontinuity structure beneath the Colorado plateau and its surroundings using Ps and Sp receiver functions. Their Ps receiver function results also show an LAB that is shallower beneath the RGR than in the surrounding area. They found the LAB at depths of ~70-80 km beneath western portion of profiles D-D' and E-E', which lies within the RGR. We find the thickest crust and deepest LAB in areas located just away from the eastern side of the RGR on the Delaware Basin. We find the thickest crust in approximately the same location as the deepest LAB (Figure 11, between  $-105.5^{\circ}$  to  $-104^{\circ}$  and  $31.5^{\circ}$  to  $32.5^{\circ}$ ).

### *Discussion*

Using Sp receiver functions, *Levander and Miller* [2012] found relatively thin lithosphere (LAB at 65-75 km depth) beneath the Basin and Range and thicker lithosphere beneath the Great Plains, where the LAB reaches depths of ~100 km. Our study area represents a location at which lithosphere transitions from the Basin and Range to the Great Plains; our results indicate that the transition of the LAB between these two provinces is not smooth. Ps results show that the Moho varies throughout the region in the range 36-54 km depth, while Sp results show that the LAB varies over

depths of 75-112 km. Both boundaries occur at generally shallower depths in the west and deeper depths in the east. Given the substantial extension and magmatic activity that the Basin and Range and southern Rio Grande Rift experienced since the Miocene [McQuarrie and Wernicke, 2005; Morgan et al., 1986], the shallow LAB observed in the northwestern part of our study area, which crosses (from west to east) from the southern edge of the RGR, at the eastern edge of the Great Basin and Range Province, to the Great Plains craton, is consistent with lithospheric thinning due to lateral extension. However, the correlation of a gap in the LAB in an area of high “hit count”, which implies a reliable result, with a large fast anomaly in the upper mantle suggests that a more dramatic process of lithospheric removal has occurred, or is perhaps underway (Figure 10). This gap also corresponds to high surface topography, which may be due to thermal uplift after a detached lithospheric block has sunk into the mantle. We note that timing of the uplift is not well-constrained but clearly took place in conjunction with the evolution of the Rio Grande Rift.

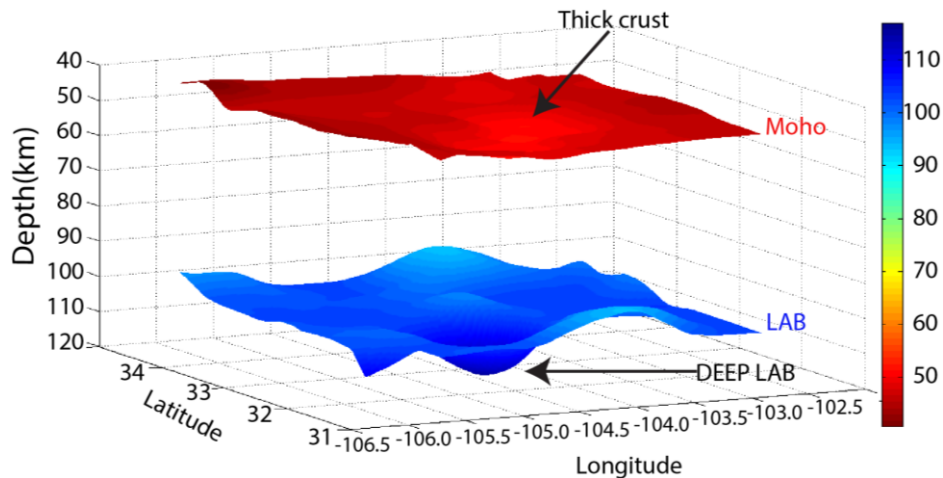


Figure 4.11. Figure 11 shows figure for Moho and LAB topography. Moho depth ranges from 36 km to 54 km (from west to east); LAB depth varies from 75 km to 112 km. Although the LAB has more complex topography than the Moho, it is also generally shallower in the west and deeper in the east.

We are not the first to find thickened crust above a mantle anomaly in this region. Using receiver function analysis, *Wilson et al.* [2005] found thickened crust in the region nearly above a feature they interpreted to be a downwelling. Data used in that study were recorded by a linear array (“La Ristra”), which did not admit 3D processing, so the lateral extent of the anomaly could not be constrained. SIEDCAR and TA data revealed that the fast anomaly extends as far south as the Big Bend region of Texas (Figure 2) but only 50-75 km further north of the La Ristra line (roughly latitude 33.5°N). The RGR becomes a diffuse feature at its southern end, where its bounds are quite uncertain, while its limits are much clearer in the north. The anomaly extends over more than 200 km in the south (from longitude -103.5 to -105.5 at latitude 30.0°) but less than 100 km in the north (longitude -104.0 to -104.5 at latitude 33.0°). If the anomaly represents a block of lithosphere that has become detached and is sinking into the mantle, it makes sense the block would be larger in the south, which has undergone greater extension, than in the north. If the data were available, one would presumably find a large gap in the LAB in the Big Bend region of west Texas, as we discovered in southeastern New Mexico. The sparseness of the Transportable Array’s (TA) station spacing (~70 km) does not allow “velocity analysis” cross-correlation procedure to be applied there.

Using TA data, *Sosa et al.* [2014] performed a 1D joint inversion of receiver functions and surface wave dispersion and generated 3D shear wave velocity images of the subsurface to a depth of 300 km. They also imaged a low velocity zone that first appears beneath the RGR and extends to the west, beneath the Basin and Range and Colorado Plateau. *Lekic and Fisher* [2014] used an optimized deconvolution technique based on the extended-time multi-taper method to image variations in Moho, LAB and

mid-lithospheric discontinuities beneath the western United States. They detected strong Sp conversions across a relatively shallow (60-80 km) seismically defined LAB beneath the areas that have undergone substantial extension, including the Great Basin, the southern Basin and Range province, and the southern RGR. Modeling surface wave phase velocity dispersion, *West [2004]* found a transition in lithosphere thickness from 200 km beneath the Great Plains to 45-55 km beneath the RGR (thickening to 120-150 km beneath the Colorado Plateau). While this matches the trend we see, our values differ significantly. Our Sp CCP stacking results suggest an LAB depth of 75 km-85 km beneath the southern portion of the RGR, which has seen a greater amount of thinning and extension than the northern portion, and LAB depths of 100-115 km beneath the westernmost portion of the Great Plains.

Our observations for the eastern flank of the RGR are similar to model predictions of *Stern et al. [2013]*, which were made for a model that included an abrupt step in the lithosphere (although the step occurred across a transform fault, not a rift). In the RGR we also find a region of relatively thin crust adjacent to thicker crust (the Great Plains) and thickened crust overlying a high velocity anomaly in the mantle, as do they. Their model predicts that a surface depression above the downwelling will migrate with time, which might be the case for the RGR. As noted above, the southern portion of the RGR has undergone significantly more extension than the northern portion and the rift itself appears to be propagating northward. Progressively more northerly cross-sections, such as D-D', E-E', and F-F', may therefore represent a time progression, and the LAB gap in D-D' is offset to the east of the gap found in E-E'. F-F', which presumably represents the "youngest" slice of rifting process (and has undergone the least extension) does not show

a gap at all. Note that the high surface topography follows the LAB gap in each profile. We propose that a process similar to the one described by *Stern et al.* [2013] is occurring beneath the eastern flank of the Rio Grande Rift.

### *Conclusion*

We processed and interpreted Ps and Sp CCP images from earthquake data recorded by SIEDCAR and Transportable Array stations using a novel technique for receiver function processing. We constructed 3D shear and compressional velocity models for use in migrating CCP stacks of receiver functions in which we optimized the average correlation values of common receiver gathers for target features while perturbing shear wave velocities in a process driven by simulated annealing. The technique simultaneously finds depths to major discontinuities (in this case the Moho and LAB) and S velocity profiles beneath each seismic station in a manner that is similar to velocity analysis in reflection seismology.

Ps CCP results show that the Moho ranges throughout the region from 36-54 km, while Sp CCP results show variations in the LAB of 75-112 km. We find that a depression in the Moho overlies a region in which the LAB is largely missing. We speculate that the missing LAB and depressed Moho are the result of large-scale removal of the lower lithosphere, which has essentially erased the impedance contrast that produces Sp-wave conversions, and produced a large fast anomaly in the upper mantle beneath the LAB gap. We further speculate that, because the anomaly is larger to the south, in the west Texas/Big Bend region, the gap in the LAB is likely to be larger in that location than in the study region shown in Figure 2.

### *Acknowledgments*

We thank S. Hansen and K. Dueker for the use of their receiver function imaging software, which formed the basis of our CCP stacking, Reetam Biswas, who contributed to the development of the receiver function imaging technique, and Yu Xia. We thank the Incorporated Research Institutions of Seismology (IRIS) and EarthScope for their roles in acquiring, archiving, and disseminating the broadband seismic data used in this study. All data were contributed to, and are available at, the IRIS Data Management Center (<http://ds.iris.edu/>). This research was supported by the National Science Foundation (EAR-0746321) and the W.M. Keck Foundation.

## References

- Aarts, E., Korst, J., 1989. Simulated annealing and Boltzmann machines: a stochastic approach to combinatorial optimization and neural computing.
- Agrawal, M., Pulliam, J., Sen, M.K., Dutta, U., Pasyanos, M.E., Mellors, R., 2015. Crustal and uppermost mantle structure in the Middle East: assessing constraints provided by jointly modelling Ps and Sp receiver functions and Rayleigh wave group velocity dispersion curves. *Geophys. J. Int.* 201, 783–810. doi:10.1093/gji/ggv050
- Agrawal, M., Pulliam, J., Sen, M.K., Gurrola, H., 2015. Lithospheric structure of the Texas-Gulf of Mexico passive margin from surface wave dispersion and migrated Ps receiver functions. *Geochemistry, Geophys. Geosystems* 16, 2221–2239. doi:10.1002/2015GC005803
- Ammon, C.J., Randall, G.E., Zandt, G., 1990. On the nonuniqueness of receiver function inversions. *J. Geophys. Res.* 95, 15303. doi:10.1029/JB095iB10p15303.
- Averill, M.G., 2007. A lithospheric investigation of the Southern Rio Grande Rift. ETD Collect. Univ. Texas, El Paso.
- Baldrige, W.S., Perry, F.V., Vaniman, D.T., Nealey, L.D., Leavy, B.D., Laughlin, A.W., Kyle, P., Bartov, Y., Steinitz, G., Gladney, E.S., 1991. Middle to late cenozoic magmatism of the southeastern Colorado plateau and central Rio Grande rift (New Mexico and Arizona, U.S.A.): a model for continental rifting. *Tectonophysics* 197, 327–354. doi:10.1016/0040-1951(91)90049-X
- Berglund, H.T., Sheehan, A.F., Murray, M.H., Roy, M., Lowry, A.R., Nerem, R.S., Blume, F., 2011. Distributed deformation across the Rio Grande Rift, Great Plains, and Colorado Plateau. *Geology* 40, 23–26. doi:10.1130/G32418.1
- Çakır, Ö., Erduran, M., 2004. Constraining crustal and uppermost mantle structure beneath station TBZ (Trabzon, Turkey) by receiver function and dispersion analyses. *Geophys. J. Int.* 158, 955–971. doi:10.1111/j.1365-246X.2004.02345.x
- Chase, C.G., Libarkin, J.A., Sussman, A.J., 2002. Colorado Plateau: Geoid and Means of Isostatic Support. *Int. Geol. Rev.* 44, 575–587. doi:10.2747/0020-6814.44.7.575.
- Dueker, K.G., Sheehan, A.F., 1997. Mantle discontinuity structure from midpoint stacks of converted P to S waves across the Yellowstone hotspot track. *J. Geophys. Res.* 102, 8313. doi:10.1029/96JB03857
- Dugda, M.T., Nyblade, A.A., 2006. New constraints on crustal structure in eastern Afar from the analysis of receiver functions and surface wave dispersion in Djibouti. *Geol. Soc. London, Spec. Publ.* 259, 239–251. doi:10.1144/GSL.SP.2006.259.01.19

- Evanzia, D., Pulliam, J., Ainsworth, R., Gurrola, H., Pratt, K., 2014. Seismic Vp & Vs tomography of Texas & Oklahoma with a focus on the Gulf Coast margin. *Earth Planet. Sci. Lett.* 402, 148–156. doi:10.1016/j.epsl.2013.12.027.
- Faber, S., Muller, G., 1980. Sp phases from the transition zone between the upper and lower mantle. *Bull. Seismol. Soc. Am.* 70, 487–508.
- Farra, V., Vinnik, L., 2000. Upper mantle stratification by P and S receiver functions. *Geophys. J. Int.* 141, 699–712. doi:10.1046/j.1365-246x.2000.00118.x
- Frederiksen, A. W.; Bostock, M. G., 2000. Modelling teleseismic waves in dipping anisotropic structures. *Geophys. J. Int.* vol. 141 (2) p. 401-412.
- Gao, W., 2004. Upper mantle convection beneath the central Rio Grande rift imaged by P and S wave tomography. *J. Geophys. Res.* 109, B03305. doi:10.1029/2003JB002743
- Geman, S., Geman, D., 1984. Stochastic Relaxation, Gibbs Distributions, and the Bayesian Restoration of Images. *IEEE Trans. Pattern Anal. Mach. Intell. PAMI-6*, 721–741. doi:10.1109/TPAMI.1984.4767596.
- Jesse F. Lawrence, D.A.W., n.d. Combined receiver-function and surface wave phase-velocity inversion using a niching genetic algorithm: Application to Patagonia.
- Julià, J., Ammon, C.J., Herrmann, R.B., Correig, A.M., 2000. Joint inversion of receiver function and surface wave dispersion observations. *Geophys. J. Int.* 143, 99–112. doi:10.1046/j.1365246x.2000.00217.x
- Julià, J., Ammon, C.J., Nyblade, A.A., 2005. Evidence for mafic lower crust in Tanzania, East Africa, from joint inversion of receiver functions and Rayleigh wave dispersion velocities. *Geophys. J. Int.* 162, 555–569. doi:10.1111/j.1365-246X.2005.02685.x
- Keller, G.R., 1999. The Rio Grande rift: A geological and geophysical overview. *Rocky Mt. Geol.* 34, 121–130. doi:10.2113/34.1.121.
- Kikuchi, M., Kanamori, H., 1982. Inversion of complex body waves. *Bull. Seismol. Soc. Am.* 72, 491–506.
- Kind, R., Vinnik, L.P., 1988. The upper- mantle discontinuities underneath the GRF array from P- to -S converted phases. *J. Geophys. - Zeitschrift fur Geophys.*
- King, S.D., 2007. Hotspots and edge-driven convection. *Geology* 35, 223. doi:10.1130/G23291A.1
- Kirkpatrick, S., Gelatt, C.D., Vecchi, M.P., 1983. Optimization by simulated annealing. *Science* 220, 671–80. doi:10.1126/science.220.4598.671
- Kreemer, C., Blewitt, G., Bennett, R.A., 2010. Present-day motion and deformation of the Colorado Plateau. *Geophys. Res. Lett.* 37, n/a–n/a. doi:10.1029/2010GL043374.

- Kumar, P., 2005. The lithosphere-asthenosphere boundary in the Tien Shan-Karakoram region from *S* receiver functions: Evidence for continental subduction. *Geophys. Res. Lett.* 32, L07305. doi:10.1029/2004GL022291.
- Kumar, P., Kind, R., Hanka, W., Wylegalla, K., Reigber, C., Yuan, X., Woelbern, I., Schwintzer, P., Fleming, K., Dahl-Jensen, T., Larsen, T.B., Schweitzer, J., Priestley, K., Gudmundsson, O., Wolf, D., 2005. The lithosphere–asthenosphere boundary in the North-West Atlantic region. *Earth Planet. Sci. Lett.* 236, 249–257. doi:10.1016/j.epsl.2005.05.029.
- Lekić, V., Fischer, K.M., 2014. Contrasting lithospheric signatures across the western United States revealed by *Sp* receiver functions. *Earth Planet. Sci. Lett.* 402, 90–98. doi:10.1016/j.epsl.2013.11.026
- Li, X., Kind, R., Yuan, X., Wölbern, I., Hanka, W., 2004. Rejuvenation of the lithosphere by the Hawaiian plume. *Nature* 427, 827–9. doi:10.1038/nature02349.
- Li, X., Sobolev, S.V., Kind, R., Yuan, X., Estabrook, C., 2000. A detailed receiver function image of the upper mantle discontinuities in the Japan subduction zone. *Earth Planet. Sci. Lett.* 183, 527– 541. doi:10.1016/S0012-821X(00)00294-6
- Ligorria, J.P., Ammon, C.J., 1999. Iterative deconvolution and receiver-function estimation. *Bull. Seismol. Soc. Am.* 89, 1395–1400.
- McQuarrie, N., Wernicke, B.P., 2005. An animated tectonic reconstruction of southwestern North America since 36 Ma. *Geosphere* 1, 147–172. doi:10.1130/GES00016.1.
- Morgan, P., Seager, W.R., Golombek, M.P., 1986. Cenozoic thermal, mechanical and tectonic evolution of the Rio Grande Rift. *J. Geophys. Res.* 91, 6263. doi:10.1029/JB091iB06p06263
- Morgan, P., Swanberg, C.A., 1985. On the Cenozoic uplift and tectonic stability of the Colorado Plateau. *J. Geodyn.* 3, 39–63. doi:10.1016/0264-3707(85)90021-3.
- Moucha, R., Forte, A.M., Rowley, D.B., Mitrovica, J.X., Simmons, N.A., Grand, S.P., 2008. Mantle convection and the recent evolution of the Colorado Plateau and the Rio Grande Rift valley. *Geology* 36.
- Owens, T.J., Nyblade, A.A., Gurrola, H., Langston, C.A., 2000. Mantle transition zone structure beneath Tanzania, east Africa. *Geophys. Res. Lett.* 27, 827–830. doi:10.1029/1999GL005429
- Ozalaybey, S., Savage, M.K., Sheehan, A.F., Louie, J.N., Brune, J.N., 1997. Shear-wave velocity structure in the northern Basin and Range province from the combined analysis of receiver functions and surface waves. *Bull. Seismol. Soc. Am.* 87, 183–199.

- Parsons, T.E., 1995. The basin and range province: Chapter 7 277–324.
- Pasyanos, M.E., 2005. A variable resolution surface wave dispersion study of Eurasia, North Africa, and surrounding regions. *J. Geophys. Res.* 110, B12301. doi:10.1029/2005JB003749.
- Roger Buck, W., 1986. Small-scale convection induced by passive rifting: the cause for uplift of rift shoulders. *Earth Planet. Sci. Lett.* 77, 362–372. doi:10.1016/0012-821X(86)90146-9
- Roy, M., MacCarthy, J.K., Selverstone, J., 2005. Upper mantle structure beneath the eastern Colorado Plateau and Rio Grande rift revealed by Bouguer gravity, seismic velocities, and xenolith data. *Geochemistry, Geophys. Geosystems* 6, n/a–n/a. doi:10.1029/2005GC001008.
- Sahagian, D., Proussevitch, A., Carlson, W., 2002. Timing of Colorado Plateau uplift: Initial constraints from vesicular basalt-derived paleoelevations. *Geology* 30, 807–810. doi:10.1130/00917613(2002)030
- Sen, M.K., Stoffa, P.L., 1995. *Global Optimization Methods in Geophysical Inversion*. Elsevier.
- Stern, T., Houseman, G., Salmon, M., Evans, L., 2013. Instability of a lithospheric step beneath western North Island, New Zealand. *Geology* 41, 423–426. doi:10.1130/G34028.1.
- Tkalčić, H., Pasyanos, M.E., Rodgers, A.J., Gök, R., Walter, W.R., Al-Amri, A., 2006. A multistep approach for joint modeling of surface wave dispersion and teleseismic receiver functions: Implications for lithospheric structure of the Arabian Peninsula. *J. Geophys. Res.* 111, B11311. doi:10.1029/2005JB004130.
- Van Wijk, J., van Hunen, J., Goes, S., 2008. Small-scale convection during continental rifting: Evidence from the Rio Grande rift. *Geology* 36, 575. doi:10.1130/G24691A.1.
- Van Wijk, J.W., Baldrige, W.S., van Hunen, J., Goes, S., Aster, R., Coblenz, D.D., Grand, S.P., Ni, J., 2010. Small-scale convection at the edge of the Colorado Plateau: Implications for topography, magmatism, and evolution of Proterozoic lithosphere. *Geology* 38, 611–614. doi:10.1130/G31031.1
- Varela, C.L., Stoffa, P.L., Sen, M.K., 1998. Background velocity estimation using non-linear optimization for reflection tomography and migration misfit. *Geophysical Prospecting* 46, Issue 1, 51-78.
- West, M., 2004. Crust and upper mantle shear wave structure of the southwest United States: Implications for rifting and support for high elevation. *J. Geophys. Res.* 109, B03309. doi:10.1029/2003JB002575

- Wilson, D., 2005a. Imaging the seismic structure of the crust and upper mantle beneath the Great Plains, Rio Grande Rift, and Colorado Plateau using receiver functions. *J. Geophys. Res.* 110, B05306. doi:10.1029/2004JB003492
- Wilson, D., 2005b. Seismic imaging of the crust and upper mantle using regularized joint receiver functions, frequency–wave number filtering, and multimode Kirchhoff migration. *J. Geophys. Res.* 110, B05305. doi:10.1029/2004JB003430
- Wilson, D.C., Angus, D.A., Ni, J.F., Grand, S.P., 2006. Constraints on the interpretation of S -to- P receiver functions. *Geophys. J. Int.* 165, 969–980. doi:10.1111/j.1365-246X.2006.02981.x
- Woodward, L.A., 1977. Rate of crustal extension across the Rio Grande Rift near Albuquerque, New Mexico. *Geology* 5, 269–272. doi:10.1130/0091-7613(1977)5.
- Yuan, X., Kind, R., Li, X., Wang, R., 2006. The S receiver functions: synthetics and data example. *Geophys. J. Int.* 165, 555–564. doi:10.1111/j.1365-246X.2006.02885.x
- Zhu, L., Kanamori, H., 2000. Moho depth variation in southern California from teleseismic receiver functions. *J. Geophys. Res.* 105, 2969. doi:10.1029/1999JB900322

## CHAPTER FIVE

### Conclusions

We demonstrated the usefulness of MOOS by jointly modeling Ps and Sp receiver functions and Rayleigh wave group velocity dispersion curves and by quantitatively assessing the uncertainties associated with, and independence of, model parameters. These statistical assessment tools (the PPD and model parameter correlation matrix) can identify characteristics of acceptable models that are *required by* the data, rather than those that are simply *consistent with* the data.

We also demonstrated that joint fitting Ps and Sp receiver functions and Rayleigh wave group velocity dispersion curves provides better constraints on model parameters than does a single functional. We apply this newly-developed technique to earthquake data recorded by eleven seismic stations in the Middle East. Our results show that crustal thickness varies in the region from ~15 km beneath ATD, located in Djibouti, to ~45 km beneath RAYN, in Saudi Arabia.

Our second project was an application of a technique derived from MOOS to the Texas Gulf Coastal Plain. The strategy was to a) find 1D seismic velocity models for a transect across the Plain, using ambient noise data recorded during a 2010-13 broadband seismograph deployment, b) compute P-to-S receiver functions, and c) migrate those receiver functions using the 1D velocity models found by fitting dispersion curves via VFSA. The results of seismic migration are quite sensitive to velocity models in the case

of substantial lateral velocity variations and no reliable models of the crust and upper mantle have been found previously in the passive margin of Texas Gulf coast.

Using surface wave dispersion measured from ambient noise is a new and exciting prospect because very few earthquakes occur in the region, so opportunities for traditional surface wave modeling are rare. Dispersion curves found by cross-correlating ambient noise were used to produce velocity models for migration of receiver functions. Apart from several advantages of this methodology, there is one drawback: ambient noise has significant amplitudes only at periods of 5-50 s, which only constrains subsurface velocities to depths of ~100 km. As discussed previously, because no reliable models of the crust and upper mantle had been found in the passive margin of Texas Gulf coast, determining a velocity model even up to 100 km depth should give us better migration results of Ps receiver functions. Our results indicate that the Moho is missing outboard of the Balcones Fault Zone (BFZ), suggesting that the BFZ is a significant, throughgoing feature that has introduced fluids to the upper mantle.

In our last research project, we processed and interpreted Ps and Sp CCP images from earthquake data recorded by SIEDCAR and Transportable Array stations using a novel technique for receiver function processing. We constructed 3D shear and compressional velocity models for use in migrating CCP stacks of receiver functions in which we optimized the average correlation value of common receiver gathers for target features while perturbing shear wave velocities in a process driven by simulated annealing. The technique simultaneously finds depths to major discontinuities (in this case the Moho and LAB) and S velocity profiles beneath each seismic station in a manner that is similar to velocity analysis in reflection seismology. Finding the correct depths of

these major discontinuities is important because the impedance contrast implied by observed Moho and LAB events can divert raypaths dramatically from their trajectories in a smooth structure, thereby degrading the quality and fidelity of resulting migration images. Our results show a gap in the seismically-determined lithosphere-asthenosphere boundary beneath the eastern flank of the Rio Grande Rift that we interpret, in conjunction with  $V_p$  and  $V_s$  tomography, to result from large-scale removal of the lithosphere.

### *Suggestions for Future Work*

The techniques we use to determine P- and S-velocity models for use in migrating receiver functions each have advantages and disadvantages. To produce a reliable model, the velocity analysis technique used in Chapter 4 must have accurate search bounds specified by the user. One must therefore provide a starting model. While the “ambient noise” technique, which also uses VFSA, also needs to have its search bounds specified, the periods at issue (those available in the ambient noise, typically 5-50 s) admit only relatively smooth models, so search bounds are more easily estimated and models can be parameterized more sparsely than with a technique that relies on body waves, as does the velocity analysis approach of Chapter 4.

A good approach, therefore, would be to formulate a two-step approach, one in which an initial, fairly smooth model is found by modeling surface wave dispersion curves (found by ambient noise cross-correlation or a classical two-station method, or both) and the model is then used to construct search bounds for velocity analysis based on receiver functions. A second approach would be to conduct both steps jointly.

## REFERENCES

- Agostinetti, N. P. & Malinverno, A., 2010. Receiver function inversion by trans-dimensional Monte Carlo sampling, *Geophys. J. Int.*, 181, 858–872.
- Al-Amri, A.M., 1998. The crustal structure of the western Arabian platform from the spectral analysis of long-period P-wave amplitude ratios, *Tectonophysics*, 136, 271–283.
- Al-Amri, A., 1999. The crustal and upper-mantle structure of the interior Arabian Platform. *Geophys. J. Int.*, 136, 421–430.
- Al-Damegh, K., Sandvol, E. & Barazangi, M., 2005. Crustal structure of the Arabian Plate: new constraints from the analysis of teleseismic receiver functions, *Earth planet. Sci. Lett.*, 231, 177–196.
- Al-Lazki, A., Seber, D., Sandvol, E., Turkelli, N., Mohamad, R. & Barazangi, M., 2003. Tomographic Pn velocity and anisotropy structure beneath the Anatolian plateau (eastern Turkey) and the surrounding regions, *Geophys. Res. Lett.*, 30, 8043, doi:10.1029/2003GL017391.
- Al-Lazki, A. I., Sandvol, E., Seber, D., Barazangi, M., Turkelli, N. & Mohamad, R., 2004. On tomographic imaging of mantle lid velocity and anisotropy at the junction of the Arabian, Eurasian and African Plates, *Geophys. J. Int.*, 158, 1024–1040, doi:10.1111/j.1365-246X.2004.02355.x.
- Al-Lazki, A.I., Seber, D., Sandvol, E. & Barazangi, M., 2002. A crustal transect across the Oman mountains of the eastern margin of Arabia, *GeoArabia*, 7, 47–78.
- Ammon, C.J., 1997. An overview of receiver function analysis.  
<http://eqseis.geosc.psu.edu/~cammon/HTML/RftnDocs/rftn01.html>
- Ammon, C.J., Herrmann, R.B., Pasyanos, M.E, Walter, W.R, Sevilla, W. & Randall, G., 2005. Simultaneous Inversion of Receiver Functions and Surface-Wave Dispersion Measurements for Lithospheric Structure beneath Asia and North Africa, *Proc. 27th Seismic Research Review: Ground-Based Nuclear Explosion Monitoring Technologies*, Palm Springs, CA, pp. 3-12.

- Ammon, C.J., Kosarian, M., Herrmann, R.B, Pasyanos, M.E., Walter, W.R. & Tkalčić, H., 2004. Simultaneous Inversion of Receiver Functions, Multi-mode Dispersion, and Travel-time Tomography for Lithospheric Structure Beneath the Middle East and North Africa, Proc. 26th Seismic Research Review - Trends in Nuclear Explosion Monitoring, Orlando, FL, pp. 17-28.
- Ammon, C.J., Randall, G.E. & Zandt, G., 1990. On the non-uniqueness of receiver function inversions, *J. Geophys. Res.*, 95: 15,303-15,318.
- Angus, D. A., Wilson, D.C., Sandvol, E. & Ni, J.F., 2006. Lithospheric structure of the Arabian and Eurasian collision zone in eastern Turkey from S-wave receiver functions, *Geophys. J. Int.*, 166, 1335–1346, doi:10.1111/j.1365-246X.2006.03070.x.
- Ainsworth, R., J. Pulliam, H. Gurrola, and D. Evanzia (2014), Sp receiver function imaging of a passive margin: transect across Texas's Gulf Coastal Plain, *Earth Planet. Sci. Lett.*, 402, 138-147.
- Ammon, C. J., M. Kosarian, and R. B. Hermann (2006), Simultaneous Inversion of Receiver Functions, Multi-mode Dispersion, and Travel-time Tomography for Lithospheric Structure Beneath the Middle East and North Africa. Defense Technical Information Center.
- Aarts, E., Korst, J., 1989. Simulated annealing and Boltzmann machines: a stochastic approach to combinatorial optimization and neural computing.
- Agrawal, M., Pulliam, J., Sen, M.K., Dutta, U., Pasyanos, M.E., Mellors, R., 2015. Crustal and uppermost mantle structure in the Middle East: assessing constraints provided by jointly modelling Ps and Sp receiver functions and Rayleigh wave group velocity dispersion curves. *Geophys. J. Int.* 201, 783–810. doi:10.1093/gji/ggv050
- Ammon, C.J., Randall, G.E., Zandt, G., 1990. On the nonuniqueness of receiver function inversions. *J. Geophys. Res.* 95, 15303. doi:10.1029/JB095iB10p15303.
- Averill, M.G., 2007. A lithospheric investigation of the Southern Rio Grande Rift. ETD Collect. Univ. Texas, El Paso.
- Baldrige, W.S., Perry, F.V., Vaniman, D.T., Nealey, L.D., Leavy, B.D., Laughlin, A.W., Kyle, P., Bartov, Y., Steinitz, G., Gladney, E.S., 1991. Middle to late cenozoic magmatism of the southeastern Colorado plateau and central Rio Grande rift (New Mexico and Arizona, U.S.A.) : a model for continental rifting. *Tectonophysics* 197, 327–354. doi:10.1016/0040-1951(91)90049-X
- Berglund, H.T., Sheehan, A.F., Murray, M.H., Roy, M., Lowry, A.R., Nerem, R.S., Blume, F., 2011. Distributed deformation across the Rio Grande Rift, Great Plains, and Colorado Plateau. *Geology* 40, 23–26. doi:10.1130/G32418.1

- Baig, A., M. Bostock, and J. P. Mercier (2005), Spectral reconstruction of teleseismic P Greens functions, *J. Geophys. Res. : Solid Earth* (1978-2012), 110.
- Bensen, G., M. Ritzwoller, M. Barmin, A. Levshin, F. Lin, and M. Moschetti (2007), Processing seismic ambient noise data to obtain reliable broad-band surface wave dispersion measurements, *Geophys. J. Int.*, 169, 1239-1260.
- Bird, D. E., K. Burke, S. A. Hall, and J. F. Casey (2005), Gulf of Mexico tectonic history: Hotspot tracks, crustal boundaries, and early salt distribution, *Am. Assoc. Pet. Geol. Bull.*, 89, 311-328.
- Blackwell, D., and M. Richards (2004), Geothermal map of North America, AAPG Map, scale 1:6,500,000, Product Code 423.
- Blackwell, D., M. Richards, and Z. Frone (2010), Texas Geothermal Assessment for the I35 Corridor East for Texas State Energy Conservation Office Contract CM709, Southern Methodist University.
- Boillot, G., G. Feraud, M. Recq, and J. Girardeau (1989), "Undercrusting" by serpentinite beneath rifted margins: The examples of the west Galicia margin (Spain), *Nature*, 341, 523-525.
- Bostock, M. (2004), Greens functions, source signatures, and the normalization of teleseismic wave fields, *J. Geophys. Res.: Solid Earth* (1978-2012), 109.
- Burke, K. (1988), Tectonic evolution of the Caribbean, *Annual Review of Earth Planet. Sci.*, 16, 201-230.
- Barazangi, M., Sandvol, E. & Seber, D., 2006. Structure and tectonic evolution of the Anatolian plateau in eastern Turkey, *GSA Today*, 409, 463–473.
- Blanc, E.J.P., Allen, M.B., Inger, S. & Hassani, H., 2003. Structural styles in the Zagros simple folded zone, Iran, *J. Struct. Geol.*, 160, 401–412.
- Bodin, T., Sambridge, M., Tkalčić, H., Arroucau, P., Gallagher, K. & Rawlinson, N., 2012. Transdimensional inversion of receiver functions and surface wave dispersion. *J. Geophys. Res.*, 117, B02301. doi:10.1029/2011JB008560.
- Bock, G., 1991. Long-period S to P converted waves and the onset of partial melting beneath Oahu, Hawaii, *Geophys. Res. Lett.*, 18, 869–872.
- Cakir, O. & Erduran, M., 2004. Constraining crustal and uppermost mantle structure beneath station TBZ (Trabzon, Turkey) by receiver function and dispersion analyses, *Geophys. J. Int.*, 158, 955-971.

- Cermak, V. & Rybach, L., 1987. *Terrestrial Heat Flow and the Lithosphere*, Springer-Verlag, New York.
- Chang, S.-J., Baag, C.-E. & Langston, C., 2004. Joint analysis of teleseismic receiver functions and surface wave dispersion using the genetic algorithm, *Bull. Seism. Soc. Am.*, 94,691-704.
- Clayton, R.W. & Wiggins, R.A., 1976. Source shape estimation and deconvolution of teleseismic body waves, *Geophys. J. Royal Astro. Soc.*, 47, 151-177.
- Cochran, J. R., 1983. A model for development of Red Sea, *Am. Assoc. Pet. Geol.*, 67, 41-69.
- Courtillot, V., 1980. Opening of the Gulf of Aden and Afar by progressive tearing, *Phys. Earth Planet. Int.*, 21, 343–350.
- Chian, C., C. Keen, I. Reid, and K. Louden (1995), Evolution of nonvolcanic rifted margins of the Labrador Sea, *Geology*, 23, 589-592.
- Chian, C., K. E. Louden, T. A. Minshull, and R. B. Whitmarsh (1999), Deep structure of the ocean-continent transition in the southern Iberia Abyssal Plain from seismic refraction profiles: Ocean Drilling Program (Legs 149 and 173) transect, *J. Geophys. Res.*, 104, 7443-7462.
- Cram Jr, I. H. (1962), Crustal structure of Texas coastal plain region, *Am. Assoc. Pet. Geol. Bull.*, 46, 1721-1727.
- Culotta, R., T. Latham, M. Sydow, J. Oliver, L. Brown, and S. Kaufman (1992), Deep structure of the Texas Gulf passive margin and its Ouachita-Precambrian basement:Results of the COCORP San Marcos Arch Survey, *Am. Assoc. Pet. Geol. Bull.*, 76, 270-283.
- Chase, C.G., Libarkin, J.A., Sussman, A.J., 2002. Colorado Plateau: Geoid and Means of Isostatic Support. *Int. Geol. Rev.* 44, 575–587. doi:10.2747/0020-6814.44.7.575.
- Dueker, K.G., Sheehan, A.F., 1997. Mantle discontinuity structure from midpoint stacks of converted P to S waves across the Yellowstone hotspot track. *J. Geophys. Res.* 102, 8313. doi:10.1029/96JB03857
- Dugda, M.T., Nyblade, A.A., 2006. New constraints on crustal structure in eastern Afar from the analysis of receiver functions and surface wave dispersion in Djibouti. *Geol. Soc. London, Spec. Publ.* 259, 239–251. doi:10.1144/GSL.SP.2006.259.01.19
- Derode, A., E. Larose, M. Tanter, J. De Rosny, A. Tourin, and M. Campillo (2003), Recovering the Green's function from field-field correlations in an open scattering medium (L), *J. Acoust. Soc. Am.*, 113, 2973-2976.

- Dickinson, W. R. (2009), The Gulf of Mexico and the southern margin of Laurentia, *Geology*, 37, 479-480.
- Dorman, J., J. L. Worzel, R. Leyden, T. N. Crook, and M. Hatzimmanuel (1972), Crustal section from seismic refraction measurements near Victoria, Texas, *Geophys.*, 37, 325-336.
- Dunbar, J. A., and D. S. Sawyer (1987), Implications of continental crust extension for plate reconstruction: An example from the Gulf of Mexico, *Tectonics*, 6, 739-755.
- Duncan, G., and H. Gurrola (2009), An updated interpretation of the Hales 1969 onshore-offshore refraction experiment: an investigation of the rifted margin of the Northern Gulf of Mexico and Gulf Coastal Plain, In: Fall Meeting 2009. *Am. Geophys. Union. Abstract #t53D-1620*.
- Dziewonski, A., S. Bloch, and M. Landisman (1969), A technique for the analysis of transient seismic signals, *Bull. Seismol. Soc. Am.*, 59, 427-444.
- Davis, T. E. & Principe, J. C., 1991. A simulated annealing like convergence theory for the simple genetic algorithm, in *Proc. of the Fourth International Conference on Genetic Algorithms*, Morgan Kaufmann, San Mateo, California.
- Dewey, J. F. & Sengor, A.M.C., 1979. Aegean and surrounding regions: Complex multiplate and continuum tectonics in a convergent zone, *Geol. Soc. Am. Bull.*, 90, 84-92.
- Dewey, J.F., Hempton, M.R., Kidd, W.S., SarogClu, F. & Sengor, A.M.C., 1986. Shortening of continental lithosphere: the neotectonics of Eastern Anatolia--a young collision zone, *Geol. Soc. Spec. Publ.*, London, 19, pp. 3-36.
- Dotduyev, S.I., 1986. The nappe structure of the Great Caucasus (in Russian), *Geotektonika*, 5, 94-105.
- Dziewonski, A., Bloch, S. & Landisman, M., 1969. Surface wave ray tracing azimuthal anisotropy: a generalized spherical harmonic approach technique for the analysis of transient seismic signals, *Bull. Seism. Soc. Am.*, 59, 427-444.
- Eagar, K. C., M. J. Fouch, and D. E. James (2010), Receiver function imaging of upper mantle complexity beneath the Pacific Northwest, United States, *Earth Planet. Sci. Lett.*, 297, 141--153.
- Eagar, K. C., M. J. Fouch, D. E. James, and R. W. Carlson (2011), Crustal structure beneath the High Lava Plains of eastern Oregon and surrounding regions from receiver function analysis *J. Geophys. Res.: Solid Earth* (1978--2012), 116.

- Escartín, J., G. Hirth, and B. Evans (1997a), Nondilatant brittle deformation of serpentinites: Implications for Mohr-Coulomb theory and the strength of faults, *J. Geophys. Res.*, 102, 2897-2913.
- Escartín, J., G. Hirth, and B. Evans (1997b), Effects of serpentinization on the lithospheric strength and the style of normal faulting at slow-spreading ridges, *Earth Planet. Sci. Lett.*, 151, 181-189.
- Evanzia, E., J. Pulliam, R. Ainsworth, H. Gurrola, and K. Pratt (2014), Seismic Vp & Vs tomography of Texas & Oklahoma with a focus on the Gulf Coast margin, *Earth Planet. Sci. Lett.*, <http://dx.doi.org/10.1016/j.epsl.2013.12.027>.
- Ewing, T.E., and S. C. Caran (1982), Late Cretaceous volcanism in South and Central Texas—stratigraphic, structural, and seismic models, *Gulf Coast Assoc. Geol. Soc. Trans.* 32, 137-145.
- Faber, S., Muller, G., 1980. Sp phases from the transition zone between the upper and lower mantle. *Bull. Seismol. Soc. Am.* 70, 487–508.
- Farra, V., Vinnik, L., 2000. Upper mantle stratification by P and S receiver functions. *Geophys. J. Int.* 141, 699–712. doi:10.1046/j.1365-246x.2000.00118.x
- Frederiksen, A. W.; Bostock, M. G., 2000. Modelling teleseismic waves in dipping anisotropic structures. *Geophys. J. Int.* vol. 141 (2) p. 401-412.
- Forrest, S., 1993. Genetic algorithms: Principles of natural selection applied to computation, *Science*, 261, 872-878.
- Gangopadhyay, A., Pulliam, J. & Sen, M.K., 2007. Waveform Modeling of Teleseismic S, SP, SsPmP, and Shear-Coupled PL Waves for Crust and Upper Mantle Velocity Structure Beneath Africa, *Geophys. J. Int.*, 170: 1210–1226.
- Geman, S. & Geman, D., 1984. Stochastic relaxation, Gibbs distributions, and the Bayesian restoration of images, *IEEE Trans. Patt. Anan. Mac. Int.*, 6, pp. 721–741.
- Gök, R., Sandvol, E., Türkelli, N., Seber, D. & Barazangi, M., 2003. Sn attenuation in the Anatolian and Iranian plateau and surrounding regions, *Geophys. Res. Lett.*, 30, 8042, doi:10.1029/2003GL018020.
- Gök, R., Mellors, R.J, Sandvol, E., Pasyanos, M.E., Hauk, T., Takedatsu, R., Yetirmishli, G., Teoman, U., Turkelli, N., Godoladze, T. & Javakishvirli, Z., 2011. Lithospheric velocity structure of the Anatolian plateau–Caucasus–Caspian region, *J. Geophys. Res.*, 116, p. B05303, doi: 10.1029/2009JB000837.
- Gök R., Pasyanos, M. & Zor, E., 2006. Lithospheric Structure of the Continent-Continent Collision Zone: Eastern Turkey, *Geophys. J. Int.*, 169, 1079-1088.

- Gök, R., Mahdi, H., Al-Shukri, H. & Rodgers, A.J., 2007. Crustal structure of Iraq from receiver functions and surface wave dispersion: Implications for understanding the deformation history of the Arabian–Eurasian collision, *Geophys J. Int.* 172, 1179–1187.
- Gök, R., Turkelli, N., Sandvol, E., Seber, D. & Barazangi, M., 2000. Regional wave propagation in Turkey and surrounding regions, *Geophys. Res. Lett.*, 27, 429–432, doi:10.1029/1999GL008375.
- Green, P.J., 1995. Reversible jump Markov chain Monte Carlo computation and Bayesian model determination, *Biometrika*, 82(4), 711–732.
- Gurrola, H., Baker, E. & Minster, B., 1996. Resolution of Receiver Function waveforms and resulting limitations in the modeling of Earth structure, *Eos Trans. AGU*, 77, 460.
- Gussinye, M.P., and T. J. Reston (2001), Rheological evolution during extension at nonvolcanic rifted margins: Onset of serpentinization and development of detachments leading to continental breakup, *J. Geophys. Res.*, 106, 3961-3975.
- Gussinye, M.P., T. J. Reston, and J. P. Morgan (2001), Serpentinization and magmatism during extension at non-volcanic margins: the effect of initial lithospheric structure, *Geol. Soc. London Spec. Publ.*, 187, 551-576.
- Gao, W., 2004. Upper mantle convection beneath the central Rio Grande rift imaged by P and S wave tomography. *J. Geophys. Res.* 109, B03305. doi:10.1029/2003JB002743
- Hales, A.L., J. B. Nations and C. E. Helsley (1970), Crustal structure study on the Gulf coast of Texas, *Am. Assoc. Pet. Geol. Bull.*, 54, 2040-3057.
- Hall, S. A., and I. J. Najmuddin (1994), Constraints on the tectonic development of the eastern Gulf of Mexico provided by magnetic anomaly data, *J. Geophys. Res.*, 99, 7161-7175.
- Hansen, S. M., K. G. Dueker, J. C. Stachnik, R. C. Aster, and K. E. Karlstrom (2013), A rootless rockies-Support and lithospheric structure of the Colorado Rocky Mountains inferred from CREST and TA seismic data, *Geochem. Geophys. Geosyst.*, 14, 2670-2695.
- Hansen, S., and K. Dueker (2009), P-and S-wave receiver function images of crustal imbrication beneath the Cheyenne Belt in southeast Wyoming, *Bull. Seismol. Soc. Am.*, 99, 1953-1961.

- Harry, D., and J. Londono (2004), Structure and evolution of the central Gulf of Mexico continental margin and coastal plain, southeast United States, *Geol. Soc. Am. Bull.*, 116, 188-199.
- Helfrich, G. (2006), Extended-time multitaper frequency domain cross-correlation receiver-function estimation, *Bull. Seismol. Soc. Am.*, 96, 344-347.
- Herrin, E., and T. Goforth (1977), Phase-matched filters: application to the study of Rayleigh waves, *Bull. Seismol. Soc. Am.*, 67, 1259-1275.
- Herrmann, R. B., C. J. Ammon, and J. Julia (2001), Application of joint receiver-function surface-wave dispersion for local structure in Eurasia, techreport.
- Huerta A.D., and D. L. Harry (2012), Wilson cycles, tectonic inheritance, and rifting of the North American Gulf of Mexico continental margin, *Geosphere*, 8, 374-385.
- Hammersley, J.M. & Handscomb, D.C., 1964. Monte Carlo Methods, Chapman & Hall, London.
- Hauser, J., Dyer, K.M., Pasyanos, M.E., Bungum, H., Faleide, J.I., Clark, S.A. & Schweitzer, J., 2011. A probabilistic seismic model for the European Arctic, *J. Geophys. Res.*, 116, B01303.
- Herrmann, R.B., 1973. Some aspects of band-pass filtering of surface waves, *Bull. Seism. Soc. Am.* 63, 663-671.
- Herrmann, R.B., Ammon, C.J. & Julia, J., 2001. Application of joint receiver-function surface-wave dispersion for local structure in Eurasia, *Proceedings of the 23rd Seismic Research Review: Worldwide Monitoring of Nuclear Explosions*, Jackson, WY, pp. 46-54.
- Hofstetter, R. & Bock, G., 2004. Shear-wave velocity structure of the Sinai sub-plate from receiver function analysis, *Geophys. J. Int.*, 158, 67 – 84.
- Holland, J. H., 1975. *Adaptation in Natural and Artificial Systems*, Univ. of Michigan Press, Ann Arbor, Michigan.
- Ingber, L., 1989. Very fast simulated reannealing, *Math. Comput. Modeling*, 12, 967–993.
- Ingber, L., 1993. Simulated annealing: practice versus theory, *Math. Computer Modeling*, 18, pp. 29–57.
- Julia, J., C. J. Ammon, and R. B. Herrmann (2003), Lithospheric structure of the Arabian Shield from the joint inversion of receiver functions and surface-wave group velocities, *Tectonophysics*, 371, 1-21.

- Julia, J., C. J. Ammon, and A. A. Nyblade (2005), Evidence for mafic lower crust in Tanzania, East Africa, from joint inversion of receiver functions and Rayleigh wave dispersion velocities, *Geophys. J. Int.*, 162, 555-569.
- Julia, J., C. Ammon, R. Herrmann, and A. M. Correig (2000), Joint inversion of receiver function and surface wave dispersion observations, *Geophys. J. Int.*, 143, 99-112.
- Julia, J., Ammon, C.J., Herrmann, R.B. & Correig, A.M., 2000. Joint inversions of receiver function and surface wave dispersion observations, *Geophys. J. Int.*, 143, 99-112.
- Julia, J., Ammon, C.J. & Nyblade, A.A., 2005. Evidence for mafic lower crust in Tanzania, East Africa, from joint inversion of receiver functions and Rayleigh wave dispersion velocities, *Geophys. J. Int.*, 162, 555-569.
- Jesse F. Lawrence, D.A.W., n.d. Combined receiver-function and surface wave phase-velocity inversion using a niching genetic algorithm: Application to Patagonia.
- Kaban, M. K., M. Tesauro, and S. Cloetingh (2010), An integrated gravity model for Europe's crust and upper mantle, *Earth Planet. Sci. Lett.*, 296, 195–209.
- Keller, G.R., 1999. The Rio Grande rift: A geological and geophysical overview. *Rocky Mt. Geol.* 34, 121–130. doi:10.2113/34.1.121.
- Kikuchi, M., Kanamori, H., 1982. Inversion of complex body waves. *Bull. Seismol. Soc. Am.* 72, 491–506.
- Kind, R., Vinnik, L.P., 1988. The upper- mantle discontinuities underneath the GRF array from P- to -S converted phases. *J. Geophys. - Zeitschrift fur Geophys.*
- King, S.D., 2007. Hotspots and edge-driven convection. *Geology* 35, 223. doi:10.1130/G23291A.1
- Kirkpatrick, S., Gelatt, C.D., Vecchi, M.P., 1983. Optimization by simulated annealing. *Science* 220, 671–80. doi:10.1126/science.220.4598.671
- Kreemer, C., Blewitt, G., Bennett, R.A., 2010. Present-day motion and deformation of the Colorado Plateau. *Geophys. Res. Lett.* 37, n/a–n/a. doi:10.1029/2010GL043374.
- Kumar, P., 2005. The lithosphere-asthenosphere boundary in the Tien Shan-Karakoram region from S receiver functions: Evidence for continental subduction. *Geophys. Res. Lett.* 32, L07305. doi:10.1029/2004GL022291.
- Kumar, P., Kind, R., Hanka, W., Wylegalla, K., Reigber, C., Yuan, X., Woelbern, I., Schwintzer, P., Fleming, K., Dahl-Jensen, T., Larsen, T.B., Schweitzer, J., Priestley, K., Gudmundsson, O., Wolf, D., 2005. The lithosphere–asthenosphere boundary in the North-West Atlantic region. *Earth Planet. Sci. Lett.* 236, 249–257. doi:10.1016/j.epsl.2005.05.029.

- Kennett, B.L.N, Engdahl, E.R. & Buland, R., 1995. Constraints on seismic velocities in the Earth from traveltimes, *Geophys. J. Int.*, 122, 108-124.
- Khain, V. E., & Lobkovskiy, L.I., 1994. Relict seismicity in the Alpine belt of Eurasia mode of occurrence, *Geotectonics, Engl. Transl.*, 28, 192–198.
- Korst, J. & Aarts, E.H.L., 1989. Simulated annealing and Boltzmann machines: A stochastic approach to combinatorial optimization and neural computing, Wiley, New York.
- Koulakov, I. & Sobolev, S.V., 2006. Moho depth and three-dimensional P and S structure of the crust and uppermost mantle in the Eastern Mediterranean and Middle East derived from tomographic inversion of local ISC data, *Geophys. J. Int.*, 164, 218-235, doi:10.1111/j.1365-246X.2005.02791.x.
- Keller, G.R., and D.H. Shurbet (1975), Crustal structure of the Texas Gulf Coastal Plain, *Geol. Soc. Am. Bull.*, 86, 807-810.
- Keller, G.R., and Jr. R. D. Hatcher (1999), Some comparisons of the structure and evolution of the southern Appalachian-Ouachita orogen and problems of the trans-European suture zone region, *Tectonophysics*, 314, 43-68.
- Langston, C. A. (1979), Structure under Mount Rainier, Washington, inferred from teleseismic body waves, *J. Geophys. Res.: Solid Earth*, 84, 4749-4762.
- Larose, E., A. Khan, Y. Nakamura, and M. Campillo (2005), Lunar subsurface investigated from correlation of seismic noise, *Geophys. Res. Lett.*, 32.
- Lawrence, J. F., and D. A. Wiens (2004), Combined receiver-function and surface wave phase-velocity inversion using a niching genetic algorithm: application to Patagonia, *Bull. Seismol. Soc. Am.*, 94, 977-987.
- Levshin, A., M. Ritzwoller, M. Barmin, and J. Stevens (2001), Short period group velocity measurements and maps in central Asia, techreport.
- Li, X., S. Sobolev, R. Kind, X. Yuan, and C. Estabrook (2000), A detailed receiver function image of the upper mantle discontinuities in the Japan subduction zone, *Earth Planet. Sci. Lett.*, 183, 527 - 541.
- Ligorria, J. P., and C. J. Ammon (1999), Iterative deconvolution and receiver-function estimation, *Bull. Seismol. Soc. Am.*, 89, 1395-1400.
- Lines, L. R., A. K. Schultz, and S. Treitel (1988), Cooperative inversion of geophysical data, *Geophysics*, 53, 8--20.

- Lundin, E.R., and G. Dore (2011), Hyperextension, serpentization, and weakening: A new paradigm for rifted margin compressional deformation, *Geol. Soc. Am.*, 39, 347-350.
- Marton, G., and R. T. Buffler (1994), Jurassic reconstruction of the Gulf of Mexico basin, *Int. Geol. Rev.*, 36, 545–586.
- Le Pichon, X. & Francheteau, J., 1978. A plate-tectonic analysis of the Red Sea - Gulf of Aden area, *Tectonophysics*, 46, 369-406.
- Levin, V. & Park, J., 2000. Shear zones in the Proterozoic lithosphere of the Arabian shield and the nature of the Hales discontinuity, *Tectonophysics*, 323 , 131-148.
- Li, X., Kind, R., Yuan, X., Wolbern, I. & Hanka, W., 2004. Rejuvenation of the lithosphere by the Hawaiian plume, *Nature*, 427, 827– 829.
- Lekić, V., Fischer, K.M., 2014. Contrasting lithospheric signatures across the western United States revealed by Sp receiver functions. *Earth Planet. Sci. Lett.* 402, 90–98. doi:10.1016/j.epsl.2013.11.026
- McQuarrie, N., Wernicke, B.P., 2005. An animated tectonic reconstruction of southwestern North America since 36 Ma. *Geosphere* 1, 147–172. doi:10.1130/GES00016.1.
- Morgan, P., Seager, W.R., Golombek, M.P., 1986. Cenozoic thermal, mechanical and tectonic evolution of the Rio Grande Rift. *J. Geophys. Res.* 91, 6263. doi:10.1029/JB091iB06p06263
- Morgan, P., Swanberg, C.A., 1985. On the Cenozoic uplift and tectonic stability of the Colorado Plateau. *J. Geodyn.* 3, 39–63. doi:10.1016/0264-3707(85)90021-3.
- Moucha, R., Forte, A.M., Rowley, D.B., Mitrovica, J.X., Simmons, N.A., Grand, S.P., 2008. Mantle convection and the recent evolution of the Colorado Plateau and the Rio Grande Rift valley. *Geology* 36.
- Maggi, A. & Priestley, K., 2005. Surface waveform tomography of the Turkish-Iranian Plateau, *Geophys. J. Int.*, 160, 1068–1080, doi:10.1111/j.1365-246X.2005.02505.x.
- Makris, J. & Wang, J., 1995. Geophysical study and geodynamics of the Eastern Mediterranean Sea, Rep. 719/48–1, Inst. Geophys., Univ. of Hamburg, Hamburg.
- McQuarrie, N., Stock, J.M., Verdel, C. & Wernicke, B.P., 2004. Cenozoic evolution of Neotethys and implications for the causes of plate motions, *Geophys. Res. Lett.*, 30, 2036, doi: 10.1029/2003GL017992
- Metropolis, N. & Ulam, S.M., 1949. The Monte Carlo method, *J. Am. Stat. Assoc.*, 44, 335–341.

- Metropolis, N., Rosenbluth, A.W., Rosenbluth, M.N., Teller, A.H. & Teller, E., 1953. Equation of state calculations by fast computing machines, *J. Chem. Phys.*, 21, 1087–1092.
- Mosegaard, K. & Tarantola, A., 1995. Monte Carlo sampling of solutions to inverse problems, *J. geophys. Res.*, 100, 12 431–12 447.
- Menard, H.W. (1967), Transitional types of crust under small ocean basins, *J. Geophys. Res.*, 72, 3061-3073.
- Mercier, J.-P., M. G. Bostock, and A. M. Baig (2006), Improved Green's functions for passive-source structural studies, *Geophysics*, 71, SI95--SI102.
- Merle, O. (2011), A Simple Continental Rift Classification, *Tectonophysics*, 513, 88-95.
- Menzies, M.A., S. L. Klemperer, C. J. Ebinger, and J. Baker (2002), Characteristics of volcanic rifted margins, *Geol. Soc. Spec. Pap.*, 362, 1-14.
- Mickus, K.L., and G. R. Keller (1992), Lithospheric structure of the south-central United States, *Geology*, 20, 335-338.
- Mickus, K., R. J. Stern, G. Keller, and E. Y. Anthony (2009), Potential field evidence for a volcanic rifted margin along the Texas Gulf Coast, *Geology*, 37, 387--390.
- Mjelde, R., T. Raum, Y. Murai, and T. Takanamic (2007), Continent-ocean transitions: Review, and a new tectono-magmatic model of the Voring Plateau, NE Atlantic: *J. Geodyn.*, v. 43, p. 374-392, doi: 10.1016/j.jog2006.09.013.
- Molina-Garza, R.S., R. Van der Voo, and J. Urrutia- Fucuguachi (1992), Paleomagnetism of the Chiapas massif, southern Mexico: Evidence for rotation of the Maya block and implications for the opening of the Gulf of Mexico, *Geol. Soc. Am. Bull.*, 104, 1156-1168.
- Mosher, S., J. S. F. Levine, and W. D. Carlson (2008), Mesoproterozoic plate tectonics: A collisional model for the Grenville-aged orogenic belt in the Llano uplift, central Texas, *Geology*, 36, 55-58.
- Mutter, J.C., M. Talwani, and P. L. Stoffia (1984), Evidence for a thick oceanic crust adjacent to the Norwegian margin, *J. Geophys. Res.*, 89, 483- 502.
- Nagihara, S., C. Christie, N. Ogiamien, R. Oladokun, O. Ajiboye, and S. Ojeda (2012), Gulf of Mexico borehole geothermal data integration into the national geothermal data systems, part 1: Texas continental shelf, *Gulf Coast Assoc. Geol. Soc. Trans.*, 62, 589–591.

- Nettles, M., and A. Dziewonski (2008), Radially anisotropic shear velocity structure of the upper mantle globally and beneath North America, *J. Geophys. Res.*, 113, B02303.
- Ozacar, A.A., 2007. Complex rupture processes of large strike slip earthquakes and receiver function analysis of crust and upper mantle in active tectonic settings, PhD Thesis, University of Arizona, Arizona, USA.
- Ozacar, A. A., Gilbert, H. & Zandt, G., 2008. Upper mantle discontinuity structure beneath East Anatolian Plateau (Turkey) from receiver functions, *Earth Planet. Sci. Lett.*, 269, 427–435, doi:10.1016/j.epsl.2008.02.036.
- Ozalaybey, S., Savage, M.K., Sheehan, A.F., Louie, J.N. & Brune, J.N., 1997. Shear-wave velocity structure in the northern Basin and Range province from the combined analysis of receiver functions and surface waves, *Bull. Seism. Soc. Am.*, 87, 183-199.
- Pareto, V., 1906. *Manual of Political Economy* (1971 translation from 1927 edition). Augustus Kelley, New York, USA.
- O'Reilly, B.M., F. Hauser, A. W. B. Jacob, and P. M. Shannon (1996), The lithosphere below the Rockall Trough: Wide-angle seismic evidence for extensive serpentinization, *Tectonophysics*, 255, 1-23.
- Owens, T.J., Nyblade, A.A., Gurrola, H., Langston, C.A., 2000. Mantle transition zone structure beneath Tanzania, east Africa. *Geophys. Res. Lett.* 27, 827–830. doi:10.1029/1999GL005429
- Parsons, T.E., 1995. The basin and range province: Chapter 7 277–324.
- Pasyanos, M.E., 2005. A variable resolution surface wave dispersion study of Eurasia, North Africa, and surrounding regions. *J. Geophys. Res.* 110, B12301. doi:10.1029/2005JB003749.
- Pindell, J. L., and L. Kennan (2009), Tectonic evolution of the Gulf of Mexico, Caribbean and northern South America in the mantle reference frame: an update, *Geol. Soc. London Spec. Publ.*, 328, 1-55.
- Pindell, J.L., and J. F. Dewey (1982), Permo-Triassic reconstruction of western Pangea and the evolution of the Gulf of Mexico/Caribbean region, *Tectonics*, 1, 179-211.
- Pindell, J. L. (1994), Evolution of the Gulf of Mexico and the Caribbean, in S. K. Donovan and T. A. Jackson, eds., *Caribbean geology, An introduction*: Kingston, University of the West Indies Publishers Association, 13-39.

- Paul, A., Kaviani, A., Hatzfeld, D., Vergne, J. & Mokhtari, M., 2006. Seismological evidence for crustal-scale thrusting in the Zagros mountain belt (Iran), *Geophys. J. Int.*, 166, 227-237, doi:10.1111/j.1365-246X.2006.02920.x.
- Paul, A., Kaviani, A., Hatzfeld, D., Mohammad, T. & Catherine, P., 2010. Seismic imaging of the lithospheric structure of the Zagros mountain belt (Iran), *Geol. Soc. London, Spec. Pub.*, Feb. 2012.
- Pasyanos, M.E., Franz, G.A. & Ramirez, A.L., 2006. Reconciling a geophysical model to data using a Markov chain Monte Carlo algorithm: An application to the Yellow Sea- Korean Peninsula region, *J. Geophys. Res.*, 111, B03313.
- Press, F., 1968. Earth models obtained by Monte Carlo inversion, *J. Geophys. Res.*, 73, 5223–5234.
- Press, W.H., Teukolsky, S.A., Vetterling, W.T., & Flannery, B.P., 2007. "Section 10.12. Simulated Annealing Methods". *Numerical Recipes: The Art of Scientific Computing* (3rd ed.). New York: Cambridge University Press.
- Pulliam, J., Sen, M.K., Frohlich, C. & Grand, S., 2002. Waveform modeling of the crust and upper mantle using S, Sp, SsPmP and shear-coupled PL waves, *Proc. 24th Seis. Res. Rev. – Nuclear Explosion Monitoring: Innovation and Integration*, pp. 144–153.
- Pulliam, J. & Sen, M.K., 2005. Assessing Uncertainties in Waveform Modeling of the Crust and Upper Mantle, *Proceedings of the 27th Seismic Research Review: Ground-Based Nuclear Explosion Monitoring Technologies*, Palm Springs, CA, pp. 152 – 160.
- Pulliam, J., Sen, M.K. & Gangopadhyay, A., 2006. Determination of Crust and Upper Mantle Structure beneath Africa Using a Global Optimization-Based Waveform Modeling Technique, *Proceedings of the 28th Seismic Research Review: Ground-Based Nuclear Explosion Monitoring Technologies*, Orlando, FL, pp. 196-208.
- Reilinger, R. & McClusky, S., 2011. Nubia–Arabia–Eurasia plate motions and the dynamics of Mediterranean and Middle East tectonics, *Geophys. J. Int.*, 186, 971-979, DOI: 10.1111/j.1365-246X.2011.05133.x.
- Robertson, A.H.F., 2000. Mesozoic-Tertiary tectonic-sedimentary evolution of a South Tethyan oceanic basin and its margins in Southern Turkey, *Geol. Soc. London, Spec. Pub.*, , 173, 97-138.
- Ruegg, J.C., 1975. Main results about the crustal and upper mantle structure of the Djibouti region (T.F.A.I.), In: A. Pilger and A. Rosler (Editors). *Afar Depression of Ethiopia*, E. Schweizer. Verlagsbuchhandl. (Naegele u. Obermiller), Stuttgart, Federal Republic of Germany (DEU), 120–134.

- Reston, T.J., J. Pennell, A. Stubenrauch, I. Walker, and M. P. Gussinye (2001), Detachment faulting, mantle serpentinization, and serpentinite-mud volcanism beneath Porcupine Basin, southwest of Ireland, *Geol. Soc. Am.*, 29, 587-590.
- Ritzwoller, M. H., & A. L. Levshin (1998), Eurasian surface wave tomography: Group velocities, *J. Geophys. Res.: Solid Earth* (1978-2012), 103, 4839-4878.
- Ross, M. I., and C. R. Scotese (1988), A hierarchical tectonic model of the Gulf of Mexico and Caribbean region, *Tectonophysics*, 155, 139-168.
- Russell, D. R., R. B. Herrmann, and H. J. Hwang (1988), Application of frequency variable filters to surface-wave amplitude analysis, *Bull. Seismol. Soc. Am.*, 78, 339-354.
- Roger Buck, W., 1986. Small-scale convection induced by passive rifting: the cause for uplift of rift shoulders. *Earth Planet. Sci. Lett.* 77, 362–372. doi:10.1016/0012-821X(86)90146-9
- Roy, M., MacCarthy, J.K., Selverstone, J., 2005. Upper mantle structure beneath the eastern Colorado Plateau and Rio Grande rift revealed by Bouguer gravity, seismic velocities, and xenolith data. *Geochemistry, Geophys. Geosystems* 6, n/a–n/a. doi:10.1029/2005GC001008.
- Schroeder, T., B. John, and B. R. Frost (2002), Geologic implications of seawater circulation through peridotite exposed at slow-spreading ridges, *Geology*, 30, 367-370.
- Shapiro, N. M., and M. Campillo (2004), Emergence of broadband Rayleigh waves from correlations of the ambient seismic noise, *Geophys. Res. Lett.*, 31.
- Shervais, J.W., P. Kolesar, and K. Andreasen (2005), A field and chemical study of serpentinization- Stonyford, California: chemical flux and mass balance, *Int. Geol. Rev.*, 47, 1-23.
- Snieder, R. (2004), Extracting the Green's function from the correlation of coda waves: A derivation based on stationary phase, *Physical Review E*, 69, 046610.
- Stern, R. J., E. Y. Anthony, M. Ren, B. E. Lock, I. Norton, and J. I. Kimura (2011), Southern Louisiana salt dome xenoliths: First glimpse of Jurassic (ca. 160 Ma) Gulf of Mexico crust, *Geology*, 39, 315-318.
- Sambridge, M., 1998. Geophysical inversion with a neighborhood algorithm - II, Appraising the ensemble, *Geophys. J. Int.*, 138, 727-746.
- Sambridge, M., 1999. Geophysical inversion with a neighborhood algorithm - I, Searching a parameter space, *Geophys. J. Int.*, 138, 479-494.

- Sandvol, E., Seber, D., Calvert, A. & Barazangi, M., 1998. Grid search modeling of receiver functions: Implications for crustal structure in the Middle East and North Africa, *J. Geophys. Res.*, 103, 26,899-26,917.
- Sandvol, E., Turkelli, N., Zor, E., Gök, R., Bekler, T., Gurbuz, C., Seber, D. & Barazangi, M., 2003. Shear wave splitting in a young continent-continent collision: An example from Eastern Turkey, *Geophys. Res. Lett.*, 30, 8041, doi:10.1029/2003GL017390.
- Seber, D., Vallve, M., Sandvol, E., Steer, D. & M. Barazangi, 1997. Middle East Tectonics: Applications of Geographic Information Systems, *GSA Today*.
- Sen, M.K. and Stoffa, P.L., 1996. Bayesian inference, Gibbs' sampler and uncertainty estimation in geophysical inversion, *Geophysical Prospecting*, 44, 313-350.
- Sengor, A. M. C. & Kidd, W. S. F., 1979. Post-collisional tectonics of the Turkish-Iranian plateau and a comparison with Tibet, *Tectonophysics*, 55, 361-376.
- Sheehan, A., Abers, G., Jones, C.H. & Lerner-Lam, A., 1995. Crustal thickness variations across the Rocky Mountain front from teleseismic receiver functions, *J. Geophys. Res.*, 100, 20391-20404.
- Shelton, A.W., 1990. The Interpretation of gravity data in Oman: constraints on the ophiolite emplacement mechanism, *The Geology and Tectonics of the Oman Region*, pp. 459-471, eds A.H.F. Robertson, M.P. Searle and A.C. Ries, *Geol. Soc. Lond. Spec. Publ.* No. 49.
- Sherkati, S. & Letouzey, J., 2004. Variation of structural style and basin evolution in the central Zagros (Izeh zone and Dezful Embayment), Iran, *Marine and Petroleum Geology*, 21, 535-554.
- Szu, H. & Hartley, R., 1987. Fast simulated annealing, *Phys. Lett.*, 122A, 157-62.
- Sahagian, D., Proussevitch, A., Carlson, W., 2002. Timing of Colorado Plateau uplift: Initial constraints from vesicular basalt-derived paleoelevations. *Geology* 30, 807-810. doi:10.1130/00917613(2002)030
- Sen, M.K., Stoffa, P.L., 1995. *Global Optimization Methods in Geophysical Inversion*. Elsevier.
- Stern, T., Houseman, G., Salmon, M., Evans, L., 2013. Instability of a lithospheric step beneath western North Island, New Zealand. *Geology* 41, 423-426. doi:10.1130/G34028.1.
- Tarantola, A., 1994. *Inverse Problem Theory: Methods for Data Fitting and Model Parameter Estimation*, Elsevier, Amsterdam, The Netherlands, 600 pp.

- Tiberi, C., Leroy, S., D'Acemont, E., Bellahsen, N., Ebinger, C., Al-Lazki, A. & Pointu, A., 2006. Crustal geometry of the northeastern Gulf of Aden passive margin: localization of the deformation inferred from receiver function analysis, *Geophys. J. Int.* 168, 1247–1260.
- Türkoğlu, E., Unsworth, M., Çağlar, Ý. Tuncer, V. & Avşar, Ü. 2008. Lithospheric structure of the Arabia-Eurasia collision zone in eastern Anatolia: Magnetotelluric evidence for widespread weakening by fluids?, *Geology*, 36, 619–622, doi:10.1130/G24683A.1.
- Tesauro, M., M.K. Kaban, W.D. Mooney, and S. Cloetingh (2014), NACr14: A 3D model for the crustal structure of the North American Continent, *Tectonophysics*, 631, 65-86.
- Thomas, W.A. (1991), The Appalachian-Ouachita rifted margin of southeastern North America, *Geol. Soc. Am. Bull.*, 103, 415-431.
- Thomas, W.A. (2005), Tectonic inheritance at a continental margin, *Geol. Soc. Am. Tod.*, 16, 2.
- Tkalčić, H., Pasyanos, M.E., Rodgers, A.J., Gök, R., Walter, W.R., Al-Amri, A., 2006. A multistep approach for joint modeling of surface wave dispersion and teleseismic receiver functions: Implications for lithospheric structure of the Arabian Peninsula. *J. Geophys. Res.* 111, B11311. doi:10.1029/2005JB004130.
- Vanacore, E., Taymaz, T. & Saygin, E., 2013. Moho structure of the Anatolian plate from receiver function analysis, *Geophys. J. Int.*, 193,329-337.
- Vernant, P. & Chery, J., 2006. Low fault friction in Iran implies localized deformation for the Arabia-Eurasia collision zone, *Earth Planet. Sci. Lett.*, 246, 197–206, doi:10.1016/j.epsl.2006.04.021.
- Van Wijk, J., van Hunen, J., Goes, S., 2008. Small-scale convection during continental rifting: Evidence from the Rio Grande rift. *Geology* 36, 575. doi:10.1130/G24691A.1.
- Van Wijk, J.W., Baldridge, W.S., van Hunen, J., Goes, S., Aster, R., Coblenz, D.D., Grand, S.P., Ni, J., 2010. Small-scale convection at the edge of the Colorado Plateau: Implications for topography, magmatism, and evolution of Proterozoic lithosphere. *Geology* 38, 611–614. doi:10.1130/G31031.1
- Varela, C.L., Stoffa, P.L., Sen, M.K., 1998. Background velocity estimation using non-linear optimization for reflection tomography and migration misfit. *Geophysical Prospecting* 46, Issue 1, 51-78.

- Wiggins, R. A., 1969. Monte Carlo inversion of body wave observations, *J. Geophys. Res.*, 74, 3171–3181.
- Walker, N.W. (1992), Middle Proterozoic geologic evolution of Llano uplift, Texas: Evidence from U-Pb zircon geochronometry, *Geol. Soc. Am. Bull.*, 104, 494-504.
- Walter, D. M., and M.K. Kaban (2010), The North American upper mantle: Density, composition, and evolution, *J. Geophys. Res.*, 115, B12424.
- Wapenaar, K. (2004), Retrieving the elastodynamic Greens function of an arbitrary inhomogeneous medium by cross correlation, *Phys. Rev. Lett.*, 93, 254301.
- Weaver, R. L., and O. I. Lobkis (2001), On the emergence of the Green's function in the correlations of a diffuse field, *J. Acous. Soc. Am.*, 110, 3011-3017.
- Weaver, R. L., and O. I. Lobkis (2004), Diffuse fields in open systems and the emergence of the Green's function (L), *J. Acous. Soc. Am.*, 116, 2731--2734.
- Whitmarsh, R. B., and D. S. Sawyer (1996), The ocean/continent transition beneath the Iberia Abyssal Plain and continental-rifting to seafloor spreading processes, *Proc. Ocean Drill. Program Sci. Results*, 149, 713-733, 1996.
- Whitmeyer, S. J., and Karlstrom, K. E. (2007), Tectonic model for the Proterozoic growth of North America, *Geosphere*, 3, 220--259.
- White, R., and D. P. McKenzie (1989), Magmatism at rift zones: The generation of volcanic continental margins and flood basalts, *J. Geophys. Res.*, 94, 7685-7729.
- West, M., 2004. Crust and upper mantle shear wave structure of the southwest United States: Implications for rifting and support for high elevation. *J. Geophys. Res.* 109, B03309. doi:10.1029/2003JB002575
- Wilson, D., 2005a. Imaging the seismic structure of the crust and upper mantle beneath the Great Plains, Rio Grande Rift, and Colorado Plateau using receiver functions. *J. Geophys. Res.* 110, B05306. doi:10.1029/2004JB003492
- Wilson, D., 2005b. Seismic imaging of the crust and upper mantle using regularized joint receiver functions, frequency–wave number filtering, and multimode Kirchhoff migration. *J. Geophys. Res.* 110, B05305. doi:10.1029/2004JB003430
- Wilson, D.C., Angus, D.A., Ni, J.F., Grand, S.P., 2006. Constraints on the interpretation of S -to- P receiver functions. *Geophys. J. Int.* 165, 969–980. doi:10.1111/j.1365-246X.2006.02981.x
- Woodward, L.A., 1977. Rate of crustal extension across the Rio Grande Rift near Albuquerque, New Mexico. *Geology* 5, 269–272. doi:10.1130/0091-7613(1977)5.

- Young, H., and C. T. Lee (2009), Fluid-metasomatized mantle beneath the Ouachita belt of southern Laurentia: Fate of lithospheric mantle in a continental orogenic belt, *Lithosphere*, 1, 370--383.
- Yuan, X., Kind, R., Li, X., Wang, R., 2006. The S receiver functions: synthetics and data example. *Geophys. J. Int.* 165, 555–564. doi:10.1111/j.1365-246X.2006.02885.x
- Zhao, L. S., M. K. Sen, P. Stoffa, and C. Frohlich (1996), Application of very fast simulated annealing to the determination of the crustal structure beneath Tibet, *Geophys. J. Int.*, 125, 355-370.
- Zheng, T., L. Chen, L. Zhao, W. Xu, and R. Zhu (2006), Crust-mantle structure difference across the gravity gradient zone in North China Craton: Seismic image of the thinned continental crust, *Phys. Earth Planet. Int.*, 159, 43 - 58.
- Zhu, L. (2000), Crustal structure across the San Andreas Fault, southern California from teleseismic converted waves, *Earth Planet. Sci. Lett.*, 179, 183 - 190.
- Zor, E., Gürbüz, C., Türkelli, N., Sandvol, E., Seber, D. & Barazangi, M., 2003. The crustal structure of the East Anatolian Plateau from receiver functions, *Geophys. Res. Lett.*, 30, 8044, doi: 10.1029/2003GL018192.
- Zhu, L., Kanamori, H., 2000. Moho depth variation in southern California from teleseismic receiver functions. *J. Geophys. Res.* 105, 2969. doi:10.1029/1999JB900322.